Synthesis of Ultra-Wideband Array Antennas

Hamad W. Alsawaha

Dissertation submitted to the faculty of Virginia Polytechnic Institute and State University in partial fulfillment of the requirements for the degree of

Doctor of Philosophy
In
Electrical Engineering

Virginia Polytechnic Institute and State University

Ahmad Safaai-Jazi (Chair)
Gary Brown
William Davis
Timothy Pratt
Warren Stutzman
Werner Kohler

December 9, 2013
Blacksburg, Virginia

Keywords: antenna arrays, array synthesis, ultra-wideband antenna arrays

Synthesis of Ultra-wideband Array Antennas

Hamad W. Alsawaha

(ABSTRACT)

Acquisition of ultra-wideband signals by means of array antennas requires essentially frequency-independent radiation characteristics over the entire bandwidth of the signal in order to avoid distortions. Factors contributing to bandwidth limitation of arrays include array factor, radiation characteristics of the array element, and inter-element mutual coupling. Strictly speaking, distortion-free transmission or reception of ultra-wideband signals can be maintained if the magnitude of the radiated field of the array remains constant while its phase varies linearly with frequency over the bandwidth of interest. The existing wideband-array synthesis methods do not account for all factors affecting the array bandwidth and are often limited to considering the array factor and not the total field of the array in the synthesis process.

The goal of this study is to present an ultra-wideband array synthesis technique taking into account all frequency-dependent properties, including array total pattern, phase of the total radiated field, element field, element input impedance, and inter-element mutual coupling. The proposed array synthesis technique is based on the utilization of frequency-adaptive element excitations in conjunction with expressing the total radiated field of the array as a complex Fourier series. Using the proposed method, element excitation currents required for achieving a desired radiation pattern, while compensating for frequency variations of the element radiation characteristics and the inter-element mutual coupling, are calculated.

An important consideration in the proposed ultra-wideband array design is that the 'phase bandwidth', defined as the frequency range over which the phase of the total radiated field of the array varies linearly with frequency, is taken into account as a design requirement in the synthesis process. Design examples of linear arrays with desired radiation patterns that are expected to remain unchanged over the bandwidth of interest are presented and simulated. Two example arrays, one with a wire dipole as its element and another using an elliptically-shaped

disc dipole as the element are studied. Simulation results for far-field patterns, magnitude and phase characteristics, and other performance criteria such as side-lobe level and scanning range are presented.

Synthesis of two-dimensional planar arrays is carried out by employing the formulations developed for linear arrays but generalized to accommodate the geometry of planar rectangular arrays. As example designs, planar arrays with wire dipoles and elliptical-shaped disc dipoles are studied. The simulation results indicate that synthesis of ultra-wideband arrays can be accomplished successfully using the technique presented in this work. The proposed technique is robust and comprehensive, nonetheless it is understood that the achieved performance of a synthesized array and how closely the desired performance is met also depends on some of the choices the array designer makes and other constraints, such as number of elements, type of element, size, and ultimately cost.

To my father Waled who passed away on (July 28, 2011)

To my mother Fadhela

And to my brother Khaled and my sisters Rana and Badriya

Acknowledgements

I would like to thank my academic advisor and teacher, Dr. Ahmad Safaai-Jazi, for his support and guidance through out the years that I have spent on my MS and PhD degrees at Virginia Tech. The challenging questions and valuable discussions that I had with Dr. Safaai-Jazi were of enormous help in maintaining great quality of education and research. I would also like to thank Dr. Gary Brown for being a great teacher and a member of the advisory committee. I would also like to thank Dr. William Davis for being a teacher in several classes and a member of the advisory committee in my MS and PhD degrees. I thank Dr. Timothy Pratt for being a teacher, a member of the advisory committee, and for his feedback on this dissertation. I also thank Dr. Warren Stutzman for his acceptance of being a member of my advisory committee and for his feedback on this dissertation. I would also like to thank Dr. Werner Kohler for accepting of being a member of my advisory committee.

I am grateful to my family for their support and encouragement during the years of my graduate studies. I thank my close friends, colleagues, members of VTAG and members of Wireless@VT for their help and support.

Table of Contents

List of Figures

List of Tables

Chapter 1: Introduction

1.1 Background

Many emerging wireless technologies require highly reconfigurable radiation interfaces that are capable of operating over wide bandwidths to acquire broadband signals. Phased array antennas are found to be the best candidates for many wideband wireless systems due to their capability in providing spatial filtering with high degrees of selectivity [1]. Spatial filtering is important especially when separation of frequency overlapping signals originated from different locations is needed [2], or when highly-directed, radiated electromagnetic energy is required. Other important functions that can be achieved by antenna arrays include the ability to provide reconfigurable wave polarization, beam scanning, and synthesized in power-radiation patterns or beam forming. In recent research, frequency independent beam forming or power radiation-pattern synthesis has been of particular interest in applications such as wideband wireless communication systems, radar systems, microwave thermotherapy, medical imaging, and tumor detection [3].

Array radiation pattern synthesis, a process that may be regarded as the opposite to array analysis, consists of two major steps [4-7]. The first step in array synthesis is to define the desired radiation pattern as a function of spatial coordinates, while the second step is to determine the configuration of the elements of the array and their excitation currents. This conventional approach, however, is limited to narrow-band arrays. Narrow-band array pattern synthesis is well established and has been investigated extensively in the literature of antenna theory, where spatial parameters are considered as the only variables in the array-factor expression. Wideband array synthesis, on the other hand, has been mostly approached by means of optimization methodologies. If bandwidths pertaining to radiation characteristics of an array are a concern, frequency in the array factor must be treated as an additional design parameter. Many researchers have investigated the possibility of providing frequency independent array beam forming; such studies have been performed both in the time domain and in the frequency domain. Frequency independent beam forming is an important consideration, particularly if the acquisition of a wideband signal with minimal distortions is a performance goal.

1.2 Motivation, scope, and goals of research

Wideband signal acquisition requires wideband array performance with minimized signal distortions. In order to transmit or receive a wideband signal, the array has to exhibit an essentially frequency-invariant performance over the bandwidth of the signal in order to avoid distortions. All factors contributing to the frequency dependence of the total radiated field of the array have to be considered and compensated in the design process in order for the array to provide a wideband performance. The frequency dependent properties that are dealt with in this research include: array radiation pattern, array directivity, phase of the total radiated field, element field, element input impedance, and inter-element mutual coupling.

Achieving wideband, or to some extent frequency-invariant, array performance has been investigated by researchers in several fields, as will be discussed in the literature review in Chapter 2. Researchers [8-26] in the field of signal processing have presented several filter design techniques for compensating only the frequency dependent parameters in the array factor expression. Most of these studies assume an ideal isotropic antenna as the element of the array, leaving the effects due to frequency-dependent properties associated with the element antenna untreated. Incorporating the radiation characteristics of the element antenna into the model of the array allows the effects due to inter-element mutual coupling to be accounted for. Inter-element mutual coupling is an important frequency dependent factor that affects the wideband performance of the array in a complex manner. Frequency-adaptive element excitation is found to be the best technique for compensating the inter-element mutual coupling.

Many researchers have employed frequency-adaptive element excitation techniques, yet none has considered all of the frequency-dependent factors mentioned earlier in this section. In fact, all of these factors are inter-related. The input impedance of the element antenna, being a function of frequency, is highly affected by inter-element mutual coupling and is also a function of the scan angle. Because of the induced currents on a single element due to radiation by its surrounding elements, the radiated field of the element in a fully-active array is not the same as that when it is used in isolation. The radiation pattern and hence the gain of the array are highly impacted by the field of the element. Researchers working in the area of energy directing arrays have addressed the importance of using frequency adaptive excitation to achieve optimal

performance for maximum directed energy. However, if the shape of the wideband signal is a concern, energy maximization techniques do not provide the frequency-invariant performance of the array needed to achieve wideband signal transmission and reception with minimal distortions. In addition to element input impedance and mutual coupling with neighboring elements, frequency dependence of the element radiated field also influences the overall bandwidth of the array. This dependence is, in general, two fold, as both the magnitude and the phase of the element field vary with frequency over a wide frequency range. It appears that the impact of 'phase bandwidth' of the element radiated field on the overall array bandwidth has not been adequately addressed.

The goal of this study is to present an ultra-wideband, array synthesis technique through the utilization of frequency adaptive element excitations in conjunction with expressing the total radiated field of the array as a complex Fourier series, taking into account all frequency-dependent factors mentioned above. Using the proposed method, array factors with arbitrary spatial and frequency dependences can be realized, and compensations for frequency dependences of the element radiation characteristics and mutual coupling are achieved.

Chapter 2 of this dissertation presents a literature review and brief discussions of the related research performed over the last few decades. Attention will be focused on past work pertaining to wideband array synthesis based on frequency adaptive techniques. In Chapter 3, basics of antenna array analysis and synthesis are presented. Synthesis of ultra-wideband linear arrays that can provide nearly frequency-independent radiated fields over the bandwidth of interest but along a specific direction in space is addressed. Chapter 4 is devoted to developing an array synthesis technique that allows for compensating the variations of the element field as a function of space and frequency as well as the effects due to inter-element mutual coupling. Since the aim is to achieve transmission or reception of ultra-wideband signals with minimum distortions, the phase bandwidth is regarded as being equally important as the magnitude bandwidth. The magnitude bandwidth is defined as the frequency range over which the magnitude of total radiated field of the array (and hence its radiation pattern and gain) remain nearly unchanged, while the phase bandwidth is the frequency range over which the phase of the total radiated field varies linearly with frequency. All compensations are applied to both magnitude and phase. The array element is assumed to be linearly polarized, thus allowing the

array factor to be expressed simply are a scalar function. The element excitation currents required for achieving a desired radiation pattern, while compensating for frequency variations of the element radiation characteristics and the inter-element mutual coupling, are calculated. The dependence of the input impedance of the array element with the scan angle is another factor that is addressed in Chapter 4. In Chapter 5, design examples of linear arrays with desired radiation patterns that are meant to remain unchanged over the bandwidth of interest are presented and simulated. Two arrays, one with a wire dipole element and another using an elliptically-shaped disc dipole element are studied. Synthesis of two-dimensional planar arrays is carried out in Chapter 6 by employing the design technique presented in Chapter 4 but generalized to planar rectangular arrays. Simulation results for planar arrays of wire dipoles and elliptical dipoles are also presented in this chapter. Chapter 7 addresses the implementation of element excitations by means of digital filters. The block diagram of FIR filters needed to construct the required excitation signals from the source signal is discussed. Chapter 8 summarizes the results, conclusions, and contributions of this research and points out directions for further investigations.

Chapter 2: Literature Review

2.1 Wideband array design in signal-processing applications

Frequency-invariant beam formers have been investigated theoretically by researchers in the field of signal processing. Most of these studies start with a mathematical manipulation of the array factor expression in order to isolate the frequency dependent terms and minimize their effects by using specific filter designs. An example of such studies is described by Chan and Pun [8], in which the Parks-McClellan filter design algorithm is used to achieve the necessary filtering to compensate for frequency dependencies in the array factor. The isolation of the frequency dependent term in [8] is obtained by expanding the complex exponential function in the array factor expression through the use of Bessel function properties, followed by an asymptotic approximation of the resulting series expansion. The approach presented in [8] accounts for radiation in a single plane in space; that is, one spatial variable is assumed to be constant for a two-dimensional planar array.

Ghavami [9] recognized the possibility of mapping the spatial variable domain of a two-dimensional planar array into an auxiliary frequency domain. This domain mapping allowed for isolating the frequency dependent spatial variables and determining the required element excitations to produce a frequency-invariant radiation pattern in a single plane in space, resulting in a "fully-spatial" wideband beamforming. Basically, the delays needed for temporal filtering are compensated by the relative spatial differences between the locations of the elements. Only a single, purely real, weighting coefficient is required for each element, which can be realized by very simple passive or active circuits, eliminating the need for tapped delay lines. This property arises from the symmetry of the pattern in the auxiliary domain, and by assuming that the direction of arrival (DOA) of the signal is known. One of the critical assumptions in this method is the direction of arrival of the signal being in the plane of the planar array. It is assumed that the array forms its beam with reasonable maintenance of the desired performance above its plane, which might not be the case especially over a wide frequency range. Another drawback associated with this method is that, if the electrical size of the array is large, or approaches infinity, the gain of the elements that reside in the far edge goes to zero in the direction of the plane of the array.

Uthansakul and Bialkowski [10] noticed that the method developed by Ghavami in [9] practically does not yield good performance with small array configurations, because the effective aperture area of the array is not large enough to produce adequate directivity. This problem, according to Uthansakul and Bialkowski in [10], can be fixed by increasing the density of the elements in the effective aperture area. Wei [11] noticed that in the method developed by Ghavami in [9], the temporal filtering needed in the design of linear arrays has been replaced by spatial filtering in the planar design because of the additional dimension. By extending the design of the rectangular planar array to a three dimensional array, the problem associated with large arrays that was discussed previously can be resolved. However, another disadvantage arises, that is the blockage of the radiation of the center elements in a large 3-D array environment, which can render the design impractical. Wei, et al. [12] integrated an adaptive optimization algorithm, that is based on linearly constrained minimum variance beamforming (LCMV) [13]. This adaptive element weighting allows for achieving arbitrary beamforming patterns. Adaptive element excitation is discussed in section 2.3. Usually DOA estimation methods are narrowband, such as MUSIC [14]. However, by designing for a frequency-invariant beamformer, narrowband DOA algorithms can be applied at a single frequency and the results can be redistributed over the entire design bandwidth. An example of wideband DOA estimation algorithms is presented by Tuan, et al. in [15].

Another interesting method of achieving frequency-invariant beamforming is to design for a narrowband beamformer, observe how the pattern deviates when the frequency is varied over a wider bandwidth and minimize this variation. For example, in the case of achieving sinusoidal function for the array factor pattern, scaling the frequency parameter will approximately lead to a similar pattern but with scaled width of the main-beam. Yunhong, et al. [16] studied such an effect on the structure of the concentric ring array (CRA). In this study, the weights of the elements in a single ring are designed based on narrowband fast Fourier transform (FFT). On an inter-ring level, the array factor is realized as a Fourier-Bessel series [5], which allows for recognition of dominant higher order Bessel function, and considering only the dominant terms, the analysis becomes much less complicated. The weights on the inter-ring level are designed to achieve wideband performance.

At higher frequencies, the array pattern is naturally widened, but if the array is designed to produce a pre-compressed pattern at higher frequencies, this increase in the width of the main-beam is compensated. The inter-ring weights are used to produce such pre-compressed pattern. A method similar to the concept of pattern pre-compression was applied by Zhu in the study presented in [17] for linear arrays. In the method presented by Zhu in [17], the weight coefficients are calculated at a reference frequency and linearly constrained minimum variance algorithm is used to calculate the weights at other frequencies, so that it produces a pattern similar to that of the reference frequency. Another study that applies the technique of starting the design process at a reference frequency and extending it to the rest of the design bandwidth, is presented by Subramanian in [18]. In [18], the weights are calculated based on minimizing a square error function, that is defined as the cost function, in order to produce weights that result in an optimized pattern close to that of the reference frequency. Constraints other than beamwidth can be embedded in such technique, such as maximum sidelobe level (SLL). Alshammary [19] applied a spatial response variation constraint pattern synthesis algorithm that optimizes the pattern of the array around a reference frequency using a least mean square cost function with maximum SLL and beamwidth as constraints in the algorithm of the design.

Near field applications may also benefit from frequency invariant beamforming. Abhayapala et al. [20] have introduced a wideband beamformer design, consisting of three stages of filtering, that provides the desired beam pattern and the capability of zooming in and out between near-field and far-field regions with essentially the same radiation pattern by expressing the wave equation in terms of spherical harmonics.

Sometimes achieving high directivities is the primary objective in array design. Repetto and Trucco [21] have addressed the importance of providing super-directive radiation patterns, especially when the dimensions of the array aperture are smaller than the wavelength of operation. In [21], a two-step design procedure, involving synthesis of the required finite impulse response (FIR) filters, is presented. The authors in [21] discuss the limitations of the proposed design method; one of the major problems being the difficulty in controlling variations of the radiation pattern with frequency over the desired bandwidth, thus resulting in frequency dependent gain. Crocco and Trucco [22] and Traverso, et al. [23] introduced tunable methods of optimizing the weights of the elements of the array to produce an optimal highly directive pattern

or an optimal frequency invariance performance, based on a trade off between the two properties. Theses optimization methods do not support imposing a desired arbitrary beam pattern.

Ronald [24] has introduced a methodology that provides an approximately frequency-invariant broadside pattern for linear arrays by incorporating a frequency-variant phase parameter into element excitations that minimizes the frequency dependence of the array factor. The method introduced in [24] reduces the dependence of the array factor on frequency to some extent. Exciting different elements in the array over limited regions of the total bandwidth is defined as aperture frequency tapering method. This method, presented by Holmgren et al. [25] and Ouacha et al. [26] provides fairly wideband array radiation patterns.

2.2 Array inter-element mutual coupling

In many array designs aimed at achieving wideband performances, for example an array design intended for a wide scan range over a wide bandwidth, tight inter-element spacing is needed. High levels of mutual coupling due to tight element spacing can result in bandwidth degradation and/or undesirable effects such as alterations in far-field radiation patterns and polarization [4]. One of the major negative effects of inter-element mutual coupling on the performance of an array is variations of the element input impedance with the scan angle [27]; this issue is further discussed in section 2.4.

In some approaches suggested for designing wideband arrays, element mutual coupling is intentionally introduced and is proven to be useful. Using the modeling of phased arrays by infinite current sheets introduced by Wheeler [27] and the concept of frequency selective surfaces (FSS) [28, 29], Munk et al. [30] noted that the mutual impedance between closely spaced dipole elements in an array that is coated with dielectric layers provides wide bandwidths for several array characteristics. In a more recent study, Kasemodel et al. [31] also presented a wideband array design employing the concept of current sheet. Buxton [32] in her dissertation addresses the advantages of inter-element mutual coupling in an array that consists of four-square antenna elements, most notably the increase of impedance bandwidth when enhanced mutual coupling is introduced by tight spacing; the four-square element antenna was designed by Nealy [33]. D. H. Schaubert, et al.[34] and S. Kasturi [35], presented a dense array design that

consists of Vivaldi antennas. In [35], it was discovered that closing the gaps along the sides of the elements by connecting them improves the impedance matching performance of the array. Schaubert et al. [34] introduced a dual polarized Vivaldi array design that included a dielectric layer covering the aperture of the array. This dielectric layer resulted in an increase of the VSWR bandwidth over a wide scanning range, but this improvement was obtained at the cost of added dispersion. Frequency dispersion is a major source of distortion of wideband signals transmitted or received by array antennas. In the studies of dense arrays and tightly coupled elements, which are largely based on numerical analysis techniques, the element mutual coupling is not used as a design parameter and little or no consideration is given to variations of radiation pattern with frequency, thus the arrays are relatively narrow bandwidth which, in turn, result in distortions for broadband signals. Element mutual coupling must be compensated in adaptive array designs intended for wideband signal acquisition.

Extensive studies have been carried out on modeling the element mutual coupling in phased arrays [36-39]. Kelley claims in his thesis [37] that the results provided in Smith's research on mutual coupling in microstrip arrays [36] are not very accurate, largely because of some deficiencies in classical array analysis. In his research, Kelley [37, 38] discusses the concept of active-element pattern as a method of array analysis that accounts for mutual coupling among the elements of the array by taking into consideration the induced currents on the surrounding elements due to the radiation of the active-element. Because radiation characteristics of active-elements are difficult to obtain, Kelley and Stutzman [37, 38] introduced a hybrid method that regards the active element pattern in the center of the array as an average active pattern that approximates the patterns of the surrounding elements while using exact active-element patterns for the edge elements. The hybrid active element pattern method [37, 38] was theoretically tested on an array consisting of seven dipole elements and was shown to yield a high degree of accuracy when compared to measured data. The concept of active-element pattern in a fully active array environment is discussed in Chapter 4 of this dissertation. Using scattering parameters, Takamizawa [39] introduced a network model that allows to model a fully excited array, accounting for mutual coupling not just among the elements but also among their source networks. The model presented by Takamizawa [39] encompasses not only the array as the device under test (DUT) but also the probe antennas used in the measurement setup. Tang and Zhou [40] introduced a method of computing mutual impedance matrices by using multiple base

functions per element using method of moments to solve for the array problem. Complex curve fitting techniques are used if computing the mutual impedance matrix over the entire bandwidth is impractical, as proposed in [40]. Weighted least squares optimization algorithm is used to calculate optimal complex weights of FIR filters in [40] as proposed by the same authors in [41]. As will be discussed in Chapter 4 of this dissertation, mutual impedance is a function not only of frequency, but also element excitations and scan angle. This behavior makes relying on mutual impedance data to compensate for mutual coupling unreliable. However, using S-parameters is more reliable for being only a function of frequency and independent of element excitations. The method proposed in [40] does not take active-element radiation patterns into consideration, which is a parameter that is considered in the proposed synthesis method of this research. An interesting technique that accounts for element response mismatches in achieving frequency-invariant beamforming is presented by Jing and Huawei in [42, 43]. In [42, 43], the response of the element is embedded in least mean square optimization algorithm as a probability density function that is identical for all elements. Such model if incorporated with adaptive element excitation could be useful in inter-element mutual coupling compensation. Sörgel et al. [44] introduced a transient array response formulation that includes the effect of element mutual coupling and the influence of the transient response of the single element in the array. Such a model is useful when array analysis is less computationally intensive if carried out in time domain.

Mutual coupling between the elements and the feed network and also mutual coupling between the ports of the feed network can have significant impacts on radiation characteristics of wideband arrays and should be accounted for. Takamizawa [39] and other researchers have discussed various techniques for compensating mutual coupling in array systems including their passive feed networks. Most of the mutual coupling compensation techniques presented by these researches yield satisfactory results over narrowbands, thus are not adequate when dealing with wideband array systems. Adaptive element excitation technique, discussed in section 2.3 and also in the proposed synthesis technique in this dissertation, offers a convenient solution for mutual coupling compensation in wideband array systems. However, it is not easy to model the adaptive feed network theoretically and measurement based methods are the most effective tools in this case. Ertel et al. [45] presented a systematic technique on how to compensate for phase shifting errors caused by phase shifters and splitters in the array system. The data needed to

determine these errors are obtained through array boresight measurements. The same method can also be used to compensate for mutual coupling in antenna arrays and their associated feed networks. A method similar to that introduced in [45] was presented by Deshuang et al. [46], but instead of performing measurements in the frequency domain, a time reversal technique is used. Time reversal is a process in which the spectrum of a transient signal received by array elements is calculated using Fourier transform. In both [45] and [46] the received signal implicitly includes information about element mutual coupling and other undesired factors that affect the radiation characteristics of an array. If the array is of a manageable size, element mutual coupling measurements can be performed easily by measuring the scattering matrix of the array system by using a multi-port test set (MTS) as described in the work presented by Tanyer-Tigrek et al. [47]. An overview of research activities aimed at wideband beam forming has been presented by Gershman [48]. Some studies mentioned in [48] have addressed and formulated analysis and design techniques for adaptive beam forming taking into account signal interference, noise, and other array imperfections. Mutual coupling in passive feed networks is significant particularly at high frequency bands such as those operating in Ka band, i.e. 26.5 GHz-40 GHz. Such effects of mutual coupling may increase insertion loss of feed networks. Techniques such as substrate integrated waveguide (SIW), introduced by Puskely and Mikulasek in [49], where holes are strategically placed on the conducting layer of a feed network of Vivaldi array in order to provide better isolation. Other techniques such as the use of electromagnetic band gap structures (EBG) [29] can be effective in providing isolation between ports of feed networks at high frequencies.

2.3 Frequency-adaptive element excitation

The examination of array factor expression, that will be discussed in Chapter 3, indicates that in order to achieve wideband array performance, or to provide frequency-invariant beam forming, the use of frequency-variant element excitation proves useful. This frequency-adaptive element excitation is mostly implemented through the use of adaptive filters that are also used in the signal processing field as discussed in section 2.1. In fact, frequency-variant excitations are also important for operating individual wideband antennas. Pozar [50] has studied the effects of pulse shaping on maximizing the amplitude of the voltage received at the terminals of a receiving antenna as well as maximizing fidelity of the received signal. The results in [50]

emphasize the importance of pulse shaping and waveform optimizations at the transmitter for maximizing the voltage amplitude at the receiving antenna, especially when adhering to wideband communication standards such as FCC UWB signal regulations which are discussed by Schantz [51]. If pulse-shaping and waveform optimization is performed on a real-time basis, the result is an adaptive system that yields optimal performance dynamically.

Generation of frequency-adaptive element excitations is an important task in the wideband array design. The use of tapped delay lines (TDL) is one of the most common techniques in generating frequency varying signals. The operation of a TDL consists of extracting a signal at a specific point on a delay line and possibly scaling it to a desired level needed for an element excitation. The benefits of TDLs in wideband array designs have been demonstrated in many studies. Marciano et al. [52] presented a technique for linear array pattern synthesis using a synthesized TDL that is capable of producing an essentially constant radiation pattern over a wide frequency range. Several studies have also considered TDL synthesis as an integral part of adaptive array designs. Most of the presented results in these studies indicate that the designs are, to a large degree, successful [53-56].

One obvious drawback of using TDLs in wideband array designs is the lack of real-time adaptivity which maintains system robustness and real time reconfiguration, unless discrete switching techniques are employed. Maintaining real-time hardware reconfiguration requires real-time computational capabilities. Riza [57] introduced a photonic I-Q vector modulator that generates the desired radio frequency (RF) signals with accurate phase and amplitude values. Field programmable gate array (FPGA) is another popular computer peripheral technology that offers vast hardware reconfiguration capabilities. Recent research in wideband array design has recognized the usefulness of FPGAs in providing adaptive element excitations that are required to produce wideband array performance. The advantages of real-time hardware reconfiguration are explained very well by Joler et al. [58]. The main idea of the design presented in [58] is to develop a real-time self-recoverable thinned array by embedding a genetic algorithm (GA) code in an FPGA to recover the desired radiation pattern. Chiba et al. [59] designed a digital beam forming (DBF) system for mobile satellite communications using custom-designed FPGAs This design resulted in a significant size reduction in the DSP engine of such systems and eliminated the need for phase shifters. Fischman et al. [60] used FPGAs to design an electronically steerable

DBF for a synthetic aperture radar (SAR) and a moving target indication (MTI). Xin-Huai et al. [61] demonstrated how real-time reconfiguration can enhance the performance of anti-jamming beam formers in GPS systems. Harter and Zwick [62] have introduced a DBF radar system for 3D imaging employing FPGAs to provide simultaneously the required data read-out and system control. Fournier et al. [63] achieved electronic scanning through the use of FPGAs connected to a Butler matrix feed networks that produce narrow orthogonal beams with good directivity in microstrip antenna arrays. Weber and Huang [64] presented a frequency agile circular array of dipole elements for high speed communications between buoys and ships. In [64], the computational capabilities of the FPGA have been used to provide real time continuous corrections required to compensate for changes in the system introduced by random motion and interferences.

It should be mentioned that while using certain devices may facilitate the production of frequency-adaptive RF signals needed for element excitations of wideband arrays, but they may also introduce more complexity into the system and thus higher costs. Alwan, et al. [65] developed an array design technique that employs code division multiplexing (CDM) in order to reduce the complexity and large power requirements usually associated with beamforming hardware. In the design presented in [65], before the signal is digitized, or before the analog to digital conversion (ADC) stage, CDM is used to uniquely identify each signal associated with every element antenna in the array. This technique allows for the use of a single ADC unit in the beamforming system instead of using one for each element antenna. After the ADC stage, the composite signal is decelerated using the same CDM. Under ideal conditions, if the CDM codes are perfectly orthogonal, the cross-correlation between the coded signals is zero. If the number of elements increases, inter-channel interference becomes more effective, and the performance can be improved by increasing the number of orthogonal codes in the system. Another important consideration in array beamformer hardware design is the dynamic range of element excitation. Horrell and du Toit [66] discussed the involvement of the dynamic range of element excitation, the ratio between maximum and minimum voltage level, as a constraint along with beamforming using population-based incremental learning (PBIL) optimization algorithm.

In an interesting study Ward, et al. [67] analyzed the properties of a filter used for frequency-invariant sensor arrays. In [67], it was concluded that the relationship between filters

at different sensor locations is a "dilation," or frequency scaling of a primary filter design, assuming that the elements of the array are isotropic. Ihsan and Solbach [68] used the results provided by Ward, et al. in [67] to design a UWB array that consists of printed monopole element antennas. In [67], an approximately constant width for the main-beam was achieved over the UWB frequency range, but accompanied by grating lobes that tend to get closer to the main-beam at the higher end of the UWB range, an issue that is typical in UWB arrays. Exploiting the properties presented by Ward, et al. in [67] with the use of FIR filters, a primary filter can be used while the required filter transfer function for different elements can be achieved through multirate sampling techniques. This method was introduced by Ward, et al. in [69], where the performances of two frequency-invariant array designs were compared, one designed based on the multirate sampling and the other using a single sampling rate. In [69], it was concluded that the multirate method requires fewer filter coefficients, but at the cost of requiring higher sampling rate, which sometimes might be too expensive to implement. Forcellini and Kohno [70] applied the same method presented in [69] but with using an infinite impulse response filter (IIR), which may reduce the cost of the design of the frequency-invariant beamformer drastically. Key differences between the FIR and the IIR filters are discussed in Chapter 7 of this dissertation.

2.4 Array main-beam scanning

Conventionally, main beam scanning is achieved through introducing a relative phase difference or relative time delay between the elements of an array. Many phase shifter designs have been introduced in the antennas and microwave engineering disciplines [71]. One of the most notable techniques of providing frequency-independent beam scanning is that based on the beam forming matrix. As introduced by Rufenach et al. [72], the beam forming matrix consists of a grid of transmission lines coupled by capacitors in a way that allows signal passing for each pre-selected main beam direction over a specific bandwidth. Photonic devices and fiber optics are also known for their superb accuracy in providing relative phase shifts between elements. Frankel et al. [73] introduced an array design that utilizes fiber optics for two dimensional beam steering. Phase shifting can also be provided by the use of RF oscillators. Liao and York [74] presented an array design consisting of coupled oscillators that provide a constant phase progression between the element excitations of an array.

In large arrays, time delay units necessary to achieve main-beam scanning may occupy large space, which may lead to requiring larger real estate than the radiating section of the array itself. Haupt in [75] addresses the relationship between the performance of a wideband planar array and size and distribution of "time-delay units" (digital bits) that are used to provide the required time delays for the elements of the array. In [75], the approach for determining the real estate limitations associated with the size of these time-delay units is to digitize the time delay range by estimating the maximum delay required and the resolution between the delays of the elements. This way, time-delay units can be dealt with as digital bits associated with certain lengths of microstrip delay lines, then by combining specific time-delay units the required amount of time delay for each element of the array is obtained. The most significant bit (MSB) represents the largest time-delay unit and the longest delay microstrip line, while the least significant bit (LSB) represents the smallest time-delay unit and the shortest delay microstrip line. Combination of these bits results in achieving the time delay needed by a certain element with some degree of accuracy depending on the quantization error that is directly related to the number of bits used to represent a single time-delay unit. The size of a time-delay unit is constrained to a single unit cell in the planar array, i.e. the area of the cell that connects four elements whose centers are equally-spaced along the principal axes of the array. The first few most significant bits, which represent longer time delays, may occupy large spaces and it would be impractical to use them separately for each element. In [75], the placement of large time-delay bits is on a subarray level and shared between the elements of the array. Large sidelobes, designated as quantization lobes, appear with increased size of time-delay unit subarrays. Quantization errors in time-delay units can also be a source of wideband signal distortions. The effects of such errors are discussed by Haupt in [76] and by Corbin and Howard in [77]. Another effective method of minimizing the number of time-delay units is to divide the array into subarrays, as proposed by Bianchi, et al. [78]. On the subarray level, the elements are in phase, and only one time-delay unit is used for each subarray to provide relative phasing between subarrays. If the subarrays are identical, the total array factor is equal to the multiplication of the array factor of the main array configuration and that of the subarray. The appearance of grating lobes is dependent on the spacing between the contiguous subarrays. In [78], a method of overlapping subarrays is introduced. The overlapping is achieved by sharing one or more of the edge elements between the subarrays, which leads to inter-subarray spacing that is smaller than

the minimum achievable spacing when the subarrays do not overlap. The subarrays could be randomly overlapped, using an optimization process, in order to break the periodicity of the main array and achieve better suppression of grating lobes.

Array main-beam scanning over wide bandwidth is essential in many wideband applications, such as estimating DOA of wideband signals. Techniques such as beamspace division, in which beamformers are synthesized to cover certain region in space where the source signal is expected to lie, rely on frequency-invariant beamforming and wideband main-beam scanning within that specific region. Reproducing identical radiation patterns within the scanning region and the desired bandwidth is essential for signal processing in beamspace division systems, as explained by Lee in [79]. Usually FIR filters are used to achieve frequency-invariant beamforming in beamspace division systems. Yan and Hou [80] tested achieving frequency-invariant patterns within the region of the main-beam and not necessarily in the sidelobe region, while constraining the sidelobe level to a certain maximum. The optimization method used in [80] has resulted in smaller main-beam synthesized error in the frequency-invariant beamforming when the results are compared to those published in [79]. Liu et al. [81] extended the concept of beamspace division to two-dimensional arrays. Ward et al. [82] presented a technique of beamspace processing using beamforming filters in time domain, eliminating the need for frequency domain decomposition. The technique in [82] is reliant on the fact that beamforming of the systems is frequency-invariant, which leads to the avoidance of designing for beam steering filter weights at each frequency. Beamspce division techniques if combined with adaptive array systems can be useful in interference suppression. Sekiguchi and Karasawa [83] proposed an adaptive beamspace division technique using adaptive FIR fan filters. Each frequency-invariant beam is controlled by a FIR fan filter [84] with 2-dimensional adaptive weights, one dimension corresponds to the location of the element antenna in the array and the other corresponds to the number of delay unit that precede the weight factor in the FIR filter of a single element antenna. The weights of the FIR fan filters are optimized using LMS algorithm. The technique proposed in [83] was successful in accommodating signals with up to 100% fractional bandwidth. Liu et al. [85] addressed one more important condition, namely linear independency, for beamforming in beamspace division techniques other than frequency-invariance. The beams formed by a beamspace division array should be linearly independent, otherwise some of the beam outputs are just a linear combination of the other beams, which

reduces the number of effective beams and lead to reduction of the capabilities of the array in isolating interfering signals. As it is proven in [85], there is a trade-off between frequency-invariance and linear independency of beams. Frequency-invariance properties of beams may need to be sacrificed to some degree in order to improve interference cancellation capabilities by enhancing linear independencies between different beams.

The input impedances of active elements of an array are affected by main beam scanning according to inter-element mutual coupling, as mentioned in section 2.2. Mutual coupling compensation through the use of frequency-adaptive element excitation can help in eliminating the effect of beam scanning on the input impedances of active-elements. In order to achieve the desired scanning range over a wide frequency range, free of grating lobes, usually the element spacing is minimized. However, with the elements placed close to each other, inter-element mutual coupling becomes more effective. Inter-element mutual coupling is an important issue especially in dense array systems, such as the foursquare array introduced by Buxton [32] and the Vivaldi array by Kasturi [35]. Appearance of grating lobes in the high frequency range of wideband arrays is largely due to the periodicity of the array factor as a function of space and frequency. Unequal element spacing or nonperiodic array design techniques, combined with optimization algorithms, might be helpful in suppressing grating lobes and achieving the desired scanning range over the desired bandwidth. Gregory and Werner in [86] have presented a method of converting the periodic function of the array factor of a linear array to a power series by replacing the constant element spacing with a factor raised to an optimized power. This factor is also a function of the location of the element that was originally placed in an equally spaced array. The method presented in [86] was tested for a linear array with equally excited elements. A bandwidth of 20:1 was achieved with array factor free of grating lobes. A maximum sidelobe level criterion was embedded in the optimization algorithm presented in [86]. However, in [86], the width of the main-beam varies within the design bandwidth, which is a minor issue if the width of the main beam is very narrow. In a study presented by Gregory et al. [87], a semi-periodic technique is used for designing circular arrays. In [87], the location of the elements inside a sector of the circular array is optimized and then the circular sector is rotated based on standard periodic lattices to fill the circle of the array. The results in [87] show a significant suppression of grating lobes over the bandwidth of design. Another common technique in improving the performance of wideband arrays is the use of fractal geometry. Gregory et al., [88]

employed such techniques in order to optimize the design of the array factor of a linear array. The design process in the technique presented in [88] starts with a set of generators terminated with connection factors that determine which generator to be connected in the next stage. Progressing to a higher order stage is controlled by optimization algorithms. The design technique proposed in [88] was applied to a linear array that consisted of 1959 elements, and a 28:1 bandwidth was achieved with a 60º scanning angle, free of grating lobes.

2.5 Energy-directing arrays

Radiated electromagnetic energy is most commonly analyzed using time domain techniques. In some applications, achieving maximum radiation with a desired direction and time duration, in which the energy is radiated, are considered the only goals of the design. Of course, in such systems, the issues pertaining to information signals for wireless communications is not a concern. One of the early studies on maximizing radiated energy from wire dipole arrays in a specific direction and a specific duration of time was carried out by Yoon-Won and Pozar [89]. Optimal element excitation signals were obtained to produce an endfire or a broadside beam with or without sidelobe level constraints. The relationship between the ratio of the radiated energy in a specified time duration to the total radiated energy and the bandwidth of the system has been investigated in [89]. Inter-element mutual coupling was compensated for using an optimization method. Since the main goal in the study presented in [89] was to provide maximum radiated energy and not wideband signal transmission, signal distortion was not a concern. Ciattaglia and Marrocco [90] introduced a time-domain pattern synthesis technique in which Radon transforms, explained by Johnson and Dudgeon in [91], were used to calculate element excitations required to produce a specific array factor. In [90] the array element is regarded as an ideal differentiator, which is not a very accurate representation especially when effects such as element phase and inter-element mutual coupling is to be compensated.

Chapter 3: Synthesis of Linear Arrays with Specified Bandwidths

As a first step toward the ultimate goal of designing ultra-wideband two-dimensional arrays, this chapter focuses on the synthesis of linear arrays with bandwidth as the main design requirement. The array factor is formulated as a Fourier series expansion in order to facilitate the calculation of element excitation currents. The array factor, over a desired frequency range and in a specified direction in space, is defined as a function of frequency based on the bandwidth requirements of the design. The synthesis approach allows for compensating frequency-dependent variations of the array element radiation characteristics.

3.1 Formulation of the array factor

Let us consider a linear array consisting of $2N+1$ isotropic equally-spaced elements with element currents $I_n = |I_n| e^{j\alpha_n}$; $n = 0,\ \pm 1,\ \pm 2, ..., \pm N$, and element spacing d. The center of array is assumed to coincide with the origin. Figure 3.1 illustrates the geometry and coordinates for such an array. In the far-field region, the array factor is simply sum of the fields radiated by the array elements. Excluding the propagation term $e^{-j\beta r}/4\pi r$, the array factor can be expressed as [4-6],

$$AF(\omega,\theta) = \sum_{n=-N}^{N} I_n e^{jn\beta d\cos\theta} \qquad (3.1)$$

where $\beta = \omega\sqrt{\mu_o \varepsilon_o} = \omega / c$ is the propagation constant, with c being the speed of light in free space, and θ is the elevation angle measured from the line of array.

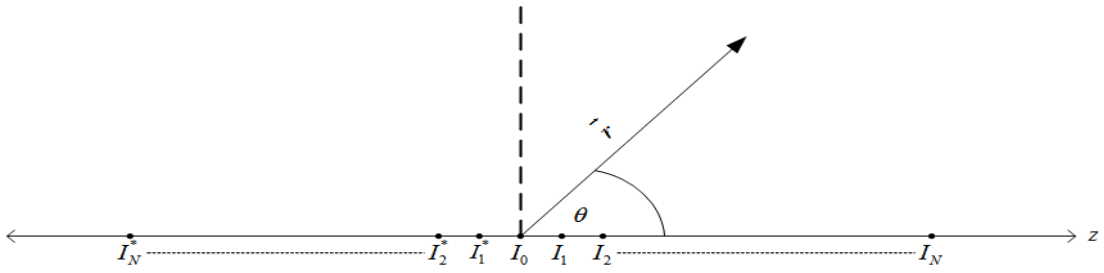

Fig. 3.1: Geometry and coordinates for a linear array of $2N+1$ isotropic elements

Examination of (3.1) reveals that the right hand side of the array factor equation may be regarded as a truncated Fourier series expansion. Furthermore, the array factor becomes purely real if the currents of symmetrically spaced elements are complex conjugates of each other; that is, $I_{-n} = I_n^*$. In this case, the array factor can be written as

$$AF(\omega,\theta) = I_0 + \sum_{n=1}^{N} I_n e^{jn\beta d\cos\theta} + I_n^* e^{-jn\beta d\cos\theta} = I_0 + 2\sum_{n=1}^{N} |I_n| \cos(n\beta d\cos\theta + \alpha_n) \quad (3.2)$$

Equation (3.2) is the array factor for an odd number of elements. If the number of elements is even, the array factor may be obtained from (3.2) by setting $I_0 = 0$ and replacing *nd* with $(n-0.5)d$ in it [4]. To facilitate the calculation of excitation coefficients I_n, we compare (3.2) with the trigonometric form of the Fourier series written as

$$AF(\omega,\theta) = a_0 + \sum_{n=1}^{N} a_n \cos[n\beta d\cos\theta] + b_n \sin[n\beta d\cos\theta] \quad (3.3)$$

where $a_0 = I_0$, $a_n = 2|I_n|\cos\alpha_n$, $b_n = -2|I_n|\sin\alpha_n$. If the element phasing is chosen to be $\alpha_n = 0$ or $\alpha_n = \kappa\pi$; $\kappa = 0, \pm1, \pm2, \pm3, \ldots$, then it is readily noted that $b_n = 0$ and (3.3) reduces to

$$AF(\omega,\theta) = I_0 + 2\sum_{n=1}^{N} I_n \cos(n\beta d\cos\theta) \quad (3.4)$$

3.2 Synthesis of arrays with specified radiation patterns

If in (3.4) the frequency is fixed at ω_o, the array factor may be regarded as a truncated Fourier series expansion of a desired array pattern defined by the function $f(\theta)$; that is,

$$f(\theta) = AF(\theta,\omega_0) = I_0 + 2\sum_{n=1}^{N} I_n \cos\left(\frac{d}{c}\omega_o n\cos\theta\right) \quad (3.5)$$

The elements excitation currents are calculated as follows.

$$I_0 = \frac{1}{T_\theta}\int_0^{\pi} f(\theta)\cdot\sin\theta d\theta \quad (3.6)$$

$$I_n = \frac{1}{T_\theta}\int_0^{\pi} f(\theta)\cos\left(n\frac{2\pi}{T_\theta}\cos\theta\right)\cdot\sin\theta d\theta \tag{3.7}$$

where $T_\theta = 2\pi c / d\omega_0$. More details on the design of linear arrays with prescribed radiation patterns can be found in [4-6]. It is also evident from (3.5) that, at a fixed value of θ, the array factor can be regarded as a Fourier series expansion in the frequency domain with ω as the variable. This case is investigated in the next section.

3.3 Synthesis of arrays with prescribed bandwidth requirements

In a specific direction, θ_o, the array factor of the array in Fig. 3.1 can be expressed as a function of frequency with the following trigonometric Fourier series expansion.

$$AF(\omega) = I_0 + 2\sum_{n=1}^{N} I_n \cos\left(\frac{d}{c}\omega n\cos\theta_o\right) \tag{3.8}$$

The element excitations are calculated by using the following equations.

$$I_0 = \frac{2}{T_\omega}\int_{\omega_1}^{\omega_2} AF(\omega)d\omega \tag{3.9a}$$

$$I_n = \frac{2}{T_\omega}\int_{\omega_1}^{\omega_2} AF(\omega)\cos\left[n\left(\frac{2\pi}{T_\omega}\right)\omega\right]d\omega \tag{3.9b}$$

where

$$T_\omega = \frac{2\pi c}{d\cos\theta_o} \tag{3.9c}$$

To calculate the excitation currents I_0 and I_n in (3.9a) and (3.9b), the array factor function $AF(\omega)$ should be specified first. This depends on the frequency response characteristic that the array is desired to have. For ultra-wideband array designs, the array factor is specified such that the total radiated field in a given direction $\theta = \theta_0$, which is the product of the array factor and the radiated field of the array element, remains constant over a desired frequency range $\omega_1 < \omega < \omega_2$. The frequency dependence of the array factor within the desired bandwidth can be determined

such that the effects of the field of the element antenna are compensated. Clearly, such an array lends itself to wideband and ultra-wideband designs, depending upon to what extent the bandwidth limitations of the array element can be reasonably compensated. This aspect will be elaborated upon further in the ensuing discussions.

Let us consider an array element whose radiated field magnitude in a given direction, $|\vec{E}_e(\omega,\theta_o)|$, varies with frequency ($\omega_1 < \omega < \omega_2$) as an arbitrary function shown in Fig. 3.2a. For the total radiated field of the array to remain constant over the frequency range $\omega_1 < \omega < \omega_2$, the array factor should be inversely proportional to $|\vec{E}_e(\omega,\theta_o)|$, that is

$$AF(\omega,\theta_o) = \left[|\vec{E}_e(\omega,\theta_o)|\right]^{-1} \tag{3.10}$$

Next, a square-wave like periodic function is formed such that it is an even function of ω and its period T_ω is chosen to be larger than $2(\omega_1+\omega_2)$, as shown in Fig. 3.2b. Using the array factor function given by (3.10) in integral expressions in (3.9a) and (3.9b), the element excitation currents are readily determined. It is noted from Fig. 3.2b that for a specified upper frequency of the desired bandwidth ω_2, the minimum value of the period is $(T_\omega)_{\min} = 2\omega_2$. Moreover, from the expression for T_ω in (3.9c), it is noted that the choice of T_ω directly impacts the inter-element spacing d. In particular, the maximum inter-element spacing is limited to

$$d_{\max} = \frac{2\pi c}{(T_\omega)_{\min}\cos\theta_o} \tag{3.11}$$

Also, from the series expression in (3.8), one can notice that the larger the number of elements, $2N+1$, the more accurately the truncated Fourier series can approximate the array factor. In the next section, the impact of the number of elements on the accuracy of the array factor is examined more thoroughly.

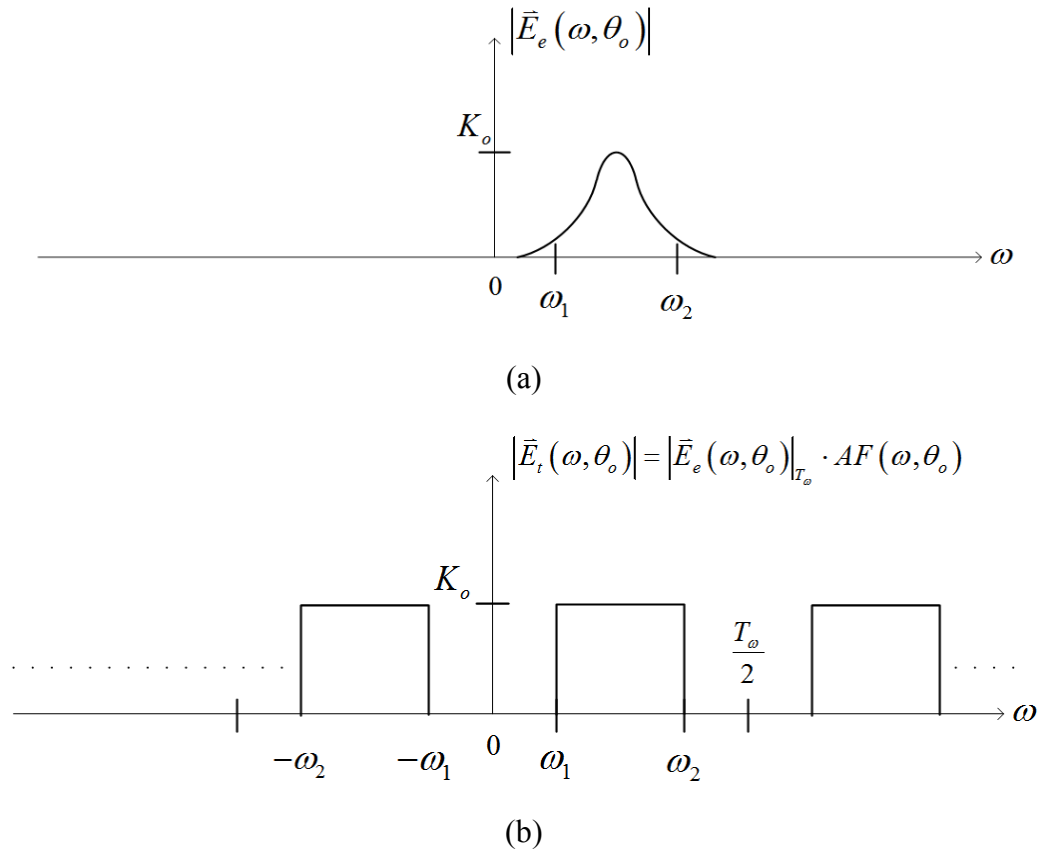

Fig. 3.2: (a) Variations of the magnitude of the element field with frequency, (b) magnitude of the total field of the array as a square-wave like periodic function

3.4 Design examples for linear arrays with specified bandwidths

To demonstrate the application of the formulation developed in the previous section, design examples for linear arrays of equally-spaced elements with desired bandwidths are presented. Initially, the elements are assumed to be isotropic. Figure 3.3 shows the results for variations of the array factor and directivity versus frequency for two design examples of linear arrays of equally-spaced isotropic elements with $N = 15$ (31 elements) and two values of the inter-element spacing d (d =13.64 mm and d =15 mm). In these examples the desired bandwidth of the array is 9 GHz along the direction $\theta = \theta_0 = 0^\circ$, covering a frequency range of 1 GHz to 10 GHz. Figures 3.3a and 3.3c show three dimensional plots of the magnitude of the normalized array factor versus θ and frequency. A planar top view projection of the 3-D plot of the array factor is also included in these figures to show some of the hidden details in the lower 3-D plots. Examination of Figures 3.3a and 3.3c indicates that the array factor remains essentially

unchanged over much of the in-band frequencies in the range f_1=1 GHz to f_2=10 GHz, particularly over a narrow angular range about $\theta = 0^\circ$. It is further noted that as the frequency increases, the angular region over which the array factor is nearly constant becomes wider, and as the upper frequency of 10 GHZ is approached this angular region covers $0^\circ \le \theta < 60^\circ$. Furthermore, for the design with $(T_\omega)_{\min} = 2\omega_2 = 4\pi f_2 = 40\pi$ Grad/s, the array factor in Fig. 3.3a has more sidelobes than that of the design with a larger value of T_ω shown in Fig. 3.3c. Also, comparison of Figs. 3.3a and 3.3c reveals that the ripples, which result from Fourier series truncation, are less in the array designed with $(T_\omega)_{\min} = 40\pi$ Grad/s and tend to decrease as the frequency increases. Grating lobes are present over almost the entire desired bandwidth; they emerge when $120^\circ < \theta \le 180^\circ$ for lower frequencies in the bandwidth and $90^\circ < \theta \le 180^\circ$ for higher frequencies. The emergence of grating lobes at smaller values of θ for higher frequencies is due to the fact that the element spacing in terms of wavelength is larger at higher frequencies than that at lower frequencies. The grating lobes can be eliminated through multiplication of the array factor and the element pattern. In the next chapter, the elimination of grating lobes by using frequency adaptive excitation techniques is discussed.

The directivity at each frequency is calculated using the following equation [4]

$$D(\omega) = \frac{2}{\int_0^\pi \left[\frac{|AF(\omega,\theta)|}{|AF(\omega,\theta_{\max})|} \right]^2 \sin\theta \, d\theta} \tag{3.12}$$

where $\theta_{\max}$ is the angle at which the magnitude of the array factor function is maximum. Figures 3.3b and 3.3d illustrate variations of the directivity versus frequency for the design examples in Figs. 3.3a and 3.3c, respectively. Both designs exhibit similar directivity performance, with 3-dB bandwidth of 3.1 GHz to 10.6 GHz which is the frequency range considered for ultra-wideband (UWB) applications. A major limitation of the design method presented in this chapter is the restriction on the inter-element spacing, *d*, as stated in (3.11). If d exceeds its maximum value given in (3.11), the frequency performance of the array over the specified bandwidth is deteriorated.

The number of elements of the array $(2N+1)$ is a determining factor on how well the array factor and hence the directivity of the array remain constant over the specified bandwidth. Figure 3.4 shows different spatial cuts of the magnitude of the array factor for different numbers of elements. It is observed that as the number of elements increases, for a given value of θ, (i) the array factor exhibits less variations with frequency within the design bandwidth, (ii) the achieved bandwidth becomes larger while not exceeding the desired design bandwidth, and (iii) the ripples become smaller in amplitude but larger in number. These phenomena are all due to truncation of the Fourier series representing the array factor; that is, finite number of terms in the series corresponding to finite number of elements in the array. Also, examination of the plots in Fig. 3.4 at angles away from $\theta = \theta_o$ indicates that as θ increases the bandwidth tends to broaden and shift toward higher frequencies. From a mathematical point of view, this effect may be attributed to the presence of the term $\omega \cos\theta_0$ in the Fourier series representation of the array factor, as noted in (3.8). Since $\cos\theta_0$ decreases with θ_0 , $0^\circ \le \theta_0 \le 90^\circ$, for larger values of θ_0 the center frequency of the bandwidth should occur at higher values, thus a shift of the bandwidth to the right along the frequency axis.

The element excitation currents required to produce the array factors shown in Fig. 3.4 are given in Fig. 3.5. Using (3.9a) and (3.9b) it can be shown that, if $\theta_o = 0$ and $AF(\omega)$ is chosen to be constant within the frequency range $\omega_1 < \omega < \omega_2$, then $I_n = 0$ for odd values of n and I_n follows a discrete *sinc* function for even values of n. The sinc-function-like behavior seen in Fig. 3.5 is a familiar feature associated with the Fourier transform of rectangular pulses. Accordingly, amplitude tapering of the element currents away from the array center is necessary in order to achieve the required frequency-invariant array factor over the specified bandwidth. The decision on limiting the number of elements of the array can be based on the array factors shown in Fig. 3.4 and how well the desired performance is achieved. Another useful information that helps in making reasonable decisions on array truncation is the significance of the current excitations shown in Fig. 3.5 and realization of the fact that elements closer to the center have a much stronger impact on the array factor than those closer to the edges of the array.

The synthesis example presented above involved isotropic elements with no bandwidth limitation (that is infinite element bandwidth). However, in practical applications the elements

have a limited bandwidth that is often less than the desired bandwidth of the array. One of the key features of the array synthesis technique presented in this chapter is the ability to compensate for frequency variations of the field of the element antenna over the specified bandwidth and achieve an overall array bandwidth larger than the bandwidth of constituent elements. To demonstrate the effectiveness of element bandwidth compensation, the synthesis method is applied to a linear array of half-wave wire dipoles, with length $L = 0.48\lambda_r$, at $f_r = 5.5$ GHz. Figure 3.6 shows the reflection coefficient and the realized gain of a wire half-wave dipole antenna made to be resonant approximately at $f_r = 5.5$ GHz. The half-power frequencies of the dipole are $4.7\,\text{GHz}$ and $7.64\,\text{GHz}$. Figure 3.7 compares the total fields radiated by the arrays of wire dipoles with different numbers of elements. The dipoles are assumed to be parallel to the y-axis with their centers located on the z-axis. It is emphasized that inter-element mutual coupling is not considered here. Compensation of inter-element mutual coupling is discussed in the next chapter. Since the fields of all elements are assumed to be identical in the present discussion, pattern multiplication principle, stated in (3.13), is applied to produce the total fields shown in Fig. 3.7.

$$\vec{E}_{tot}(\theta,\omega) = \vec{E}_e(\theta,\omega)\cdot AF(\theta,\omega) \tag{3.13}$$

where $\vec{E}_e(\theta,\omega)$ is the field of the dipole element antenna and $\vec{E}_{tot}(\theta,\omega)$ is the total field of the array. Also in Fig. 3.7, the total-field of a uniformly-excited equally-spaced linear array (UEESLA) that consists of the same number of dipole elements is included for comparison. For UEESLA, the array factor is obtained from the following equation [4],

$$AF(\omega,\theta) = \frac{\sin\left(N_0\Psi/2\right)}{N_0\sin\left(\Psi/2\right)} \tag{3.14}$$

where $\Psi = (\omega d/c)(\cos\theta - 1)$ and $N_0 = 2N+1$ which produces an endfire beam.

It is emphasized that the array factor used in determining the element excitation currents for the array of wire dipoles in Fig. 3.7 is based on (3.10). This ensures that frequency variations of the realized gain of the wire dipole are compensated over the desired frequency range of $4.7\,\text{GHz} < f < 7.64\,\text{GHz}$. Comparison of plots in Fig. 3.4 with those in Fig. 3.7 indicates that,

apart from the significant impact of the narrow realized gain bandwidth of the wire dipole on the overall bandwidth of the array, the influence of the number of elements on the frequency response characteristics of the array remains the same. In particular, ripples with smaller amplitudes for larger number of elements and bandwidth broadening as well as shifting to higher frequencies at larger values of θ_0 occur in the same manner in both cases.

Figure 3.7 also illustrates the total radiated field of a uniformly-excited equally-spaced array of wire dipoles with N=100. It is noted that the radiated field of this array generally varies rapidly with frequency, causing significant distortion on wideband signals, whereas the array designed based on the technique presented here indeed provides a bandwidth much larger than that of the dipole element and will allow radiation of wideband signals with much less distortion.

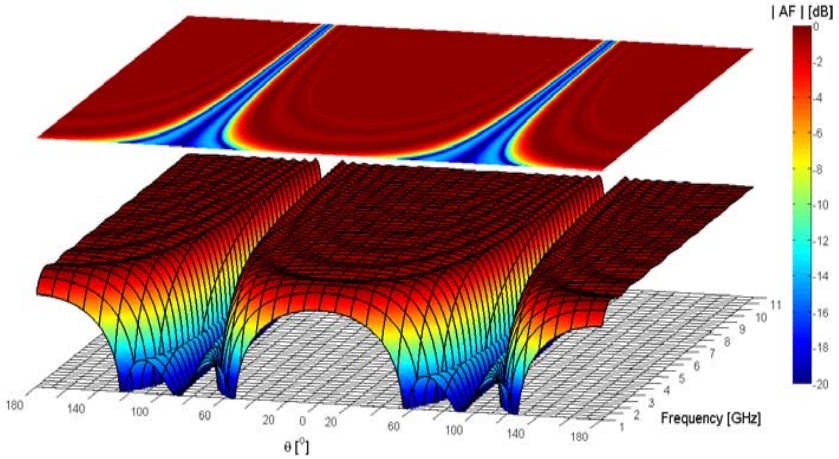

(a) $T_\omega = (T_\omega)_{\min} = 4\pi f_2$, $d_{\max} = 15.00$ mm

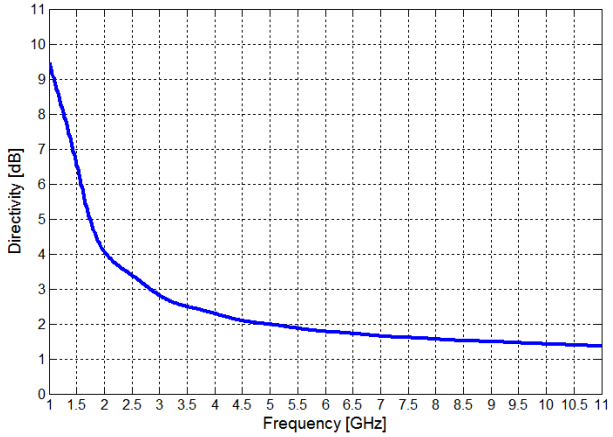

(b) $T_\omega = (T_\omega)_{\min} = 4\pi f_2$, $d_{\max} = 15.00$ mm

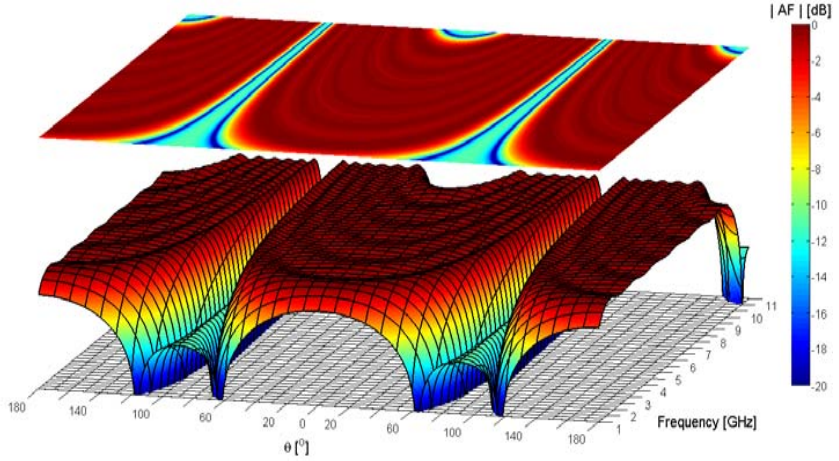

(c) $T_\omega = 4\pi(f_1 + f_2)$ **and** $d = 13.64$ mm

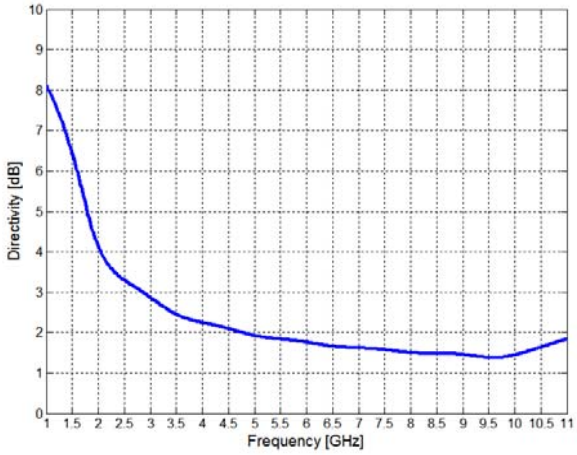

(d) $T_\omega = 4\pi(f_1 + f_2)$ **and** $d = 13.64$ mm

Fig. 3.3: Variations of array factor and directivity for linear arrays of isotropic elements with 31 elements ($N = 15$), element spacing d=15 mm for (a) and (b) and d=13.64 mm for (c) and (d). The desired bandwidth is 9 GHz at $\theta = 0^\circ$ with lower and upper frequencies of $f_1 = 1\text{GHz}, \text{and } f_2 = 10\text{GHz}$.

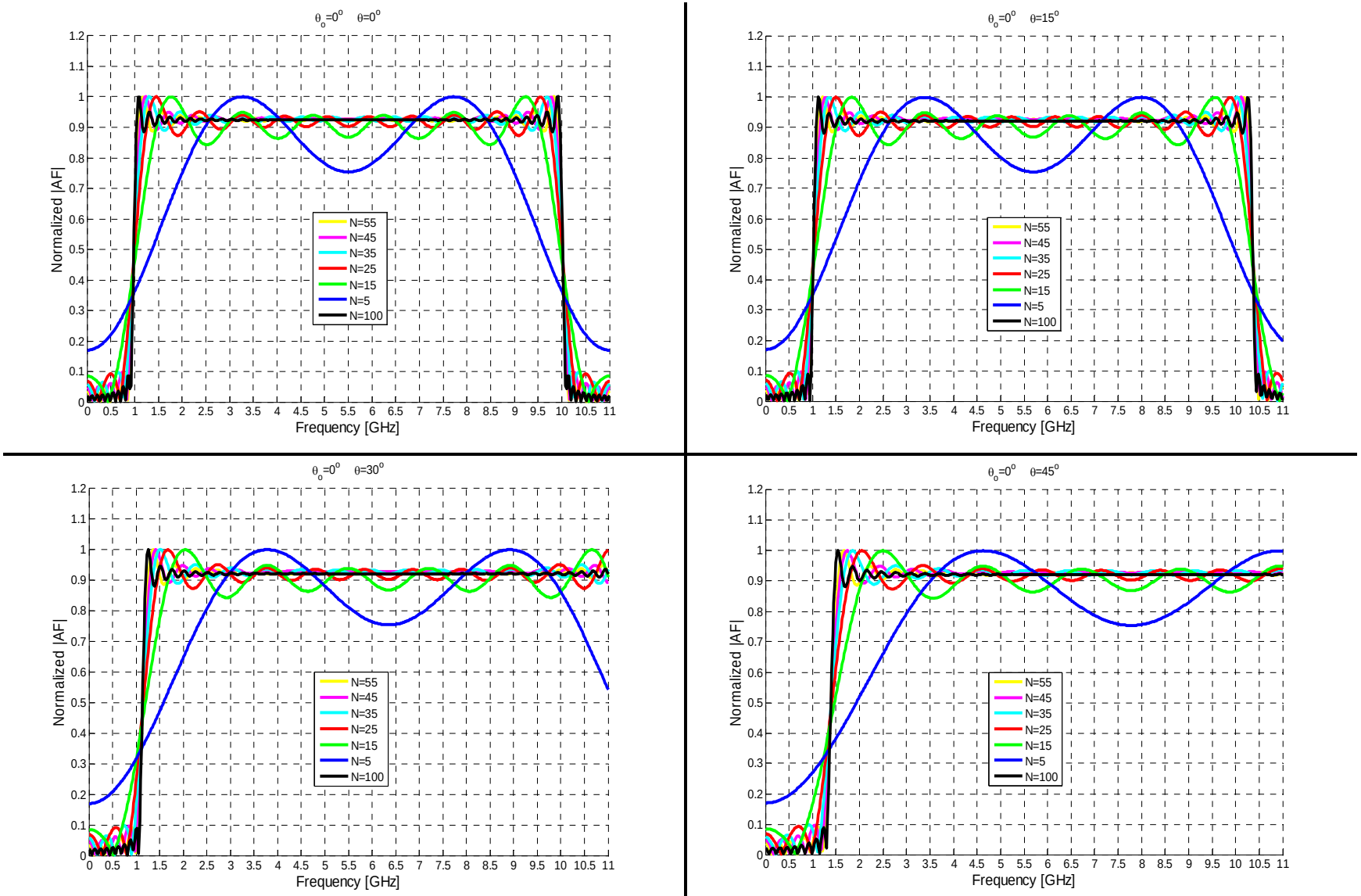

Fig. 3.4: Variations of array factor versus frequency for different values of θ and different numbers of elements (2N+1). The element spacing is d=13.64 mm, the desired bandwidth is 9 GHz at $\theta = 0^{\circ}$ with lower and upper frequencies of $f_1 = 1\text{GHz}$, and $f_2 = 10\text{GHz}$, and $T_{\omega} = 4\pi(f_1 + f_2)$

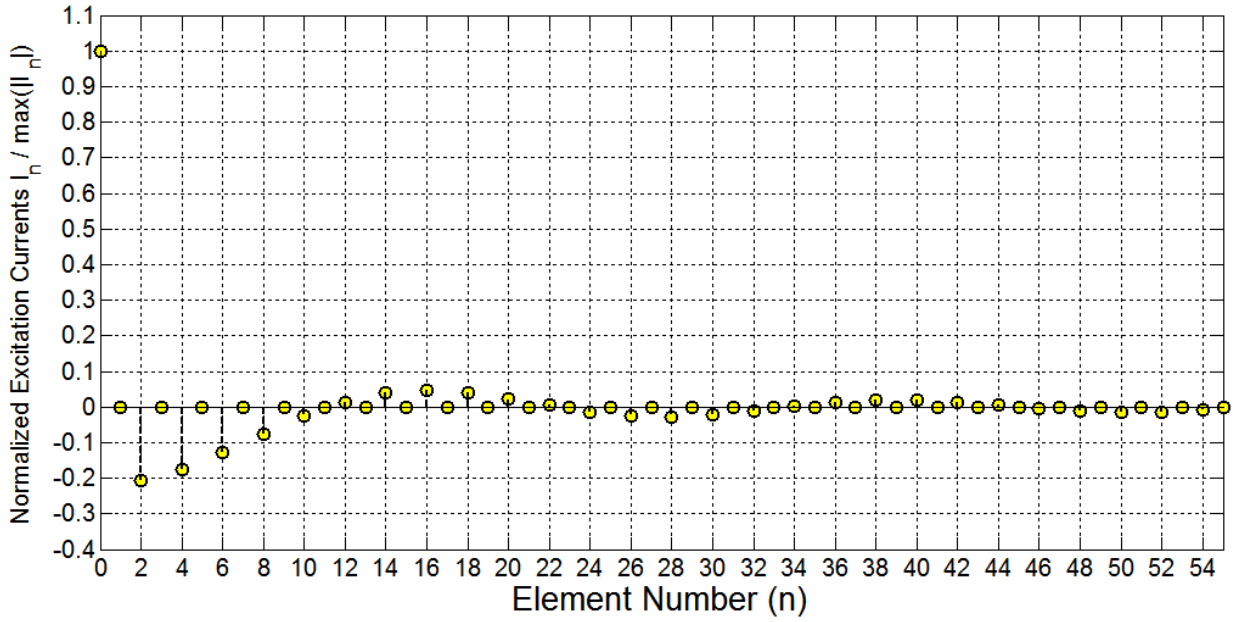

Fig. 3.5: Element current distributions required to produce the array factors shown in Fig. 3.4. All parameters used in calculating these currents are the same as those in Fig. 3.4.

In summary, arrays designed based on the method of non-uniform excitation presented in this chapter provide the specified 3-dB bandwidth with reasonable accuracy particularly for larger number of elements, while the UEESLA design, with the exception of the case $\theta = 0^{\circ}$ for which the array factor becomes unity, provides a poor wideband characteristic. Our synthesis technique will be further developed and expanded in next and subsequent chapters

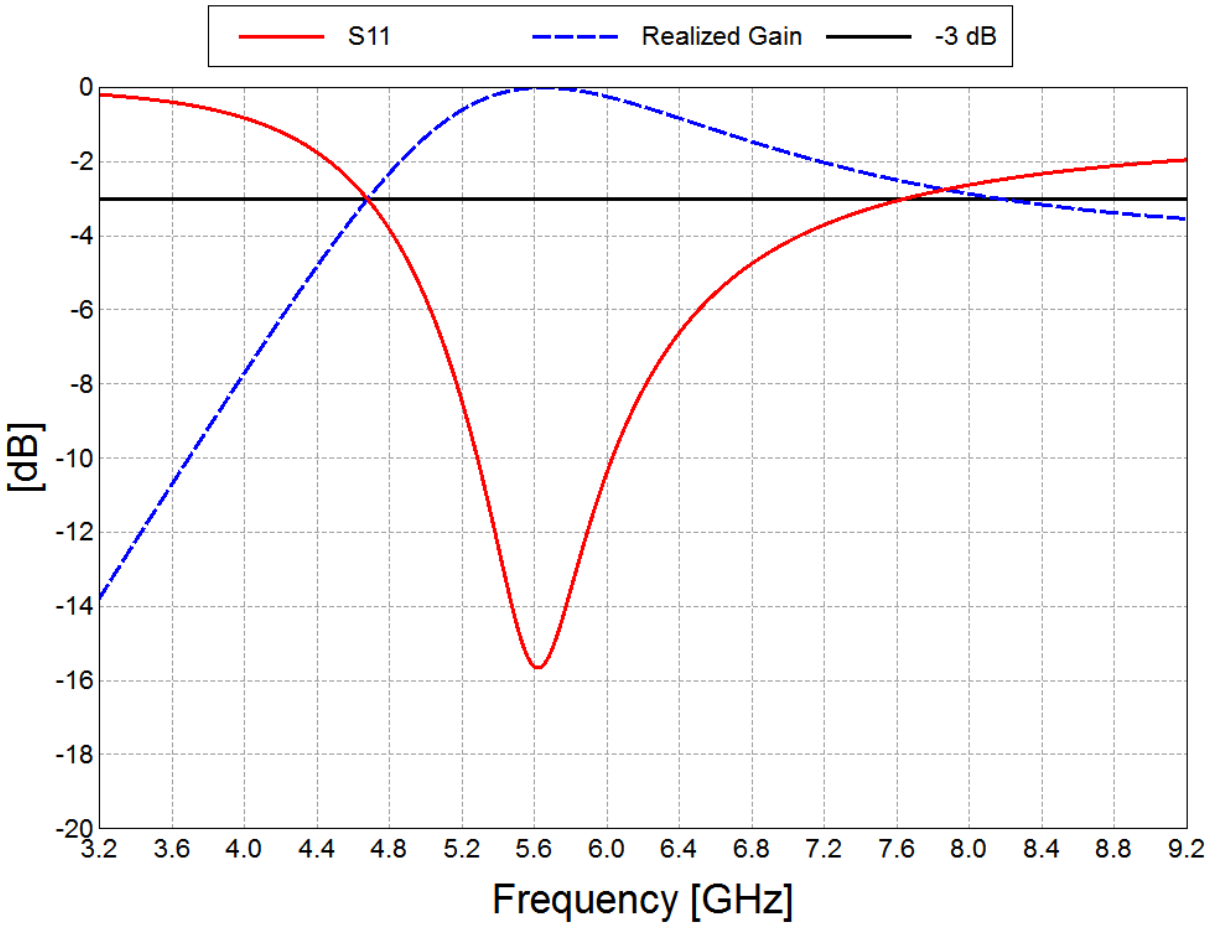

Fig. 3.6: Variations of normalized S_{11} and realized gain versus frequency at $\theta = 0^{\circ}$ for a wire dipole antenna as array element. The dipole is resonant at $f_r = 5.5$ GHz (length=2.73cm= $0.48\lambda_r$) and has a radius of 0.5 mm.

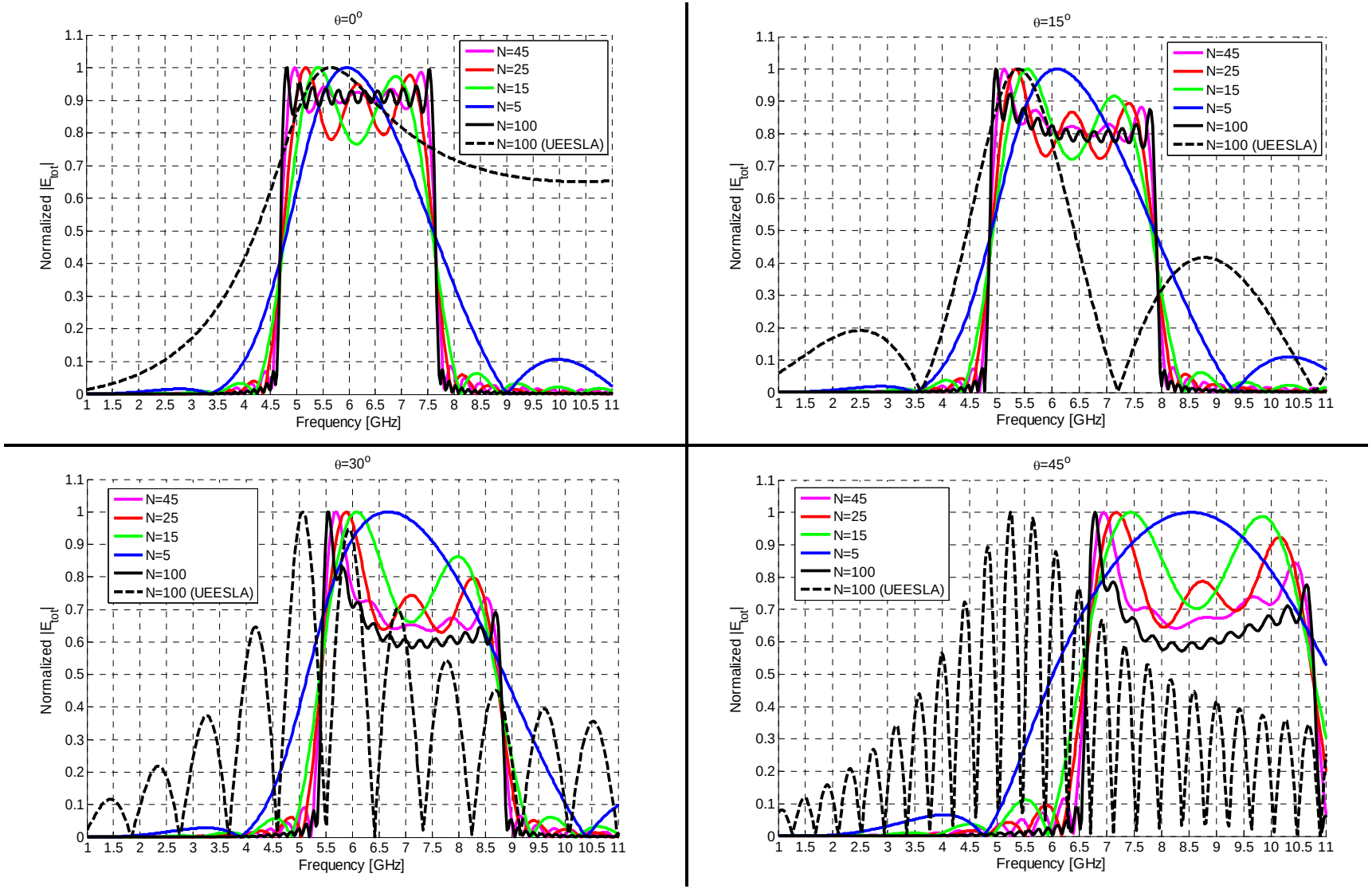

Fig. 3.7: Variations of the total radiated field of arrays of wire dipoles resonant at 5.5 GHz versus frequency for different values of θ and different numbers of elements (2N+1). The design parameters are: d=13.64 mm, $\theta = 0^{\circ}$, $f_1 = 4.7$ GHz, $f_2 = 7.64$ GHz , and $T_{\omega} = 4\pi\left(f_1 + f_2\right)$. Also, the total radiated field of an equally-spaced uniformly excited array of same wire dipoles with N=100 is shown for comparison.

Chapter 4: Synthesis of Arrays Using a Frequency-Adaptive Method

In the synthesis technique presented in Chapter 3, bandwidth was the main design requirement used in determining the array element currents. In this chapter, a frequency-adaptive synthesis method is introduced that allows including not only the required bandwidth but also the desired radiation pattern which in turn may contain such information as beamwidth, sidelobe level, nulls in certain directions, directivity, etc. It is shown how frequency-adaptive excitation can be employed to provide frequency-invariant total array patterns. It is also explained how this method can be used to compensate for the effects of the field of the element antenna, its input impedance, and inter-element mutual coupling on the overall bandwidth of the array.

4.1 Frequency-adaptive element excitation

Let us consider a linear array with the same geometry, parameters, and symmetry properties as that shown in Fig. 3.1. If the array factor in (3.4) is sampled discretely in the frequency domain, it may be re-written in the following form:

$$AF_p(\theta) = I_{0p} + 2\sum_{n=1}^{N} I_{np} \cos\left(\frac{d}{c}\omega_p n \cos\theta\right) \qquad (4.1)$$

where $\omega_p = \omega_l + p(\Delta\omega)$; $p = 0,1,2,3,...,P$; $\Delta\omega$ is a constant frequency increment, and $\omega_h - \omega_l$ defines the bandwidth of the array with ω_h and ω_l being the upper and lower radian frequencies (corresponding to p=0 and p=P, respectively). It is noted that the right-hand-side expression in (4.1) can be regarded as a truncated Fourier series expansion in the θ-domain at a single frequency sample ω_p. The element excitations can be calculated at each frequency sample to produce an array factor that closely approximates a desired function of θ. This method, in principle, allows for producing frequency-invariant array factors with arbitrary radiation patterns; $AF_p(\theta) = f(\theta)$ for all p. Introducing the spatial period $T_p = 2\pi c / d\omega_p$, element excitation currents can be calculated as Fourier series coefficients using the following equations.

$$I_{0p} = \frac{1}{T_p}\int_{u_1}^{u_2} AF_p(u)\,du = \frac{1}{T_p}\int_0^{\pi} f(\theta)\sin\theta d\theta \tag{4.2}$$

$$I_{np} = \frac{1}{T_p}\int_0^{\pi} f(\theta)\cos\left(n\frac{d\omega_p}{c}\cos\theta\right)\cdot\sin\theta d\theta \tag{4.3}$$

The minimum value of the spatial period of the Fourier series, corresponding to the upper frequency of the array bandwidth ω_h, is:

$$T_P^{\min} = \frac{2\pi c}{d\omega_h} \tag{4.4}$$

It is emphasized that in (4.2) and (4.3) the function $f(\theta)$ is assumed to be zero outside the range $\theta \in [0,\pi]$ in order for the basis functions of the Fourier series in (4.1) to remain orthogonal through out the bandwidth of interest.

The element spacing should be adjusted to a value such that grating lobes are avoided and tolerable sidelobe levels are maintained. This point will be discussed further in the next section.

In order to have a better appreciation of the proposed technique, a design example for an ultra-wideband array with prescribed bandwidth and radiation pattern is presented. The array is desired to produce a frequency-invariant broadside beam over a bandwidth of 1 GHz to 10 GHz (includes L-, S-, C-, and part of X-bands). In this example $N = 22$ is assumed. To calculate the element excitation currents, we need to specify the array factor as a function of θ. We choose a sinusoidal function that provides a highly directive radiation pattern as defined below:

$$AF(\theta,\omega) = f(\theta) = \sin^m\theta, \quad \text{with} \quad m = 50 \tag{4.5}$$

The half-power beamwidth for this pattern is $HP \approx 13.5^\circ$. For this array, in order to avoid grating lobes at the highest frequency in the bandwidth ($f_h = 10$ GHz) it is necessary that, as will be shown later, the element spacing satisfies the relationship $d \le \lambda_h/2$, where $\lambda_h = c/f_h = 3\times10^8/10\times10^9 = 3\ cm$; that is, $d \le 1.5\ cm$. Here $d = 1\,cm$ is chosen.

The next step is to calculate the element excitation coefficients using (4.2) and (4.3). In doing so, integrations are carried out numerically. Also, truncation errors due to the finite numbers of elements can be compensated (to some degree) by modifying the element excitation coefficients in such a manner that the array factor along the direction of the main beam ($\theta = \theta_o$) remains unchanged versus frequency over the bandwidth of the array. Accordingly, the modified excitation coefficients are determined as follows.

$$I_{0p\_mod} = \frac{I_{0p}}{\left|AF_p\left(\theta_o\right)\right|} \tag{4.6}$$

$$I_{np\_mod} = \frac{I_{np}}{\left|AF_p\left(\theta_o\right)\right|} \tag{4.7}$$

Figure 4.1 shows the calculated array factor (AF) using the current distributions in (4.6) and (4.7), while Fig. 4.2 illustrates the element excitation coefficients as functions of frequency needed to produce the array factor of Fig. 4.1. A closer examination of Fig. 4.1 reveals that the beamwidth at the lower frequencies exhibits some broadening accompanied by low-level sidelobes that vanish rapidly when approaching the higher frequencies of the bandwidth. This beam broadening and side lobe occurrences are due to residual truncation errors caused by the limited number of elements in the array. It is emphasized that these errors were compensated only for the main beam direction, thus occurrence of side lobes (away from the main beam) and a small broadening of the main beam should be expected. It is shown later in this section that these errors can be significantly reduced by increasing the element spacing.

To achieve main beam scanning, a phase shift is embedded in the element excitation coefficients in (4.6) and (4.7). The direction of the main beam shifts from $\theta = \theta_0$ to $\theta = \theta_s$ if the array factor is modified to the following expression.

$$AF_{p\_mod}\left(\theta\right) = I_{0\_mod} + 2\sum_{n=1}^{N}\left|I_{np\_mod}\right|\cos\left[\left(nd\omega_p / c\right)\left(\cos\theta - \cos\theta_s + \cos\theta_0\right) + \alpha_{np}\right] \tag{4.8}$$

where θ_s is the desired scan angle. Accordingly, the following element excitation coefficients will produce the desired array factor in (4.8). It is reminded that the condition $I_{(-n)p\_mod} = I^*_{np\_mod}$,

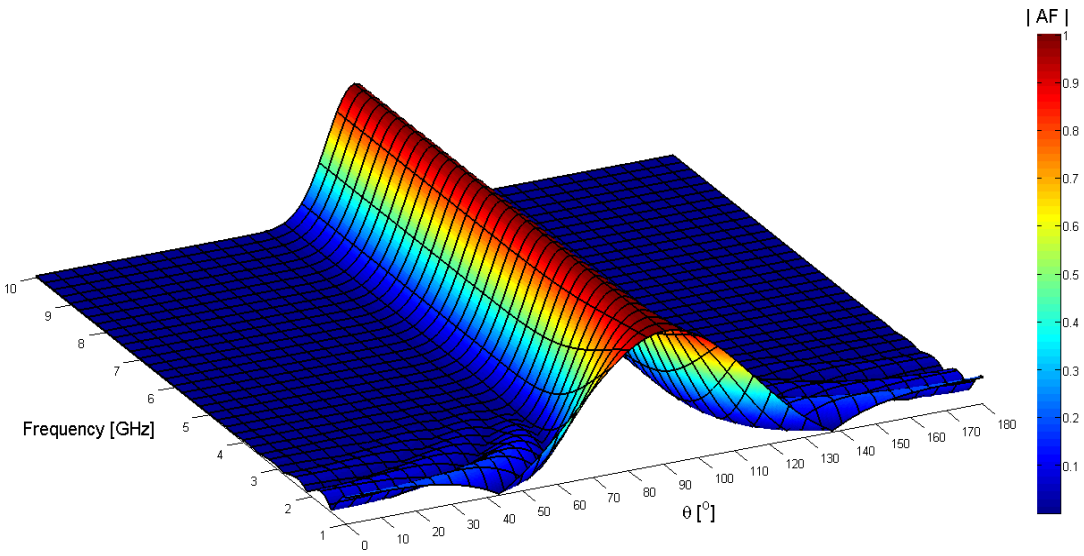

(a)

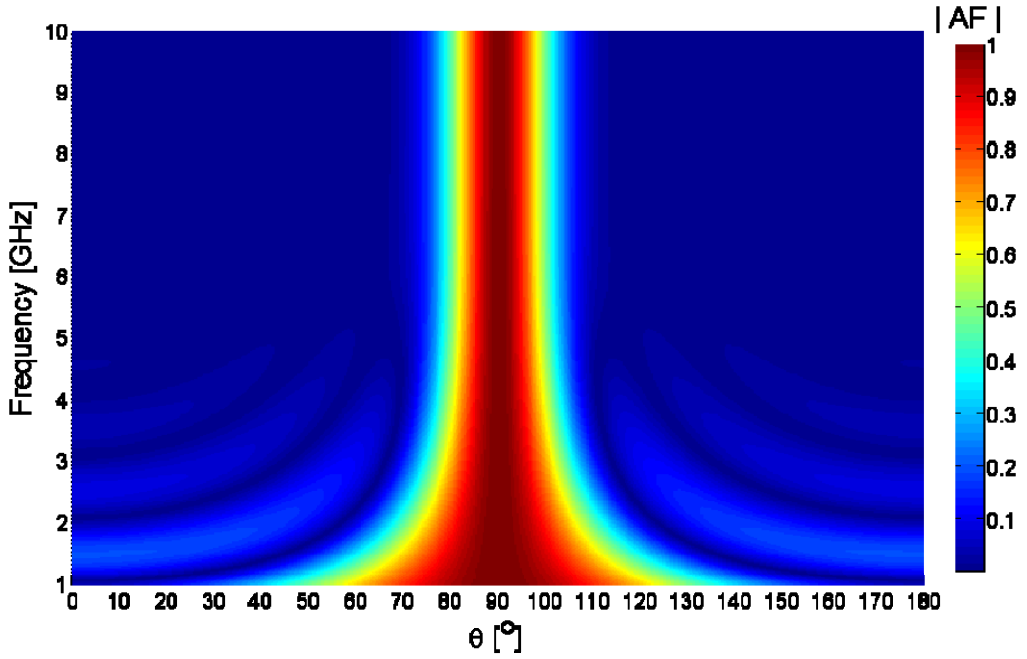

(b)

Fig. 4.1: Variations of the calculated array factor (|AF|) versus frequency and angle θ for a linear array with 45 isotropic elements (N=22) and element spacing $\mathrm{d} = 1\ \mathrm{cm}$ **. The desired array pattern is described by** $AF = \sin^{50}\theta$ **over a frequency range of 1GHz to 10GHz. (a) Three-dimensional view, (b) top view**

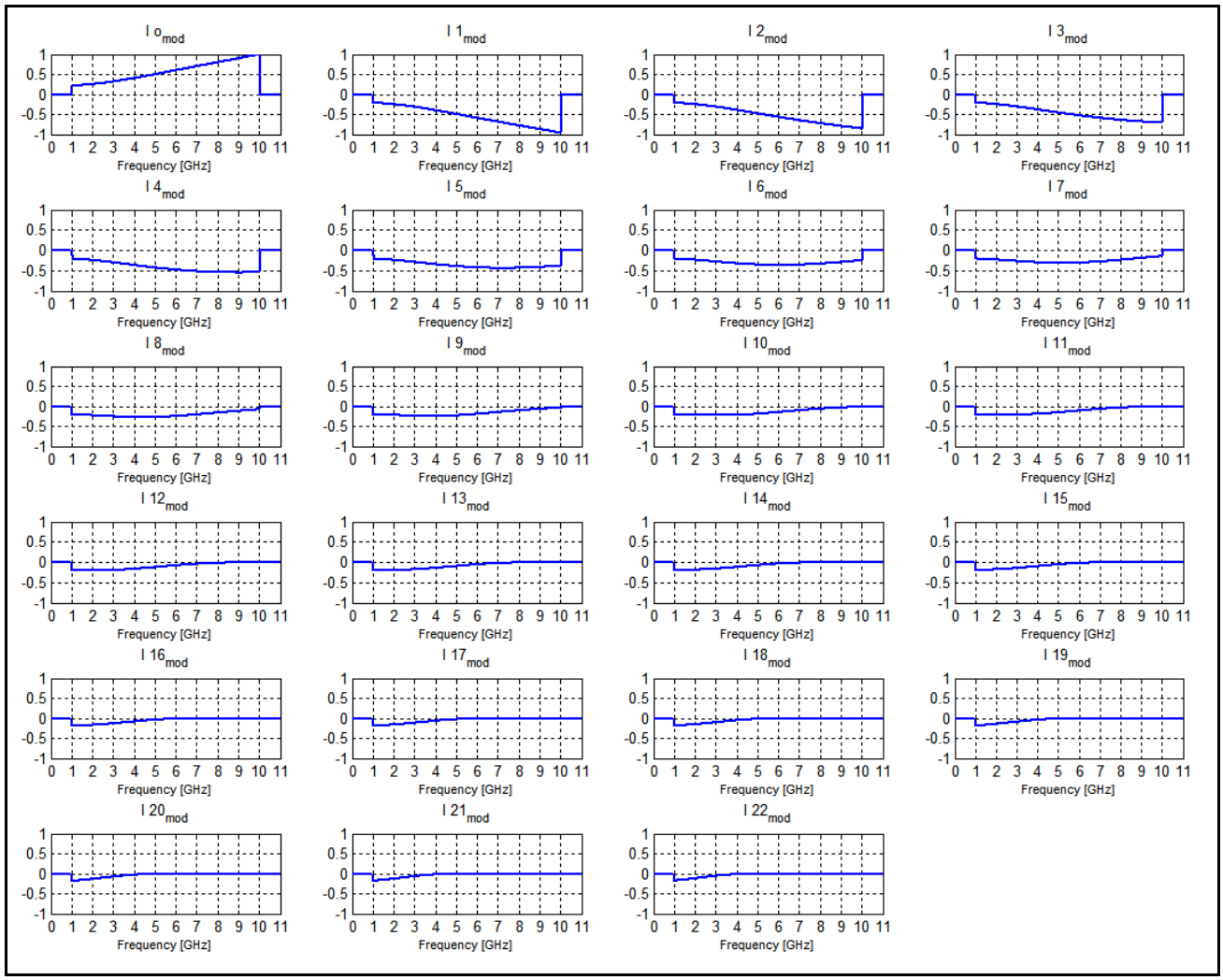

Fig. 4.2: Element currents (normalized to $|I_{0,mod}|_{\max}$) required to produce the array factor $AF = \sin^{50}\theta$ for the linear array of Fig. 4.1 (N=22, d=1 cm)

which was first applied in developing the array factor in (3.2), continues to be required here as well.

$$I_{np\_mod} = \frac{|I_{np}|}{|AF_{p\_mod}(\theta_s)|}\exp\left[-j(nd\omega_p/c)(\cos\theta_s - \cos\theta_0) + j\alpha_{np}\right] \qquad (4.9)$$

Figure 4.3 shows the array pattern for a scan angle of $\theta_s = 40^\circ$ with element currents calculated by using (4.9). It is reminded that in this case the desired array factor is expressed as

$AF_p(\theta) = \sin^{50}(\theta + 50^\circ)$. There is a somewhat broader beamwidth in this case compared to the case of $\theta_o = 90^\circ$ shown in Fig. 4.1. This is partly due to the Fourier series truncation error that is larger for scan angles away from the broadside direction $\theta_o = 90^\circ$.

It might be desirable to increase the element spacing as much as possible for various reasons; for example, to decrease inter-element mutual coupling and reduce the number of elements. The major limitation on element spacing is the emergence of grating lobes. The occurrence of such lobes is directly related to the visible range of the array factor, which may be more conveniently described if the array factor in (4.1) is viewed as a function of $\psi = d\omega_p \cos\theta / c$. Clearly, in the ψ-domain, the array factor is periodic with a period of 2π. The visible range $0 \le \theta \le \pi$ in the ψ-domain corresponds to $\left(\psi_0 - 2d\omega_p / c\right) \le \psi \le \psi_0$, where ψ_0 is a constant whose value depends on the direction of the main beam of the array pattern and the maximum allowed sidelobe level. For the design example of (4.5), $\psi_0 = \pi$ and to avoid grating lobes and also have no sidelobes over the entire bandwidth the relationship $2d\omega_h / c \le 2\pi$ should be satisfied, as demonstrated in Fig. 4.4a. Note that, the visible range, the diameter of the semicircle in Fig. 4.4a is $2d\omega_h / c$. This relationship may be expressed as a requirement that the element spacing must satisfy; namely, $d \le \left(\pi c / \omega_h = \lambda_h / 2\right)$, where $\lambda_h = 2\pi c / \omega_h$. However, if a sidelobe level $SLL \le SLL_{\max}$ is tolerated, then parts of grating lobes can be included in the visible range as shown in Fig. 4.4b. In this case, $2d\omega_h / c \le \left(2\pi + 2\psi_1\right)$, where ψ_1 is the point at which the relationship $|AF_h(\psi_1) / AF_{h-\max}| = SLL_{\max}$ is satisfied. Thus, the element spacing can be increased to a larger value.

For element spacing much larger than $\lambda_h / 2$, grating lobes become unavoidable. This is observed in Fig.4.5 which shows the array pattern produced by the element excitations used in Fig. 4.1 with $d = 5\,cm$ instead of $d \approx 1\,cm$. As expected, grating lobes appear at higher frequencies of the bandwidth and are absent at the lower frequencies. This array design can still be useful but over a reduced bandwidth of 1 GHz to 5 GHz instead of 1 GHz to 10 GHz. The reduction of bandwidth becomes even larger for main beams away from the broadside direction

as noted in Fig. 4.6 which shows a pattern with its main beam occurring at $\theta = 67.5^{\circ}$. It is noted in Fig. 4.6 that the bandwidth is reduced to 1 GHz to 4 GHz. This result indicates that if the main beam scans the angular region $67.5^{\circ} \le \theta < 112.5^{\circ}$ (corresponding to a full scan range of 45° about the broadside direction $\theta = 90^{\circ}$) the useful bandwidth of the array with $d = 5$ cm will be 1 GHz to 4 GHz. Examination of Figs. 4.5 and 4.6 indicates that a major factor contributing to bandwidth reduction at a certain scan angle is the occurrence of grating lobes.

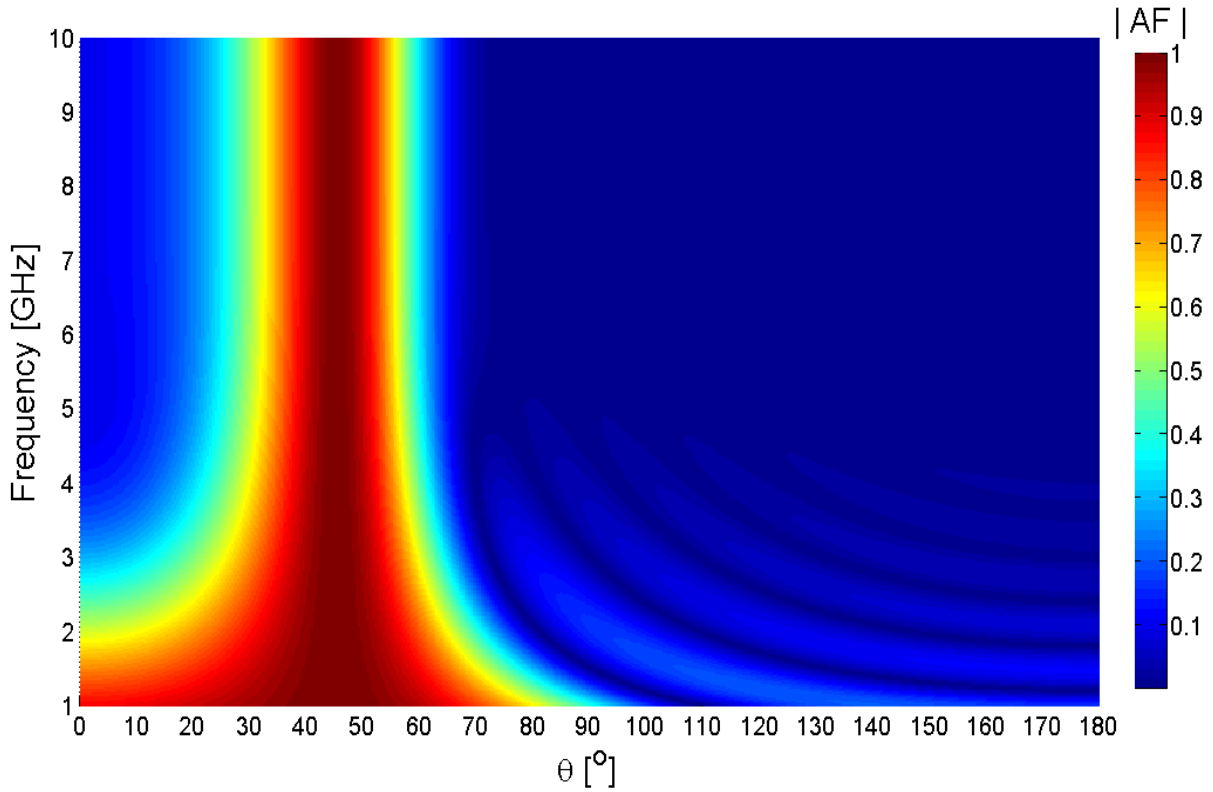

Fig. 4.3: Variations of the array factor (|AF|) versus frequency and angle θ for the array of Fig. 4.1 but with scan angle $\theta_s = 40^{\circ}$

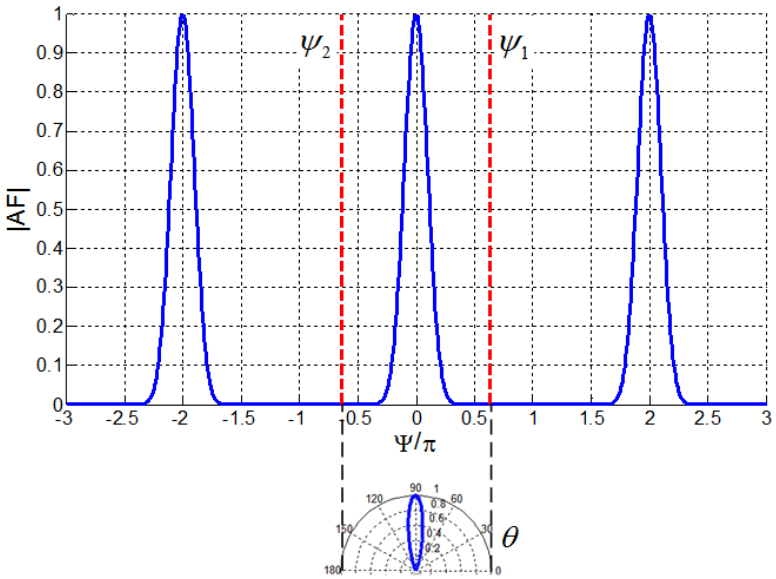

(a)

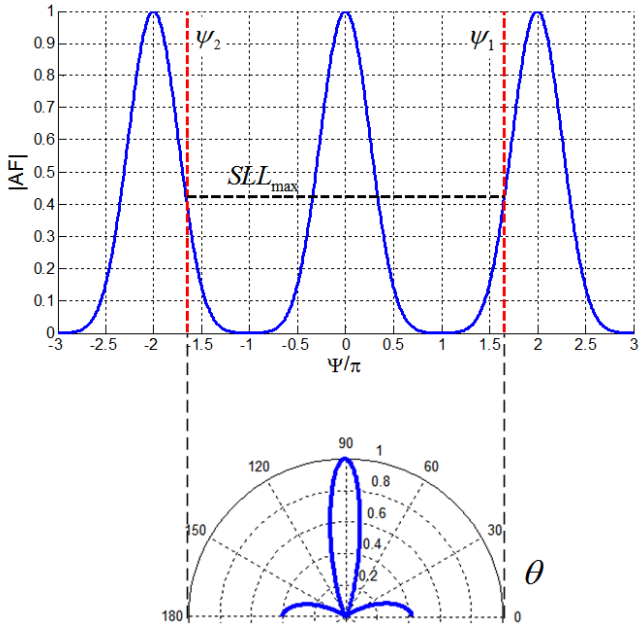

(b)

Fig. 4.4: Illustration of the emergence of grating lobes in the pattern of an arbitrary array factor and its relationship to element spacing d, $\psi_1 = \psi_o$ **,** $\psi_2 = \psi_o - 2(\omega_h / c)d$ **,** $f_h = 10$ GHz **. (a)** d = 1 cm **, (b)** d = 2.6 cm

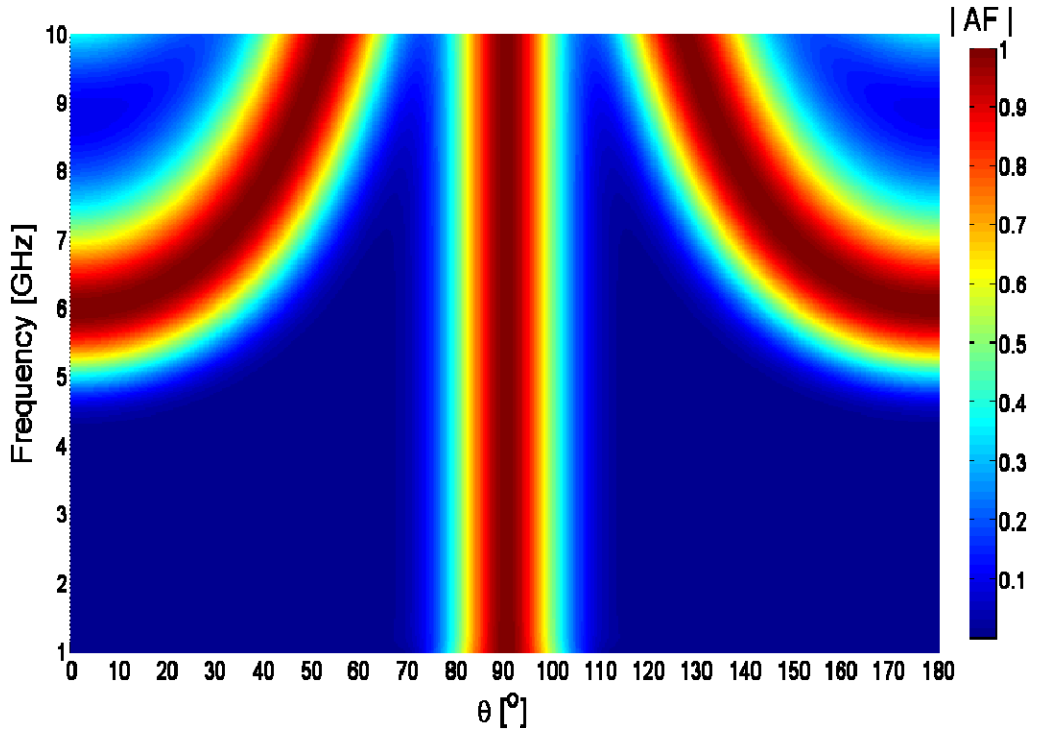

Fig. 4.5: Variations of the array factor (|AF|) versus frequency and angle θ for the array of Fig. 4.1 but with element spacing d=5 cm

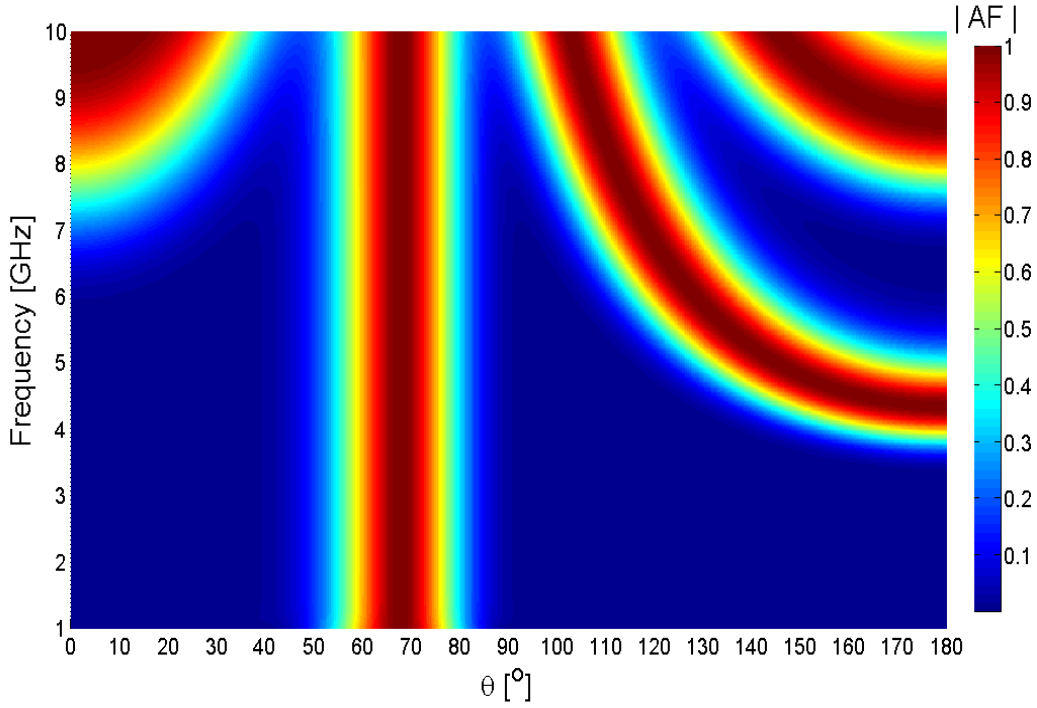

Fig. 4.6: Variations of the array factor (|AF|) versus frequency and angle θ for the array of Fig. 4.1 but with the main beam at $\theta = 67.5^\circ$ (scan angle: $\theta_s = \theta_o - 67.5^\circ = 90^\circ - 67.5^\circ = 22.5^\circ$) and element spacing d=5 cm.

4.2 Compensation of bandwidth reduction due to element antenna

For arrays consisting of identical elements the total radiated field of the array, based on the principle of pattern multiplication, is obtained by multiplying the field of the element and the array factor. The element antenna has its own frequency-dependent radiation characteristics which can significantly impact the overall bandwidth of the array. In this section, it will be shown how the frequency-adaptive element excitation method may be exploited to mitigate the reduction of array overall bandwidth due to the limited bandwidth of its constituent elements.

The total field of an array consisting of identical elements can be expressed as

$$\vec{E}_{tot}\left(\omega_p,\theta\right)=\vec{E}_e\left(\omega_p,\theta\right)\cdot AF_p\left(\omega_p,\theta\right) \tag{4.10}$$

where $\vec{E}_e\left(\omega_p,\theta\right)^{\dagger}$ is the field of an individual element. The radiated electric field of the element in the far-field region can be decomposed into two components written as,

$$\vec{E}_e\left(\omega_p,\theta\right)=\left|E_{e\theta}\left(\omega_p,\theta\right)\right|\angle E_{e\theta}\left(\omega_p,\theta\right)\hat{\theta}+\left|E_{e\phi}\left(\omega_p,\theta\right)\right|\angle E_{e\phi}\left(\omega_p,\theta\right)\hat{\phi} \tag{4.11}$$

The polarization of $\vec{E}_e\left(\omega_p,\theta\right)$ is determined based on the relationships between the magnitudes and phases of the two components in (4.11) and can also be characterized by the axial ratio [92]. In order to compensate for the frequency dependences of both the magnitude and phase (or real and imaginary parts) of each field component in (4.11) a complex vector array factor is needed. For the sake of reducing the complexity of the design in this study, the element antenna is assumed to be linearly polarized or circularly polarized [93]. Here we use linearly polarized element field which can involve one field component only, allowing us to proceed with the rest of the analyses dealing with a scalar element field, denoted as $E_e\left(\omega_p,\theta\right)$, rather than a vector one.

---

† The field of the element antenna, $\vec{E}_e$, is generally a function of both θ and φ, but in the present discussion it is assumed to be a function of θ only. This restriction will be lifted in Chapter 5 when synthesis of planar arrays is studied.

In order to demonstrate how frequency variations of the element field can be compensated so that the narrowing of the array bandwidth is minimized, we introduce a complex function defined as the inverse of the scalar element field,

$$\Omega_{AF}\left(\omega_p,\theta\right)=\left[E_e\left(\omega_p,\theta\right)\right]^{-1} \tag{4.12}$$

Next, let us assume that the desired total field of the array is described by the spatial function $E_{tot}\left(\omega_p,\theta\right)$. The magnitude of this field represents the total pattern of the array which, for distortionless transmission of wideband signals, is required not to vary with frequency over the bandwidth of the signal. The same requirement necessitates that the phase of $E_{tot}\left(\omega_p,\theta\right)$ vary linearly with frequency. The total field can be expressed as

$$E_{tot}\left(\omega_p,\theta\right)=E_e\left(\omega_p,\theta\right)\cdot AF_p\left(\omega_p,\theta\right) \tag{4.13}$$

The element excitation currents can be determined in a way that when the array factor is multiplied by the element field, the desired total field at each frequency sample can be produced. Thus, the array factor needed to compensate for the field of the element antenna should obey the following relationship:

$$AF_p\left(\omega_p,\theta\right)=\Omega_{AF}\left(\omega_p,\theta\right)\cdot G\left(\omega_p,\theta\right) \tag{4.14}$$

This makes the total radiated field to be equal to $E_{tot}\left(\omega_p,\theta\right)=E_e\left(\omega_p,\theta\right)\cdot AF_p\left(\omega_p,\theta\right)=G\left(\omega_p,\theta\right)$, where $|G(\omega_p,\theta)|=f\left(\theta\right)$ is the desired frequency-independent (UWB) radiation pattern of the array and $\angle G\left(\omega_p,\theta\right)=-\alpha_0\omega_p$, ($\alpha_0$ = constant), is the phase of the total field which is expressed such that the desired linear dependence on frequency is maintained. Producing a complex array factor is possible through complex element frequency-adaptive excitation. The complex array factor can be decomposed into two parts, a real part and an imaginary part given by the following expressions.

$$\mathrm{Re}\left\{AF_p\left(\omega_p,\theta\right)\right\}=\mathrm{Re}\left\{I_{0p}\left(\omega_p\right)\right\}+\sum_{n=1}^{N}\mathrm{Re}\left\{I_{-np}(\omega_p)e^{j(n\omega_p d/c)\cos\theta}+I_{np}(\omega_p)e^{-j(n\omega_p d/c)\cos\theta}\right\} \tag{4.15}$$

$$\mathrm{Im}\left\{AF_p\left(\omega_p,\theta\right)\right\} = \mathrm{Im}\left\{I_{0p}\left(\omega_p\right)\right\} + \sum_{n=1}^{N} \mathrm{Im}\left\{I_{-np}(\omega_p)e^{j(n\omega_p d/c)\cos\theta} + I_{np}(\omega_p)e^{-j(n\omega_p d/c)\cos\theta}\right\} \quad (4.16)$$

In the formulation of the array factor presented earlier in this chapter, conjugate currents for symmetrically located elements, $I_{-np}(\omega_p) = I^*_{+np}(\omega_p)$, were assumed. Here, in order to achieve the desired complex array factor, we consider the currents for symmetrically located elements satisfy the relationship $I_{-np}(\omega_p) = I_{np}(\omega_p)$. Using this current relation in (4.15) and (4.16) yields

$$\mathrm{Re}\left\{AF_p\left(\omega_p,\theta\right)\right\} = \mathrm{Re}\left\{I_{0p}\left(\omega_p\right)\right\} + 2\sum_{n=1}^{N} \mathrm{Re}\left\{I_{np}\left(\omega_p\right)\right\}\cos\left[\left(n\omega_p d/c\right)\cos\theta\right] \quad (4.17)$$

$$\mathrm{Im}\left\{AF_p\left(\omega_p,\theta\right)\right\} = \mathrm{Im}\left\{I_{0p}\left(\omega_p\right)\right\} + 2\sum_{n=1}^{N} \mathrm{Im}\left\{I_{np}\left(\omega_p\right)\right\}\cos\left[\left(n\omega_p d/c\right)\cos\theta\right] \quad (4.18)$$

Applying the integral relationships for calculating the Fourier series coefficients to (3.17) and (3.18), we obtain

$$I_{0p}(\omega_p) = \frac{1}{T_p}\int_0^{\pi} AF_p\left(\omega_p,\theta\right)\sin\theta\, d\theta \quad (4.19)$$

$$\mathrm{Re}\left\{I_{np}(\omega_p)\right\} = \frac{1}{T_p}\int_0^{\pi} \mathrm{Re}\left\{AF_p\left(\omega_p,\theta\right)\right\}\cos\left(n\frac{d\omega_p}{c}\cos\theta\right)\sin\theta\, d\theta \quad (4.20)$$

$$\mathrm{Im}\left\{I_{np}(\omega_p)\right\} = \frac{1}{T_p}\int_0^{\pi} \mathrm{Im}\left\{AF_p\left(\omega_p,\theta\right)\right\}\cos\left(n\frac{d\omega_p}{c}\cos\theta\right)\sin\theta\, d\theta \quad (4.21)$$

Combining (4.20) and (4.21) yields

$$\begin{aligned} I_{np}(\omega_p) &= \mathrm{Re}\left\{I_{np}(\omega_p)\right\} + j\,\mathrm{Im}\left\{I_{np}(\omega_p)\right\} \\ &= \frac{1}{T_p}\int_0^{\pi} AF_p\left(\omega_p,\theta\right)\cos\left[(nd\omega_p/c)\cos\theta\right]\sin\theta\, d\theta \\ &= \frac{1}{T_p}\int_0^{\pi}\left[G(\omega_p,\theta)/E_e(\omega_p,\theta)\right]\cos\left[(nd\omega_p/c)\cos\theta\right]\sin\theta\, d\theta \end{aligned} \quad (4.22)$$

To achieve scanning, $I_{np}(\omega_p)$ in (4.22) should be replaced with $I_{np}(\omega_p)\exp(-\Psi_{ns})$, where $\Psi_{ns} = \Psi^*_{-ns} = j(nd\omega_p / c)(\cos\theta_s - \cos\theta_0)$ is an embedded element phasing term as it was applied and explained in (4.9). The expressions in (4.19) to (4.22) provide exact results only if N were infinity, corresponding to an array with infinite number of elements. Clearly, for finite values of N truncation errors occur; however, these errors can be reduced to some degree by modifying the excitation currents such that the error along the direction of maximum radiation ($\theta = \theta_0$) vanishes and errors along other directions ($\theta \neq \theta_0$) are somewhat reduced. Accordingly, the modified excitation currents are expressed as:

$$I_{0p\_\mathrm{mod}} = \frac{I_{0p}(\omega_p)}{\left|E_{tot}\left(\omega_p, \theta_o\right)\right|} \tag{4.23}$$

$$I_{np\_\mathrm{mod}} = \frac{I_{np}(\omega_p)}{\left|E_{tot}\left(\omega_p, \theta_o\right)\right|}, \quad n = \pm 1, \pm 2, \quad \pm \mathrm{N} \tag{4.24}$$

4.3 Compensation of mutual coupling and element input impedance

As it was discussed in Chapter 2, inter-element mutual coupling is a significant factor that cannot be overlooked because it may result in degrading impacts on the array radiation characteristics, especially in the case of arrays with tight element spacing. In this section, the mitigation of element mutual coupling using the proposed frequency-adaptive element excitation is discussed.

4.3.1 Mechanisms contributing to inter-element mutual coupling

In an antenna array system, mutual coupling is caused by the following interactions [39].

- Direct space coupling among array element antennas
- Indirect coupling caused by near-by scatterers
- Coupling through feed network

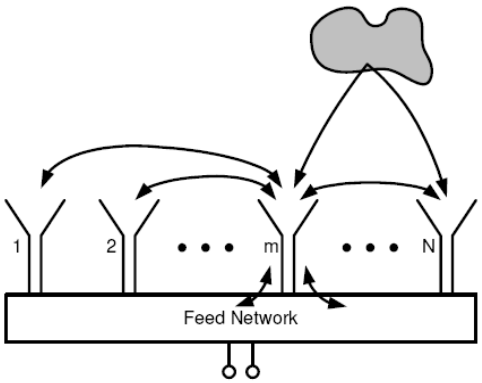

Fig. 4.7: Mechanisms of inter-element mutual coupling in a linear array [39]

Figure 4.7 illustrates these mechanisms. In general, mutual coupling deteriorates the performance of the array, especially when main-beam scanning over a wideband is the expected performance. In this study, compensation of mutual coupling is investigated with the aim of minimizing distortions on wideband and UWB signals.

4.3.2 Array modeling with inter-element mutual coupling

As a first step in understanding how the element antennas of the array interact with each other, we shall start with an ideal case of isolated elements. The current distribution for an isolated element antenna is given by the following equation.

$$\vec{J}_n\left(\vec{r'}\right) = I_n \vec{j}_n^{\,i}\left(\vec{r'}\right) \tag{4.25}$$

where $\{I_n\}$ are complex valued terminal currents and $\vec{j}_n^{\,i}\left(\vec{r'}\right)$ is the normalized current distribution of an isolated element antenna, as shown in the example of Fig. 4.8, $\vec{r'}$ is the position vector used to describe spatial variations of the current distribution.

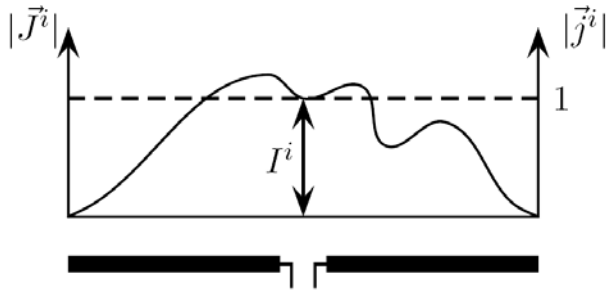

Fig. 4.8: Current distribution and terminal current of an isolated element antenna [39]

The radiation pattern in the far-field zone of an ideal array that consists of isolated element antennas, as those of Fig. 4.8, is given as follows,

$$\vec{F}^i(\theta,\phi) = \vec{g}_n^i(\theta,\phi)\sum_{n=1}^{N} I_n^i e^{j\beta_o \hat{r}\cdot\vec{r}_n} = \vec{g}_n^i(\theta,\phi)\cdot AF^i(\theta,\phi) \tag{4.26}$$

where $\{\vec{r}_n\}$ are vectors from a fixed origin to the center of the excitation terminals of the elements, $\vec{g}_n^i(\theta,\phi)$ is the radiation pattern of the *n*th element, and $AF^i(\theta,\phi)$ is the ideal array factor. The superscript '*i*' in (4.26) emphasizes the fact that the elements are assumed to be isolated.

In order to model the array system more accurately, a new element radiation pattern must be defined that accounts for the induced currents due to coupling to surrounding elements. This modified radiation pattern is called the active-element radiation pattern. The following equation represents the definition of a unit-input voltage active element pattern [37, 38].

$$\vec{g}_n^{a\,u}(\theta,\phi) = \frac{1}{j\omega\varepsilon}\hat{r}\times\hat{r}\times\iiint_{v'}\overrightarrow{j_n^a}(\vec{r}')e^{-j\beta_o\hat{r}\cdot\vec{r}'}dv'\Big|_{V_{gn}=1,V_{gj}=0 \text{ for all } j \text{ except } n} \tag{4.27}$$

where V_{gn} is the source voltage, $\overrightarrow{j_n^a}$ is the current that exists on all elements in the array when the *n*th element is excited with a unit voltage and all of the other elements are terminated with their respective source impedances as shown in Fig. 4.9. The radiation pattern of the array shown in Fig. 4.9 can be computed using the following equation.

$$\vec{F}_n(\theta,\phi) = \sum_{q=1}^{N}\vec{g}_q^{a\,u}(\theta,\phi)\cdot V_{gq}^s \tag{4.28}$$

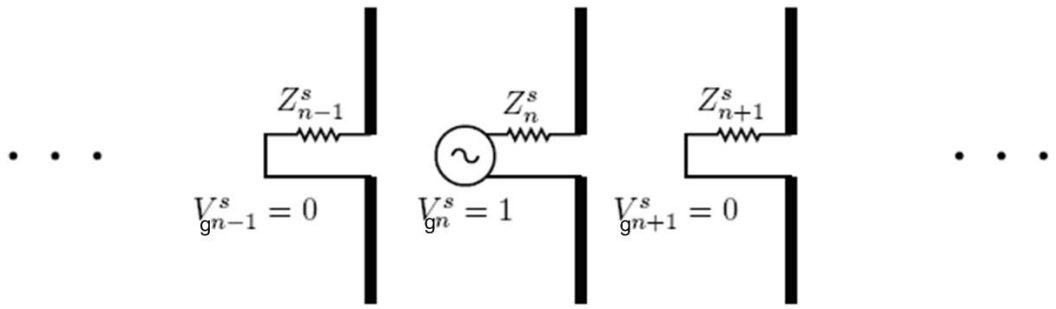

Fig. 4.9: Definition of active-element pattern for *n*th element [39]

In order to simplify the measurement process of $\vec{g}^{\,a\,u}_{gq}(\theta,\phi)$, we assume that the position of the origin of the array system is fixed but the phase reference changes as q changes. Accordingly, it is useful to define a new vector quantity for the unit-input active-element pattern that accounts for these phase variations based on the location of the active element inside the array, that is the phase-adjusted unit-input active-element pattern [37, 38]:

$$\vec{g}^{\,a\,p}_{n}(\theta,\phi) = \vec{g}^{\,a\,u}_{n}(\theta,\phi)\, e^{j\beta_o \hat{r}\cdot\vec{r}'_n} \tag{4.29}$$

It should be mentioned that the phase term in (4.29) was implicitly included in (4.28). By substituting (4.29) into (4.28), we obtain the following expression for the radiation pattern of the array.

$$\vec{F}(\theta,\phi) = \sum_{q=1}^{N} \vec{g}^{\,a\,p}_{q}(\theta,\phi)\, e^{-j\beta_o \hat{r}\cdot\vec{r}'_q} V^s_{gq} \tag{4.30}$$

In large arrays, calculating or measuring $\vec{g}^{\,a\,p}_{q}(\theta,\phi)$ for each element in the array is a time consuming and most likely an expensive process. It has been shown in [37, 38] that using the pattern of the center element as an average pattern for the interior elements of the array can represent the total pattern of the array with reasonable accuracy. This method is called 'hybrid method' because it is a mix of using an average pattern for the interior elements and exact patterns for the edge elements of the array. One restriction arises as a result of using an average pattern, namely that the interior elements have to be equally spaced for the assumption of similar surroundings for all the interior elements to be valid. One more reason that having equally spaced interior elements is useful is to be able to apply Fourier series expansion as it was

discussed in this chapter. Equation (4.31) shows how the hybrid method can be applied to an array configuration with equally spaced interior elements.

$$\vec{F}(\theta,\phi) = \underbrace{\bar{g}_i^{av}(\theta,\phi)\cdot\sum_{n=1}^{N_i} e^{-j\beta_o \hat{r}\cdot\vec{r_n'}}\cdot V_{gn}^s}_{\text{interior elements}} + \underbrace{\sum_{m=1}^{N_e} \bar{g}_m^{p}(\theta,\phi) e^{-j\beta_o \hat{r}\cdot\vec{r_m'}}\cdot V_{gm}^s}_{\text{edge elements}} \qquad (4.31)$$

where N_i is the number of the interior elements, N_e is the number of edge elements, and $N = N_i + N_e$ is the total number of elements in the array. In [37, 38], the hybrid method was tested by analyzing an array with seven dipole element antennas equally spaced by 0.4λ. The hybrid method was shown to be reasonably accurate when compared to the exact method based on using (4.30).

In (4.13), it was assumed that the radiated fields by individual elements of the array are identical regardless of their location in the array and their active-element patterns. The significance of the error that results from assuming an isolated element field in (4.13) depends on the geometry of the array and the geometry of the element antenna. This active-element error can be compensated by modifying the array factor as follows.

$$\overline{AF}(\omega_p,\theta) = \underbrace{\left[\left|E_e^i(\omega_p,\theta)\right|\right]^{-1}\cdot G_p(\theta)}_{AF(\omega_p,\theta)\text{ of eq. (4.13)}}\cdot G_p^a(\theta) \qquad (4.32)$$

where

$G_p^a(\omega_p,\theta) = G_p(\theta)\cdot\left[E_{tot}^a(\omega_p,\theta)\right]^{-1}$,

$G_p(\theta)$ is the desired complex function of the radiated total field by the array,

$E_e^i(\omega_p,\theta)$ is the field of the isolated element which is used in (4.13),

$E_{tot}^a(\omega_p,\theta)$ is the total field including the error produced by the fields of the active-elements

This step of compensating for active-element error requires knowledge of $E_{tot}^a(\omega_p,\theta)$, which can be computationally expensive to determine, that is why it is preferred to start with the assumption of isolated elements and observe whether the error due to the fields of the active-elements is significant or not. It should be noted that the modification in (4.32) will result in new

excitation coefficients, which can be calculated by using (4.22) and replacing $AF_p\left(\omega_p,\theta\right)$ with $\overline{AF}\left(\omega_p,\theta\right)$. The compensation of error due to an active-element can be integrated into the proposed method of array synthesis through an iterative process, as it will be shown later in this chapter.

4.3.3 **Array network model**

In sub-section 4.3.2, it was shown how the total radiation pattern of the array differs from the ideal case of isolated elements because of the induced currents that result from inter-element interactions. If the array is viewed as a network, the scattering parameters can be used to measure the interactions between the elements of the array at the terminals or the port of each element. S-parameters are well known for their convenience in the measurement process at radio frequencies. Figure 4.10 shows the array represented as an N-port network with V_n^{A+} and V_n^{A-} being the incident and reflected voltage waves, respectively, at the port of element n. For convenience, another form of wave amplitudes is defined as summarized below.

$$a_n = V_n^{A+} \Big/ \sqrt{Z_{on}} \tag{4.33}$$

$$b_n = V_n^{A-} \Big/ \sqrt{Z_{on}} \tag{4.34}$$

$$\left[V_n^{A-}\right] = [S]\left[V_n^{A+}\right] \tag{4.35}$$

$$[b] = [S][a] \tag{4.36}$$

where

$$S_{ij} = \left.\frac{V_i^{A-}\sqrt{Z_{oj}}}{V_j^{A+}\sqrt{Z_{oi}}}\right|_{V_k^+=0 \text{ for all } k\neq j} = \left.\frac{b_i}{a_j}\right|_{a_k=0 \text{ for all } k\neq j} \tag{4.37}$$

V_j^{A+} denotes excitation voltage at the port of the active element when measuring S_{ij}.

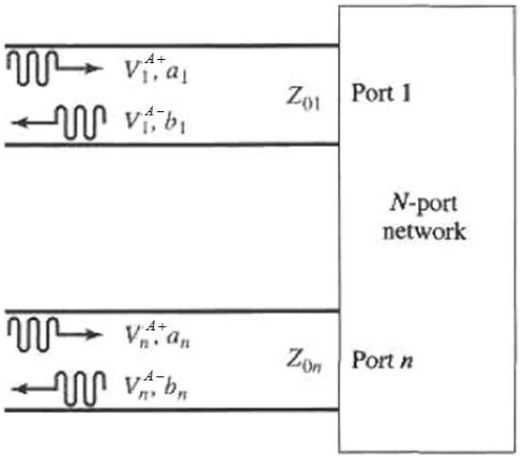

Fig. 4.10: Representation of array as an N-port network with different characteristic impedances

The total voltage and current at port n are calculated as follows.

$$V_n^A = V_n^{A+} + V_n^{A-} = \sqrt{Z_{on}}\left(a_n + b_n\right) \tag{4.38a}$$

$$I_n = \frac{1}{Z_{on}}\left(V_n^{A+} - V_n^{A-}\right) = \frac{1}{\sqrt{Z_{on}}}\left(a_n - b_n\right) \tag{4.38b}$$

which can be used to calculate the impedance at a specific port in the following equation.

$$Z_n^A = \frac{V_n^A}{I_n} \tag{4.39}$$

The reflected voltage at port n can be decomposed as follows.

$$\begin{aligned} V_n^{A-} &= S_{n1}V_1^{A+} + S_{n2}V_2^{A+} + \ldots + S_{nN}V_N^{A+} \\ &= \left.\frac{V_n^{A-}}{V_1^{A+}}\right|_{V_k^{aA+}=0 \text{ for all } k\neq 1} \cdot V_1^{A+} + \ldots + \left.\frac{V_n^{A-}}{V_N^{A+}}\right|_{V_k^{aA+}=0 \text{ for all } k\neq N} \cdot V_N^{A+} \end{aligned} \tag{4.40}$$

According to (4.37), if the element antenna is considered to be a linear time invariant (LTI) system, S-parameters do not change with scan angle, mainly because of S_{ij} being unique to only one active element. However, (4.40) shows that V_n^{A-} varies with scan angle since each V_n^{A+} is phased differently in order to achieve main-beam scanning. This variation of V_n^{A-} with scan

angle makes the input impedance at port n in (4.39) also a function of the scan angle. This variation of Z_n^A with scan angle makes it necessary to adaptively compensate for mutual coupling in order to achieve wideband signal acquisition with minimal distortions. This variation of element antenna input impedance with scan angle according to inter-element mutual coupling makes the use of S-parameters the best way to describe the system representation of the array.

4.3.4 **Mutual coupling compensation**

The challenge associated with mutual coupling compensation is to deliver the desired excitation currents to the terminals of the element antenna. Here, the implemented compensation accounts for the collective effects of mutual coupling and element input impedance. Equation (4.38b) can be normalized in the following way.

$$I_{np} = \left(A_{np} - B_{np} \right) \tag{4.41}$$

where $A_{np} = a_{np} / \sqrt{Z_{on}}$ and $B_{np} = b_{np} / \sqrt{Z_{on}}$. Smith [36] has shown how the reflected power wave, B_n, can be calculated based on the desired currents, as given by the following equation.

$$\left[B_{np} \right] = \left[I - S_p \right]^{-1} \left[S_p \right] \left[I_{np} \right] \tag{4.42}$$

where I is the identity matrix, $\left[I_{np} \right]$ are the desired currents, and $\left[S_p \right]$ is the S-parameter matrix that represents the array, all at a frequency ω_p. From the definitions of a_{np} and b_{np} given in (4.33) and (4.34), we can calculate the normalized incident power waves as follows [36].

$$\left[A_{np} \right] = \left[I_{np} \right] + \left[B_{np} \right] \tag{4.43}$$

Then, the required voltages are obtained as

$$V_{np}^{A+} = Z_{on} \left(\left[I \right] + \left[I - S_p \right]^{-1} \left[S_p \right] \right) \left[I_{np} \right] = Z_{on} \left[W_p \right] \left[I_{np} \right] \tag{4.44}$$

where $\left[W \right] = \left(\left[I \right] + \left[I - S \right]^{-1} \left[S \right] \right)$

If the excitation voltages in (4.40) were to be applied to the elements of the array, the input impedance of the element antenna would be affected as a consequence of inter-element mutual

coupling. However, power reflections at the terminals of the element antenna remain unaffected because the scattering properties do not vary with element excitation voltages. This is why S-parameters are most convenient for analyzing phased array problems. In this dissertation, S-parameters are calculated using a commercial full-wave simulation software package (FEKO suite 6.3) [94].

4.4 Flow chart of the synthesis technique

The implementation of the proposed technique for ultra-wideband array synthesis is summarized in this section. Figure 4.11 shows the flow chart that describes the steps for implementing the proposed synthesis techniques. In the first step, the basic design parameters required for the design of the array are specified. These parameters include bandwidth, element spacing, and scanning range. Step 2 consists of compensating for the effects of the field of the element antenna and calculating the excitation coefficients necessary to produce a desirable total field. In step 3, the excitation voltages necessary to compensate for inter-element mutual coupling are calculated. An error is produced as a result of the assumption of isolated elements rather than active-elements. If the error due to active-element field is intolerable, the design process proceeds to step 4, otherwise the design process reaches its end state. In step 4, a modified array factor is calculated in order to compensate for the error produced by the assumption of isolated elements. The design process then flows from step 4 back to the last part of step 2. The flow of the design technique presented in Fig. 4.11, may suggest an iterative process to compensate for the isolated element error; a loop starts from step 4 and goes through the last part of step 2, through step 3, and back to step 4.

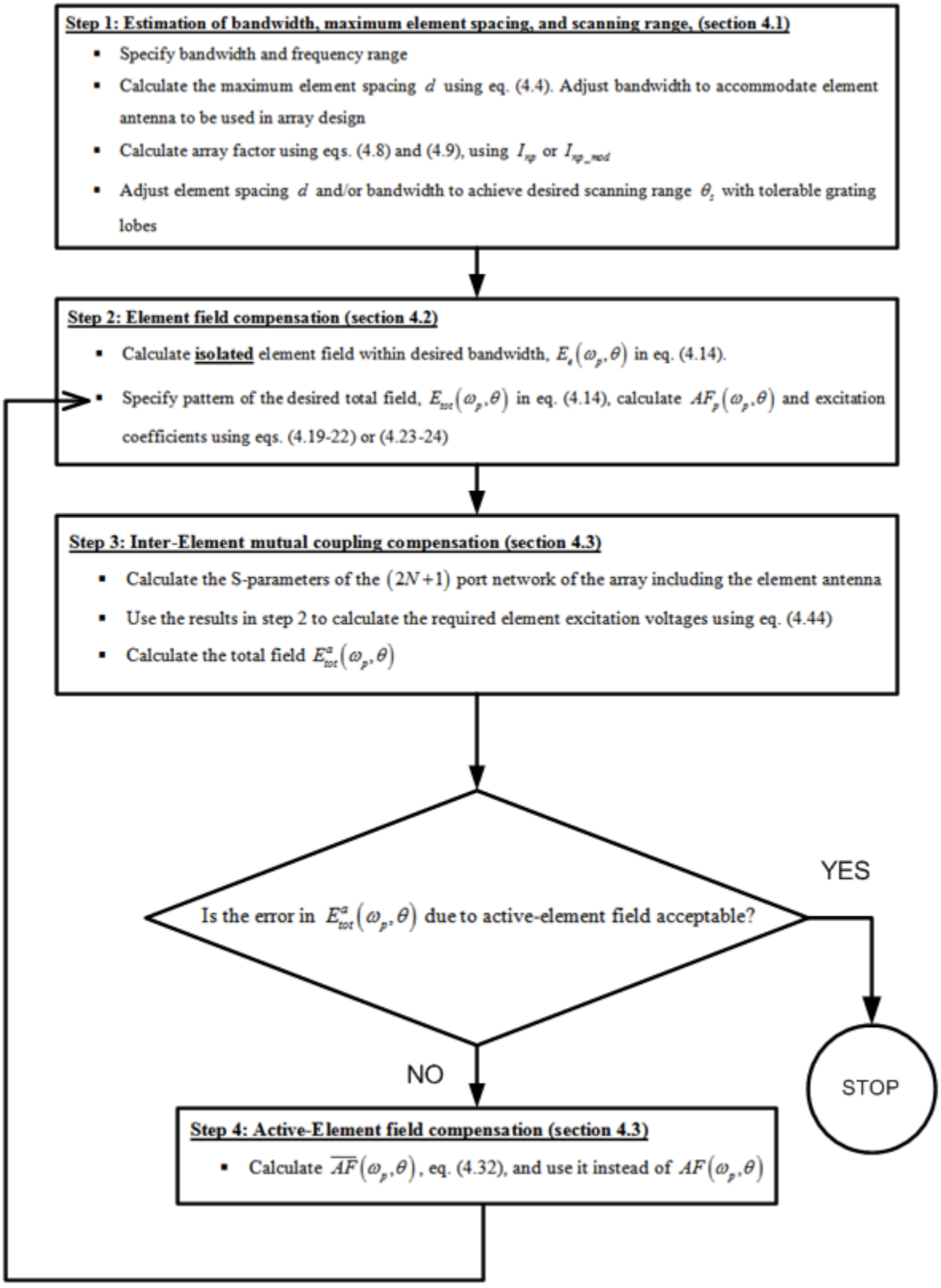

Fig. 4.11.: Flow chart illustrating the implementation of the proposed array synthesis technique

Chapter 5: Design Implementation and Simulation Results

In this chapter, the array synthesis method presented in the previous chapter is implemented in a step by step manner to design wideband and ultra wideband linear arrays. Two types of dipole antennas are chosen as array elements in design examples studied here. The bandwidth performance of these arrays is assessed and the validity of the proposed technique is examined through simulation results.

5.1 Linear array of wire dipoles

Figure 5.1 illustrates the geometry of a linear array consisting of 17 equally spaced wire dipole antennas. The method of array synthesis discussed in Chapter 3 is used to calculate the frequency-adaptive element excitations necessary to produce a frequency-invariant total field radiated by the array. First, for the sake of comparison, we start with an uncompensated array design. In the uncompensated case, the element excitations are calculated without taking into consideration the effects of the field of the element antenna and inter-element mutual coupling. That is, instead of using (4.14) for the array factor and (4.44) for the excitation voltages of the elements, the following equations are used.

$$AF_p\left(\omega_p,\theta\right)=G\left(\omega_p,\theta\right) \tag{5.1}$$

$$V_{n\,p}^{A+}\left(\omega\right)=Z_{on}\left[I_{n\,p}\left(\omega_p\right)\right] \quad \text{; element excitation} \tag{5.2}$$

where $G\left(\omega_p,\theta\right)$ is the desired pattern function of the total field, and $\Omega_{AF}\left(\omega_p,\theta\right)=1$. For the example studied here, the pattern function is chosen to be $f(\theta)=G\left(\omega_p,\theta\right)=\sin^{50}\left(\theta\right)$. The bandwidth of the array is chosen to be the frequency range over which $S_{11}\le -3$ dB for the isolated element antenna is satisfied (that is, the input impedance bandwidth of the isolated element). For the example case of the element antenna used in the array of Fig. 5.1, the bandwidth covers the frequency range 4.5 GHz to 7.0 GHz. It is emphasized that the proposed array synthesis method does not compensate for the impedance mismatch between the excitation port and the element antenna, and impedance matching is considered as part of the design of the element antenna. The far-field magnitude pattern of the array in Fig. 5.1, with its element

excitations calculated using (5.1) and (5.2), is shown in Fig. 5.2. Examination of this figure indicates that the total field produced by the array deviates from the desired frequency-invariant performance, with more than 4 dB variation in the direction of maximum radiation.

Next, for the same array configuration shown in Fig. 5.1 and the same desired radiation pattern $G\left(\omega_p, \theta\right) = \sin^{50}\left(\theta\right)$, a compensated array synthesis is undertaken. Equation (4.14) is used to calculate the array factor with the field of the element antenna taken into consideration and (4.44) is used to calculate the required element excitations to achieve the frequency-invariant total field while compensating for inter-element mutual coupling. As noted in Fig. 5.3, the magnitude pattern of the total field is essentially invariant within the bandwidth of interest; variations are less than 0.3 dB in all directions. Comparison of Figs. 5.2 and 5.3 clearly indicates a significant improvement toward achieving a frequency-invariant performance. A three-dimensional view of the total radiation pattern for the compensated design of Fig. 5.3 is provided in Fig. 5.4. It is recalled that the array factor used in the compensated design is complex, which means that the phase of the field of the element antenna and the inter-element mutual coupling are compensated as complex quantities. The best method to compare the linearity of the phase of the radiated total fields of the uncompensated and the compensated designs is to compare their group delays. The group delay is defined as the derivative of the phase of the total-field with respect to radian frequency ω. For the desired performance of minimized signal distortions, a linearly varying phase or a constant group delay versus frequency is required. Figure 5.5 compares the group delays of uncompensated and compensated designs of Figs. 5.2 and 5.3. It is observed that the group delay of the compensated design is almost constant and exhibits significantly less variations compared with the group delay of the uncompensated design [95]. In order to appreciate this improvement in group delay, the transient response of the uncompensated and the compensated array designs are calculated and compared later in this chapter. A summary of performance parameters for the compensated design described in Fig. 5.3, including half-power beamwidth (HP), directivity (D), and maximum side-lobe level (SLL), is presented in Table 5.1.

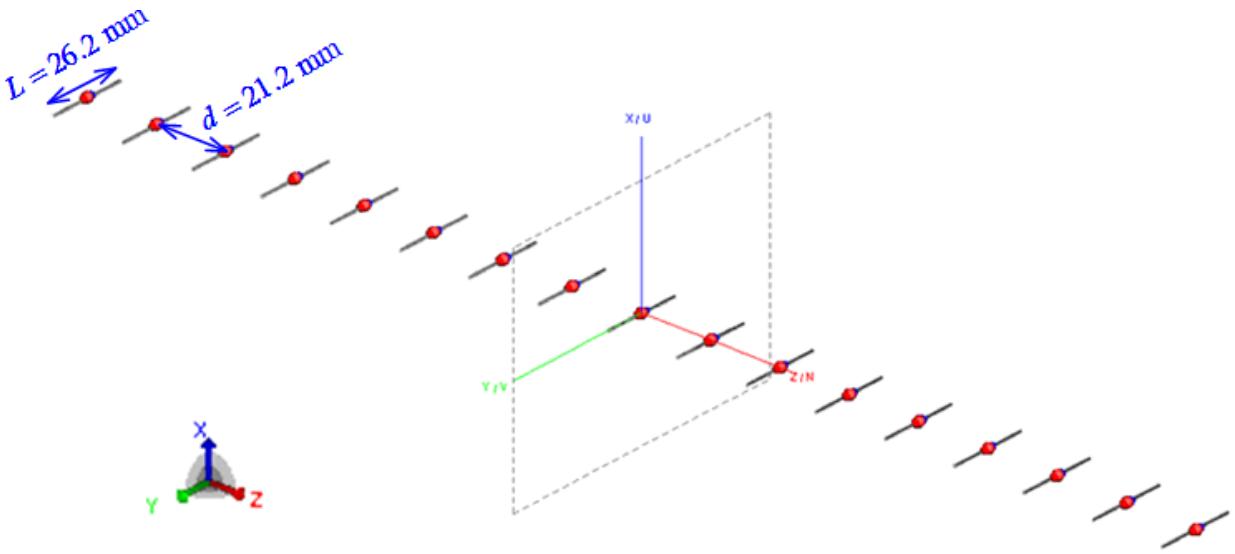

Fig. 5.1: Linear array of 17 equally spaced wire dipoles; wire radius $a = 0.5$ mm, element spacing $d = 0.4\lambda_r$, resonant frequency $f_r = 5.5$ GHz, length of dipole $L = 0.48\lambda_r$

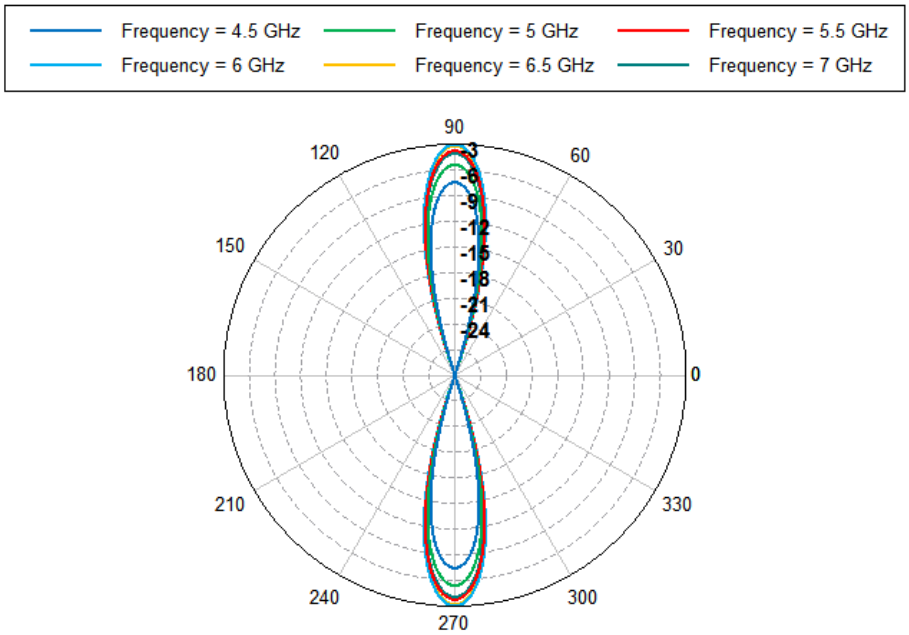

Fig. 5.2: xz-plane cuts of the total patterns at different frequencies for the uncompensated design (frequency variations of the element field and inter-element mutual coupling are not accounted for) of an array with geometry and parameters the same as those given in Fig. 5.1. The desired total array pattern is described by $f(\theta) = \sin^{50}\theta$ over the frequency range 4.5GHz to 7GHz.

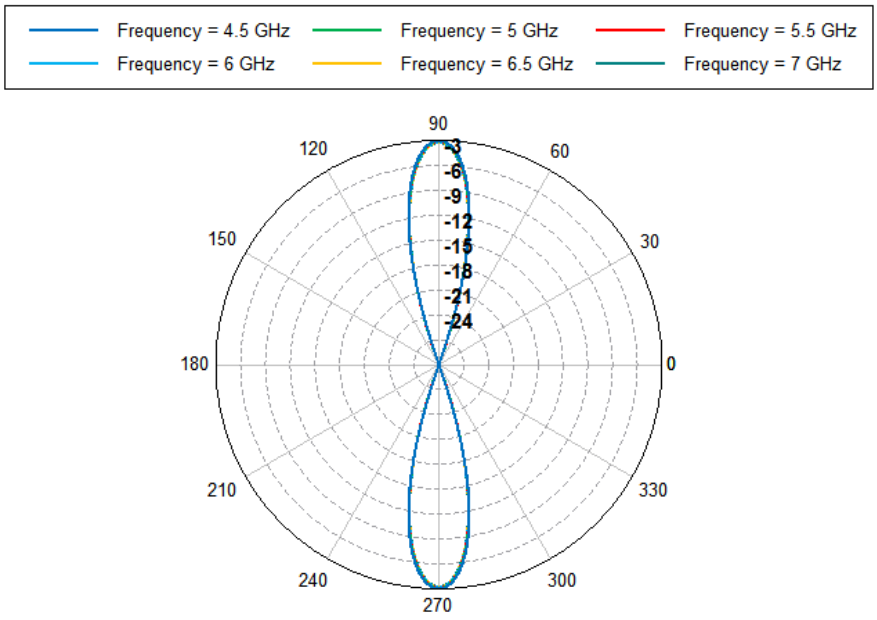

Fig. 5.3: xz -plane cuts of the total patterns at different frequencies for the compensated design (frequency variations of the element field and inter-element mutual coupling are accounted for) of an array with geometry and parameters the same as those given in Fig. 5.1. The desired total array pattern is described by $f(\theta) = \sin^{50}\theta$ over the frequency range 4.5GHz to 7GHz. All patterns are approximately coincident.

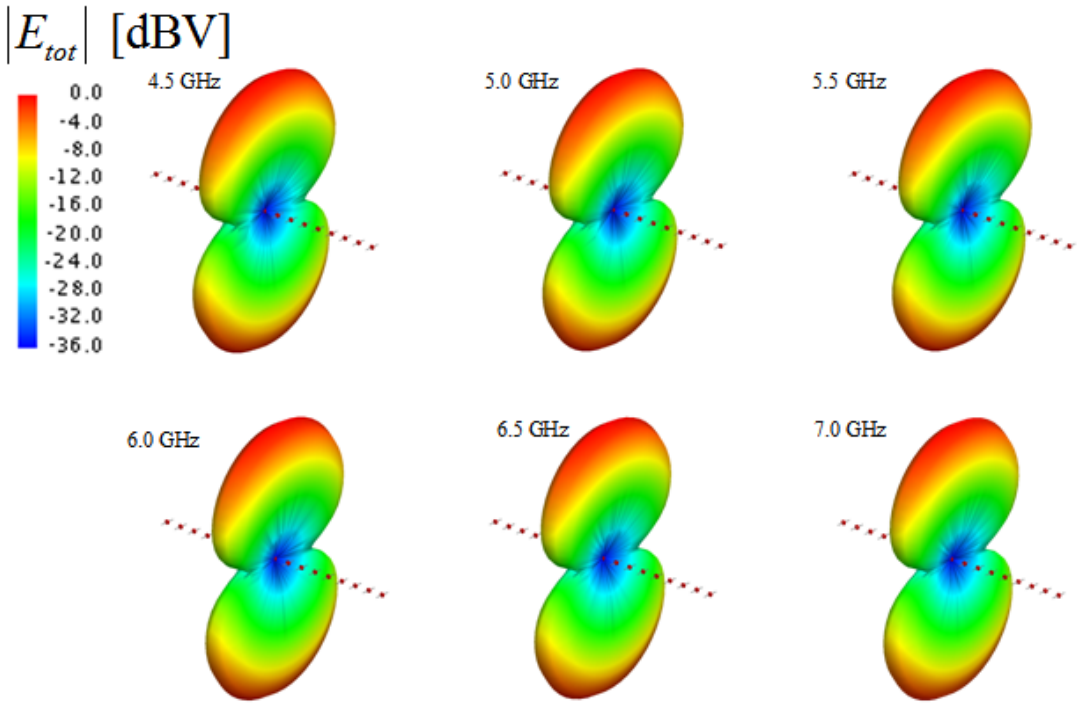

Fig. 5.4: Three-dimensional views of the magnitude patterns at different frequencies for the compensated array design described in Fig 5.3

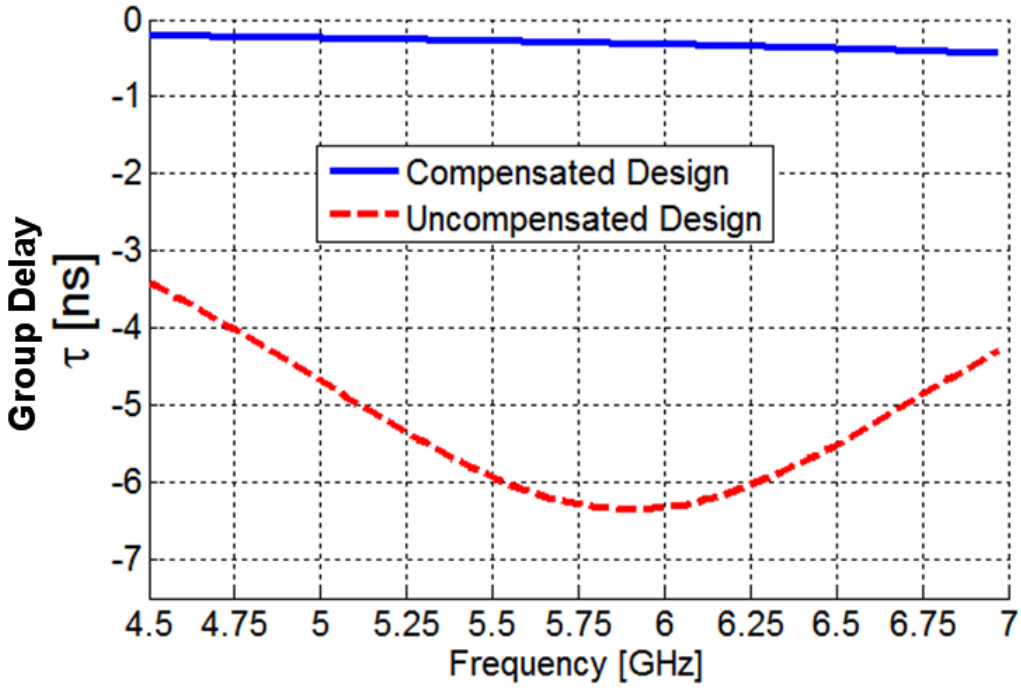

Fig. 5.5: Comparison of group delays for uncompensated and compensated array designs along the direction of maximum radiation, $\theta = 90^{\circ}$. For both designs the array geometry and parameters are the same as those given in Fig. 5.1, and the desired total pattern is described by $f(\theta) = \sin^{50}\theta$ over the frequency range 4.5GHz to 7GHz.

Table 5.1: Summary of performance parameters including, half-power beamwidth (HP), directivity (D), and maximum sidelobe level (SLL) for the array of wire dipoles described in Fig. 5.3

Frequency (GHz)	**Performance Parameters**		
	HP	D	SLL
4.5	13.9º	12.2 dB	-42.7 dB
5.0	13.7º	12.3 dB	-49.8 dB
5.5	13.5º	12.4 dB	-58.1 dB
6.0	13.5º	12.5 dB	< -58.1 dB
6.5	13.5º	12.6 dB	< -58.1 dB
7.0	13.5º	12.7 dB	< -58.1 dB

In order to achieve main-beam scanning of the total-field of the array described in Fig. 5.3, a linear phase-shift is applied to the element excitations as was implemented in (4.22). Calculating the element excitations using (4.22) will allow for main-beam scanning while preserving the frequency-invariant performance already achieved for the compensated array design described in Fig. 5.3. Figure 5.6 illustrates the scanned total pattern at a scan angle $\theta_s = \theta_o - 22.5^\circ = 67.5^\circ$ (θ_o = direction of maximum radiation=90°, when all the elements are in phase), indicating that a 45° scanning range around the broadside direction θ_o can be provided. The same linear phase performance that was achieved in the array design of Fig. 5.3 is maintained when the main beam is scanned in Fig. 5.6. A summary of performance parameters for the array described in Fig. 5.6 is presented in Table B1 in Appendix B.

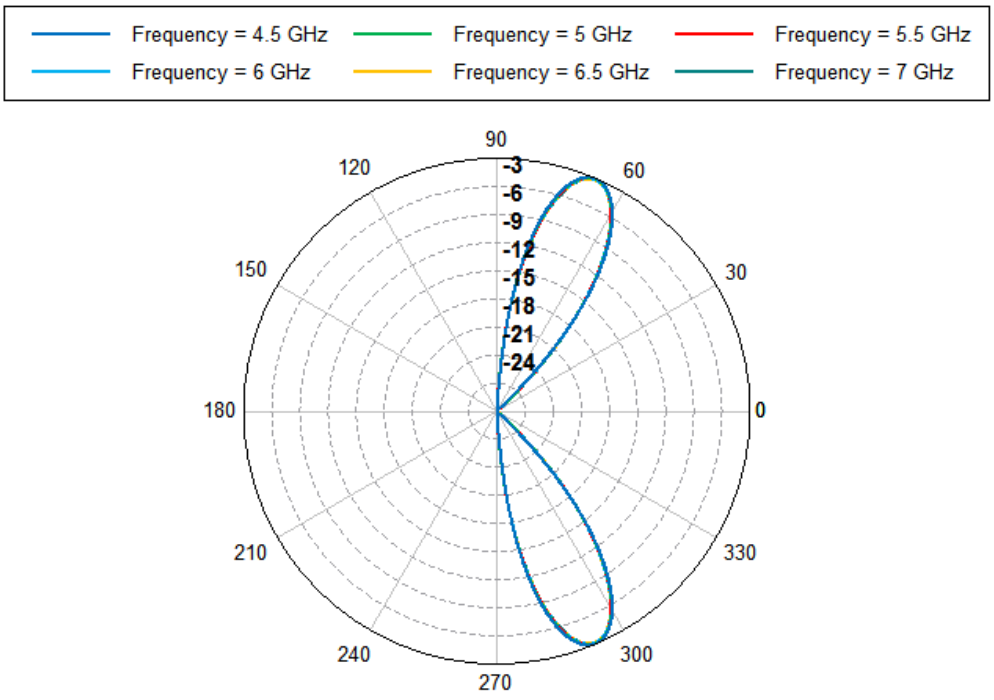

Fig. 5.6: Total pattern in the xz-plane for the compensated array design described in Fig. 5.3 but scanned to $\theta_s = \theta_o - 22.5^\circ = 67.5^\circ$. All patterns are approximately coincident.

5.2 Elliptical dipoles as element antenna

The element antenna suitable for ultra-wideband array designs proposed in this research should provide an acceptable impedance matching performance and far-field radiation pattern over the bandwidth of design. The field pattern of the element antenna can be compensated through the array factor as discussed in section 4.2. The element size is also an important design parameter with direct impact on allowable array element spacing. To provide a wide main-beam scanning range without the appearance of grating lobes within the design bandwidth, the element spacing needs be minimized. Some of the well known UWB antennas that can provide all of these requirements are circular- and the elliptical-disc dipoles [96-98].

The geometry of a UWB circular-disc dipole antenna [96, 97] is shown in Fig. 5.7. The radius of both circles is 30 mm and the length of the feed wire is 2 mm. Figure 5.8 illustrates variations of the VSWR (voltage standing-wave ratio) and the input impedance of this dipole antenna versus frequency. As noted from Fig. 5.8a, the size of the antenna can be scaled down by a multiplicative factor of 2GHz/3GHz and the antenna would still be adequately impedance matched in the UWB frequency range of 3.1 GHz to 10.6 GHz. It can be also seen in Fig. 5.8b that at lower frequencies, the input reactance of the antenna is highly capacitive. In the study presented in [96], the effect of elongating the circles in Fig. 5.7 in the direction perpendicular to the feed line (thus creating an elliptical structure with the major axis perpendicular to the feed wire line) was investigated. The result was a wider bandwidth, but at the cost of increased size and higher VSWR at lower frequencies.

As it was mentioned in the beginning of this section, keeping the size of the element antenna small is often one of the important design requirements. If the antenna with characteristics shown in Fig. 5.8 is modified in a way that provides better impedance matching at the lower frequencies, the size of the antenna can be scaled down even further to shift its bandwidth to the UWB frequency range. Comparison of the input impedances for circular and elliptical dipoles in Figs. 5.8b and 5.10b leads one to believe that attaching a narrower tapered structure to the feed wire instead of a circular one would provide a better impedance matching performance at the lower frequencies. This is due to the fact that the input impedance of narrower tapered structure is less capacitive as seen in Fig. 5.10b.

A modified design for the elliptically-tapered dipole antenna, as shown in Fig. 5.9, is proposed here which is expected to further improve the impedance matching performance at lower frequencies. A single arm of this elliptically-tapered dipole antenna consists of two half ellipse parts with a common center and their major axes perpendicular to each other, as seen in Fig. 5.9. A full-wave analysis of this antenna indeed ascertained the better impedance matching performance at lower frequencies, but of course at the cost of slightly larger size along the feed line compared to the circular dipole. If the elliptically-tapered dipole is scaled to the UWB frequency range, it will yield the same length as that of a scaled circular dipole in the UWB range. The multiplicative scaling factor of the elliptically-tapered antenna required to shift its bandwidth to the UWB frequency range is 1.5GHz/3GHz (results in axial dimensions 15 mm $\times$ 20 mm for each arm of the dipole), while for the circular dipole this factor is 2GHz/3GHz (results in 20 mm diameter for each circular arm). In the direction perpendicular to the feed wire line, the elliptically-tapered dipole is smaller in size than the circular dipole. This advantage of the elliptically-tapered dipole over the circular one allows for smaller element spacing which, in turn, results in a wider scanning range over the required bandwidth. The VSWR and input impedance characteristics of the scaled version of the elliptically-tapered dipole are shown in Fig. 5.11.

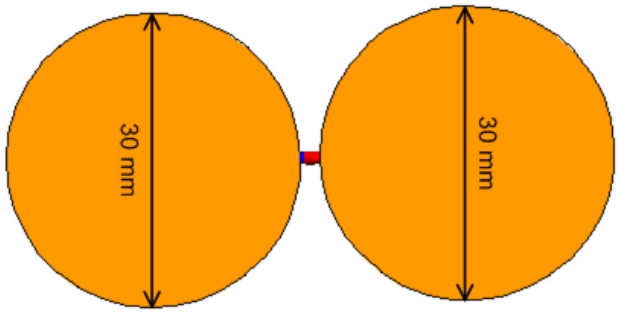

Fig. 5.7: Circular-disc dipole antenna as an ultra-wideband element for frequency-invariant arrays

Figure 5.12 illustrates the distribution of the surface current density for the scaled elliptically-tapered disc dipole antenna with characteristics shown in Fig. 5.11. As observed in Fig. 5.12, on each arm the current decays smoothly from the excitation port all the way to the edge of the disc. In fact, it is this kind of behavior that provides the UWB performance exhibited by the VSWR characteristic shown in Fig. 5.11a.

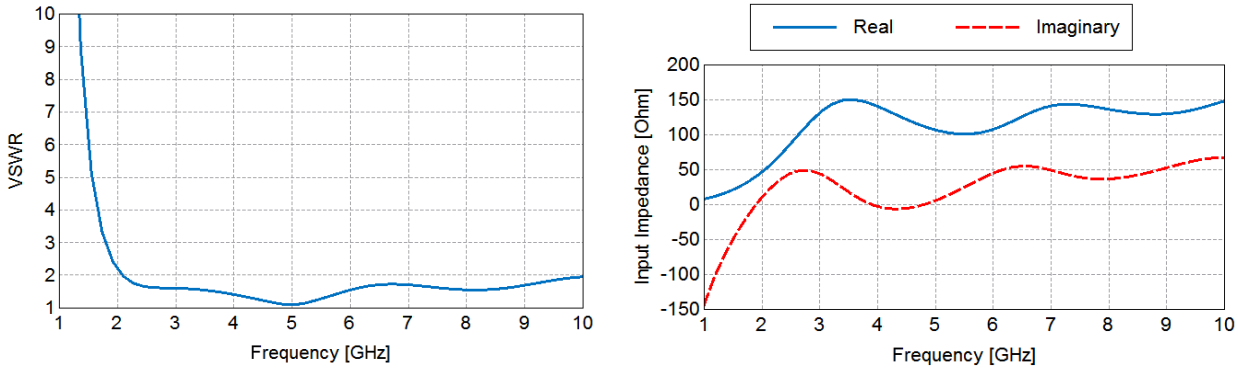

(a) VSWR (b) Input Impedance

Fig. 5.8: Variations of (a) VSWR referenced to 100Ω and (b) input impedance versus frequency for the circular-disc dipole antenna shown in Fig. 5.7

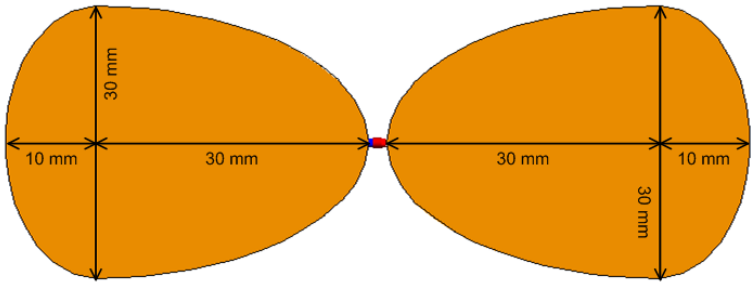

Fig. 5.9: Elliptically-tapered disc dipole antenna as an ultra-wideband element with improved input-impedance matching performance compared with the circular-disc dipole shown in Fig. 5.7.

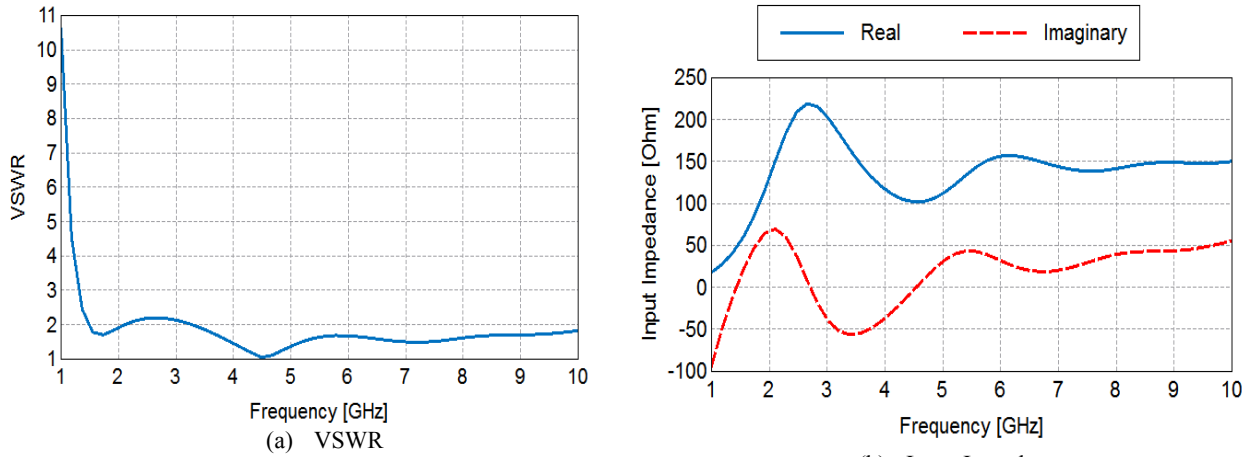

(a) VSWR (b) Input Impedance

Fig. 5.10: Variations of (a) VSWR referenced to 100Ω and (b) input impedance versus frequency for the elliptically-tapered disc dipole antenna shown in Fig. 5.9.

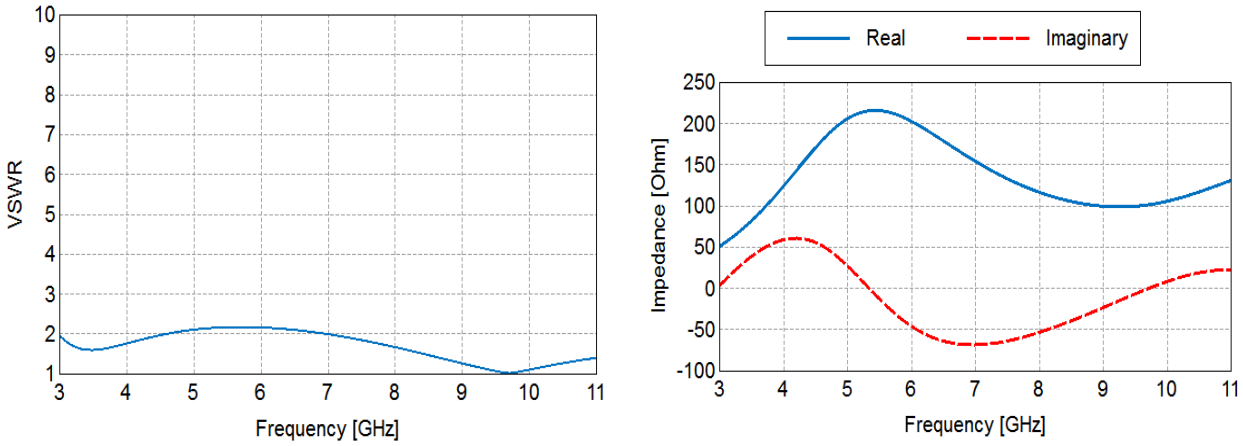

(a) VSWR (b) Input Impedance

Fig. 5.11: Variations of (a) VSWR referenced to 100Ω and (b) input impedance versus frequency for the scaled version of the elliptically-tapered dipole shown in Fig. 5.9 (dipole's axial dimensions: 15 mm × 20 mm)

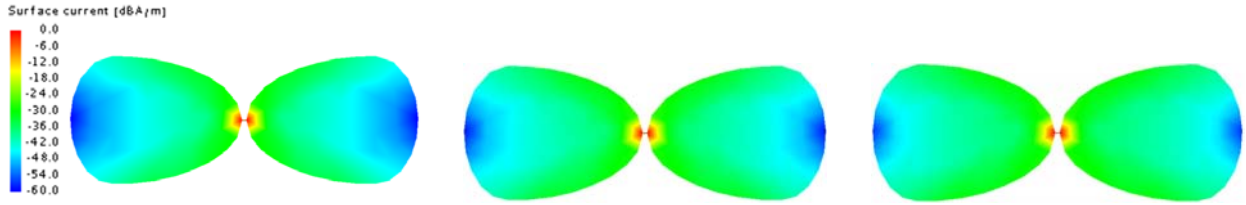

(a) f = 3.0 GHz (b) f = 4.0 GHz (c) f = 5.0 GHz

(d) f = 6.0 GHz (e) f = 7.0 GHz (f) f = 8.0 GHz

(g) f = 9.0 GHz (h) f = 10.0 GHz (i) f = 11.0 GHz

Fig. 5.12: Illustration of the distribution of surface current density at different frequencies for the scaled elliptically-tapered disc dipole antenna with performance characteristics shown in Fig. 5.11

5.3 UWB linear array

The UWB elliptically-tapered disc dipole, with VSWR and input impedance characteristics shown in Fig. 5.11, is used to construct a 17-element (N=8) linear array with element spacing d=17 mm as depicted in Fig. 5.13. The elements are assumed to lie on the yz-plane. The radiation pattern for an uncompensated design of this array with the desired total far-field pattern of $f(\theta) = G\left(\omega_p, \theta\right) = \sin^{50}\theta$ is shown in Fig. 5.14. As noted in Fig. 5.14a, the achieved radiation pattern varies significantly with frequency over the desired UWB bandwidth. This should be expected as the effects due to inter-element mutual coupling and variations of the element field with frequency are not accounted in an uncompensated array design. Variations of the input impedances versus frequency for half of the array elements including the center element for the uncompensated case are shown in Fig. 5.15. As noted in Fig. 5.15 the input impedance of the edge element (element 8) differs significantly from that of the center element. This behavior is largely due to the inter-element mutual coupling effect. A summary of performance parameters, including HP, D, and SLL is presented in Table 5.2.

The excitation currents at the input terminals of the elements for this array are shown in Fig. 5.16. Figure 5.16a illustrates variations of the current magnitudes versus frequency, while Fig. 5.16b shows how current phases vary with frequency. There are two sets of curves in each part of Fig. 5.16; the solid curves represent the currents calculated from (5.1) and (5.2), while the dashed curves represent the currents that are actually developed at the elements input ports under the influence of inter-element mutual coupling and are obtained by means of a software simulation tool (FEKO). Comparison of the solid and dashed curves indicates that for the case of uncompensated design the desired currents are not delivered to the input ports of the element antennas because mutual coupling effects are not accounted for in this design process.

The distributions of surface current densities for the elements of the array described in Fig. 5.14 are shown in Fig. 5.17. These distributions are shown only at two frequencies of 3 GHz and 11 GHz; the surface current distributions at other frequencies within the array bandwidth are presented Table C1 in Appendix C. Comparison of current distributions in Fig, 5.17 with those of an isolated element shown in Fig. 5.12 clearly indicates that the distributions for same element and at the same frequency are significantly different, particularly for the edge elements.

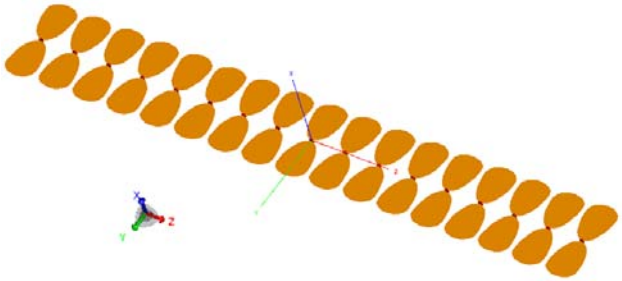

Fig. 5.13: Ultra-wideband linear array of 17 equally-spaced elliptically-tapered disc dipoles with element spacing $d = 17$ mm and element axial dimensions 15 mm × 20 mm

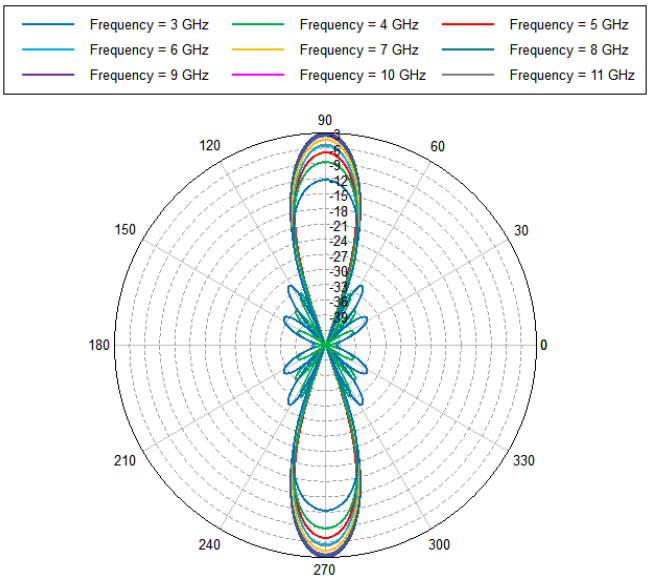

(a) Polar radiation patterns, 3dB/Div.

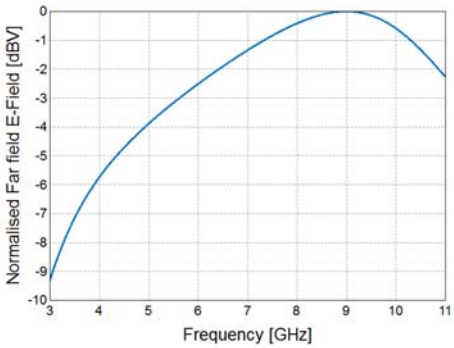

(b) Magnitude

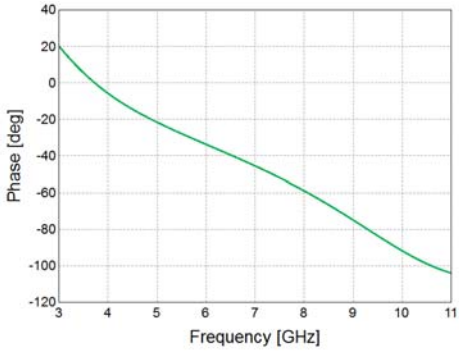

(c) Phase

Fig. 5.14: Variations of (a) total pattern, (b) magnitude of the total field at $\theta = 90^\circ$, and (c) phase of the total field at $\theta = 90^\circ$ versus frequency for an uncompensated linear array of elliptically-tapered disc dipoles with geometry and parameters same as those described in Fig. 5.13. The desired total array pattern is described by $f(\theta) = \sin^{50}\theta$ over the UWB frequency range of 3.1GHz to 10.6GHz.

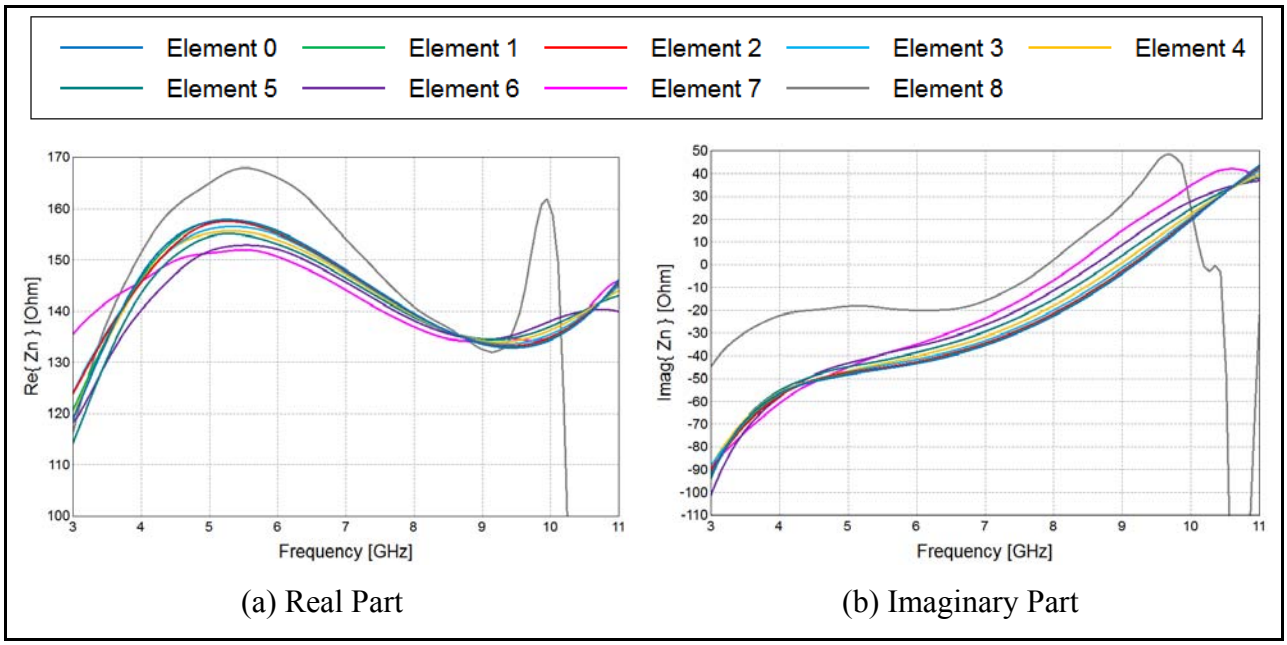

Fig. 5.15: Variations of input impedances versus frequency for half of the elements (elements 1-8) and the center element (element 0) of the array described in Fig. 5.14

Table 5.2: Summary of performance parameters including, half-power beamwidth (HP), directivity (*D*), and maximum sidelobe level (SLL) for the array described in Fig. 5.14

Frequency (GHz)	**Performance Parameters**		
	HP	*D*	SLL
3.0	19.0º	10.8 dB	-18.9 dB
4.0	16.0º	11.9 dB	-24.9 dB
5.0	14.3º	12.6 dB	-33.9 dB
6.0	13.6º	13.1 dB	-45.5 dB
7.0	13.4º	13.4 dB	< -58 dB
8.0	13.4º	13.5 dB	< -58 dB
9.0	13.4º	13.2 dB	< -58 dB
10.0	13.4º	12.3 dB	< -58 dB
11.0	13.0º	10.6 dB	< -58 dB

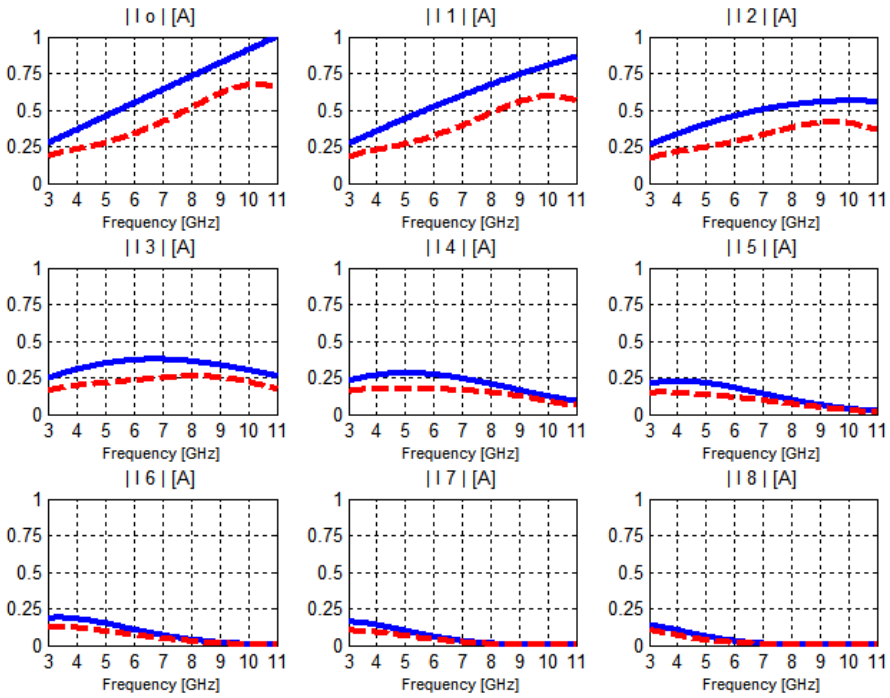

(a) Magnitude [A]

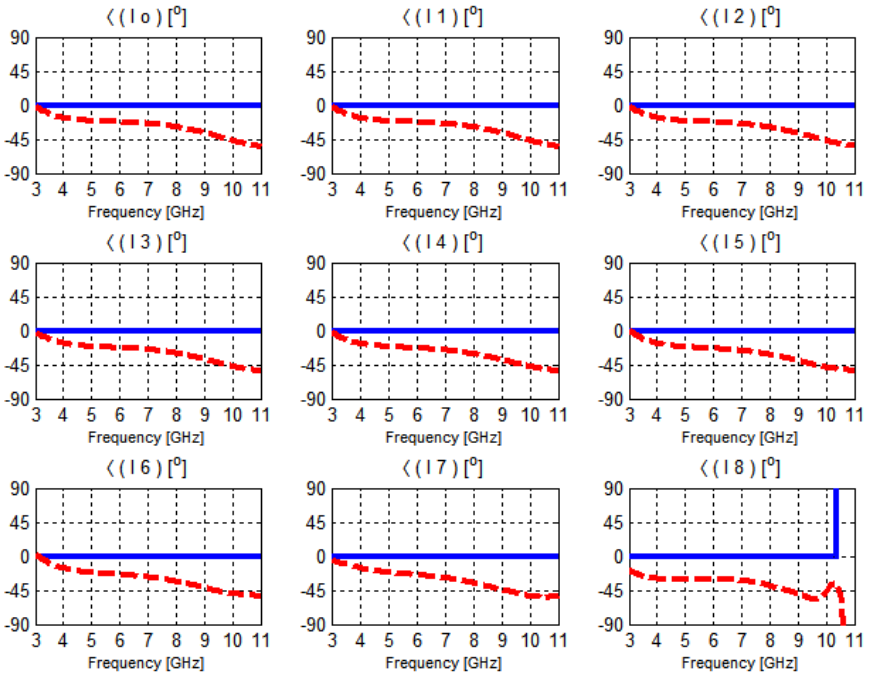

(b) Phase [°]

Fig. 5.16: Variations of excitation currents versus frequency for the elements of the array described in Fig. 5.14. Solid curves represent the currents calculated using (5.1) and (5.2), dashed curves represent the currents developed at the input ports of element antenna due to mutual coupling effects

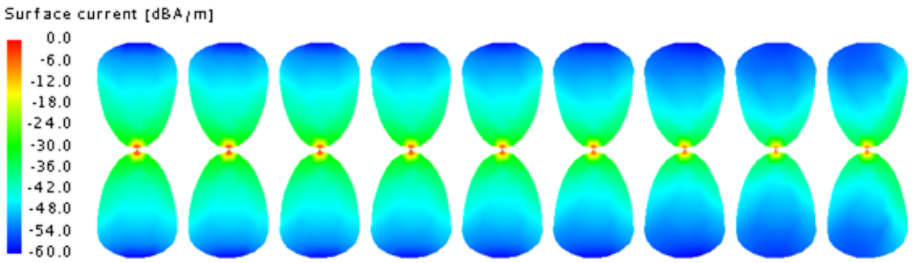

(a) f = 3.0 GHz

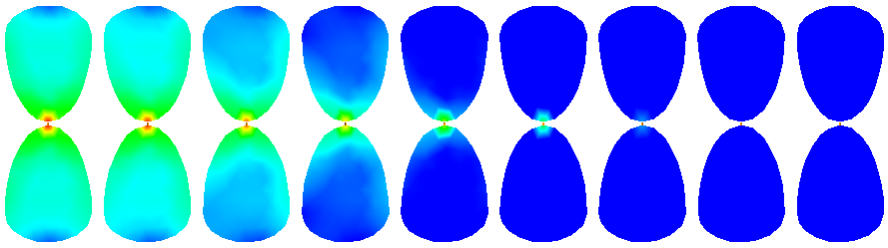

(b) f = 11.0 GHz

Fig. 5.17: Illustration of surface current distributions for half of the elements of the array described in Fig. 5.14 (center element shown on the left)

After compensations are implemented, radiation characteristics improve significantly as observed in Fig. 5.18. The excitation currents for the compensated design were calculated using (4.19) – (4.21) and (4.44). The phase of the desired total-field of the array, in the range of the half-power beamwidth, is adjusted to the nearest straight line that fits the uncompensated phase characteristic shown in Fig. 5.14c. Comparison of Figs. 5.14a and 5.18a indicates that the radiation pattern of the compensated array varies much less with frequency; however, the desired constant magnitude and linearly varying phase of the total field have not yet been achieved as noted in Figs. 5.18b and 5.18c. A summary of performance parameters and surface current distributions of elements for the compensated design of the array described in Fig. 5.18 are presented in Tables B2 and C2 in Appendices B and C. The currents at the input ports of the elements for half of the array and the center element are shown in Fig. 5.19. It is noted in Fig. 5.19 that after compensating for inter-element mutual coupling, the calculated currents and those

actually developed at the input ports of the elements become nearly the same in both magnitude and phase.

The performance of the array described in Figs. 5.18b and 5.18c with regard to magnitude and phase behaviors is due to using the isolated element field in the calculations performed in steps 1-3 of the design flow chart presented in Fig. 4.11. The resulting errors were not significant in the case of the wire dipole array discussed earlier in this chapter. In step 4 of the design process shown in Fig. 4.11, the errors in the total-field due to the active-element field are compensated. Fig. 5.20 shows the radiation characteristics of the array design of Fig. 5.18 after compensation of errors due to the active-element field have been made. As observed in Fig. 5.20, a nearly constant magnitude and a linearly varying phase for the total-field has been achieved. The results produced in Fig. 5.20 were obtained after one iteration starting from step 4 of the design process. However, comparison of patterns shown in Fig. 5.20a and Fig. 5.18a indicates that side-lobe levels have increased. The maximum SLL is -18 dB at 3GHz in Fig. 5.18a, while it is -16dB in Fig. 5.20a. Most practical UWB signals have low power spectral densities at the edges of the UWB band, making the increase in SLL at 3 GHz more tolerable. A summary of performance parameters and surface current distributions of elements for the compensated design based on the active-element field of the array described in Fig. 5.20 are presented in Tables B3 and C3 in Appendices B and C. The currents at the input ports of the elements for half of the array and the center element are shown in Fig. 5.21. It can be seen in Fig. 5.21 that the develped currents at the input ports of the elements match the calculated currents after compensation for inter-element mutual coupling using (4.44). It should be noted that the currents in Fig. 5.21, where (4.14) was used to calculate the array factor, differ from those of Fig. 5.16, where (4.32) was used to calculate the array factor.

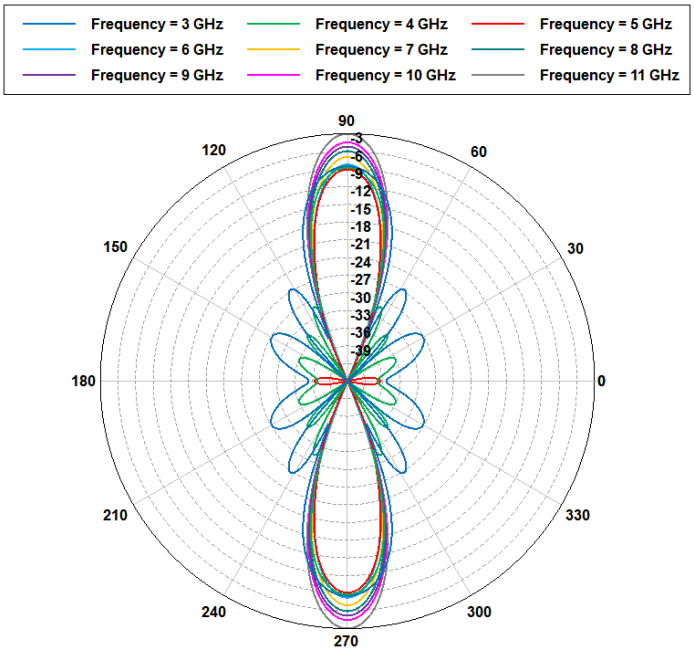

(a) 3dB/Div.

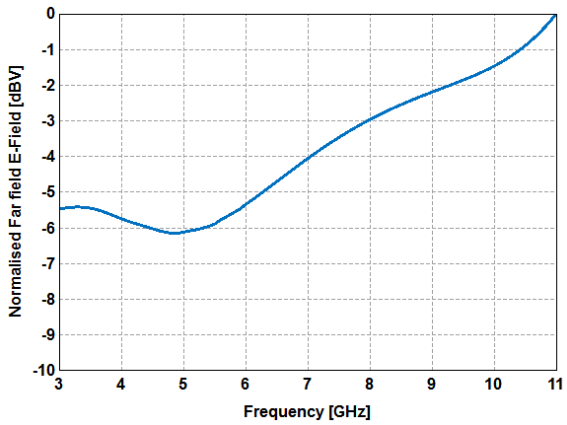

(b)

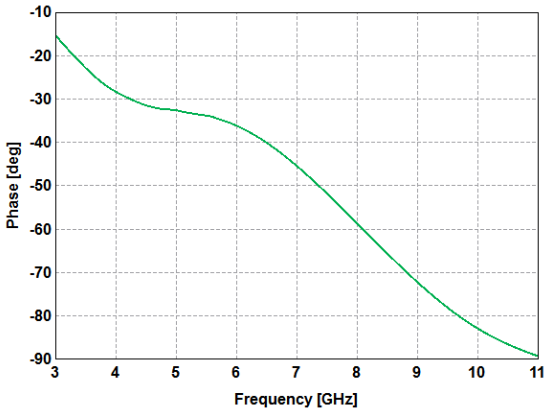

(c)

Fig. 5.18: Variations of (a) total pattern, (b) magnitude of the total field at $\theta = 90^{\circ}$, and (c) phase of the total field at $\theta = 90^{\circ}$ versus frequency for a compensated (based on isolated element assumption) linear array of elliptically-tapered disc dipoles with geometry and parameters same as those described in Fig. 5.13. The desired total array pattern is described by $f(\theta) = \sin^{50}\theta$ over the UWB frequency range 3.1GHz - 10.6GHz.

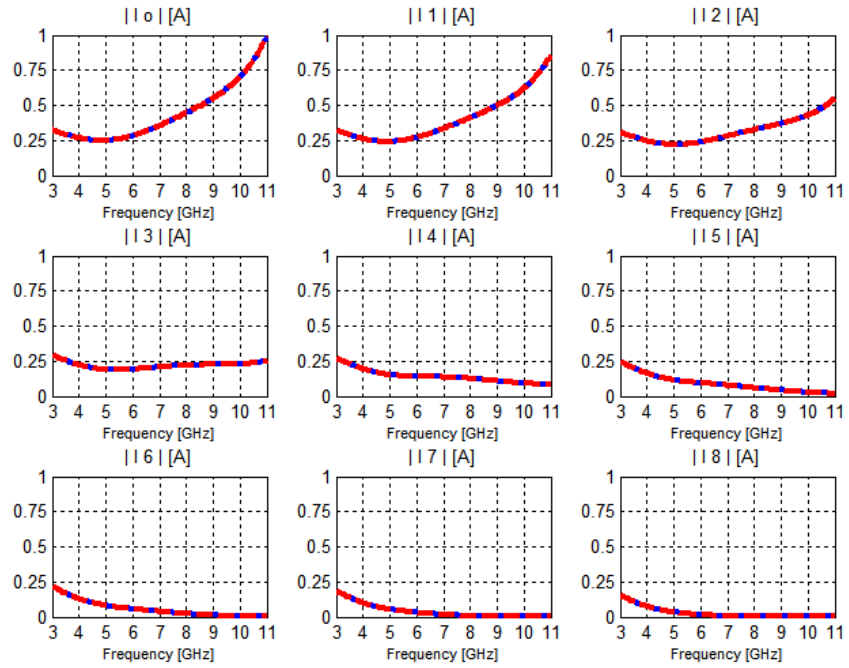

(a) Magnitude [A]

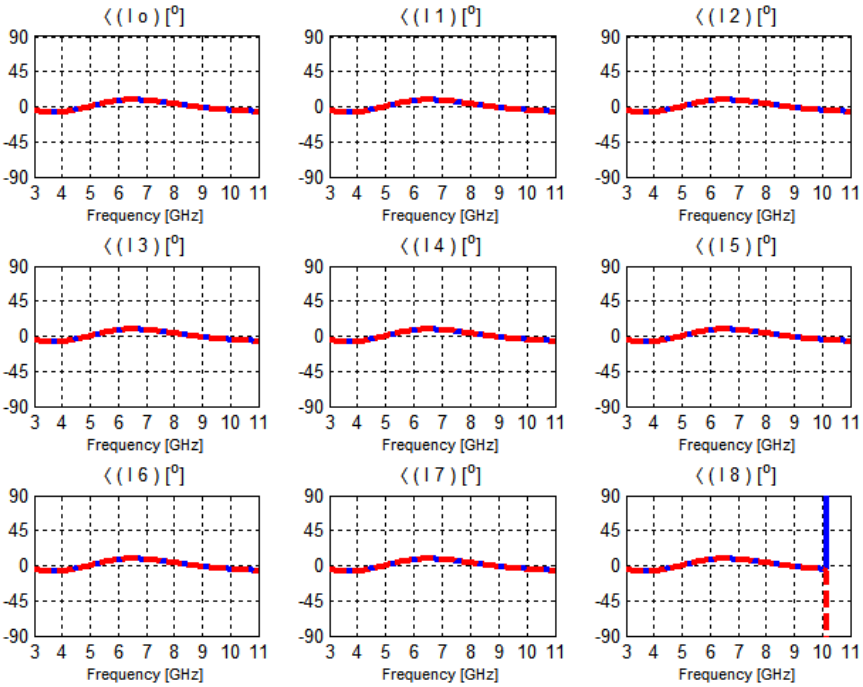

(b) Phase [°]

Fig. 5.19: Variations of excitation currents versus frequency for the elements of the array described in Fig. 5.18. Solid curves represent the currents calculated using (5.1) and (5.2), dashed curves represent the currents developed at the input ports of element antenna.

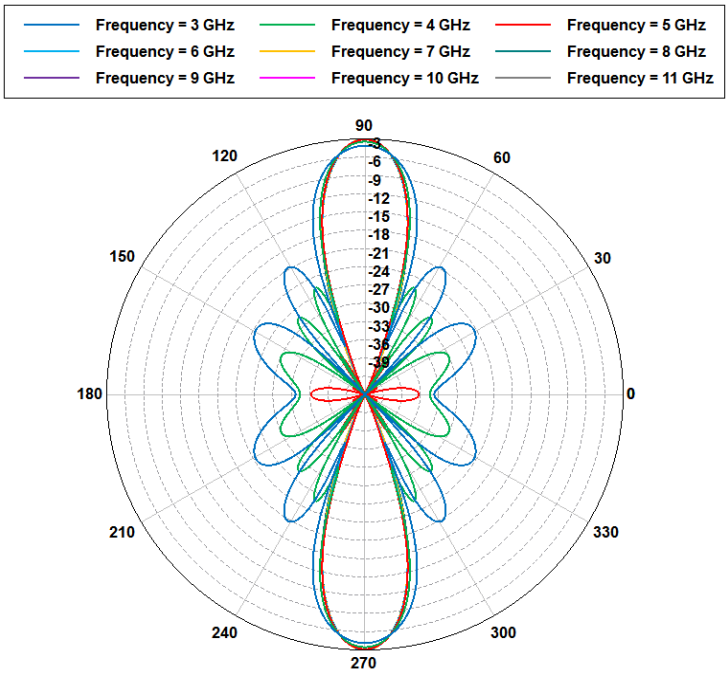

(a) 3dB/Div.

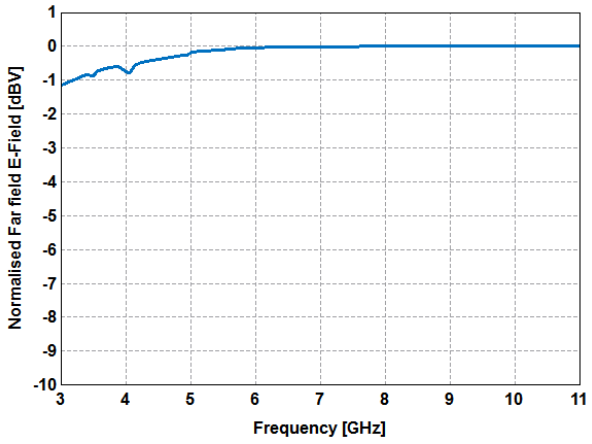

(b)

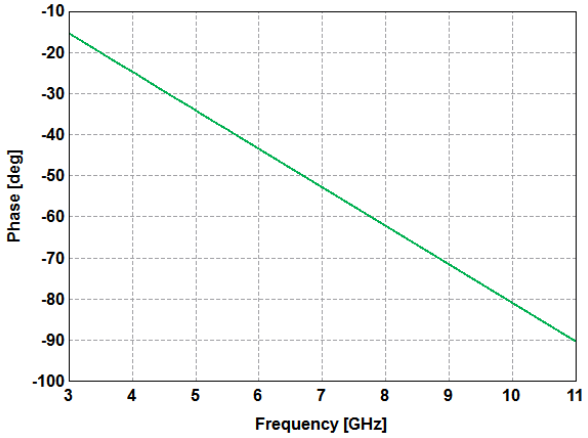

(c)

Fig. 5.20: Variations of (a) total pattern, (b) magnitude of the total field at $\theta = 90^{\circ}$, and (c) phase of the total field at $\theta = 90^{\circ}$ versus frequency for a compensated (based on active-element field) linear array of elliptically-tapered disc dipoles with geometry and parameters same as those described in Fig. 5.13. The desired total array pattern is described by $f(\theta) = \sin^{50}\theta$ over the UWB frequency range 3.1GHz - 10.6GHz.

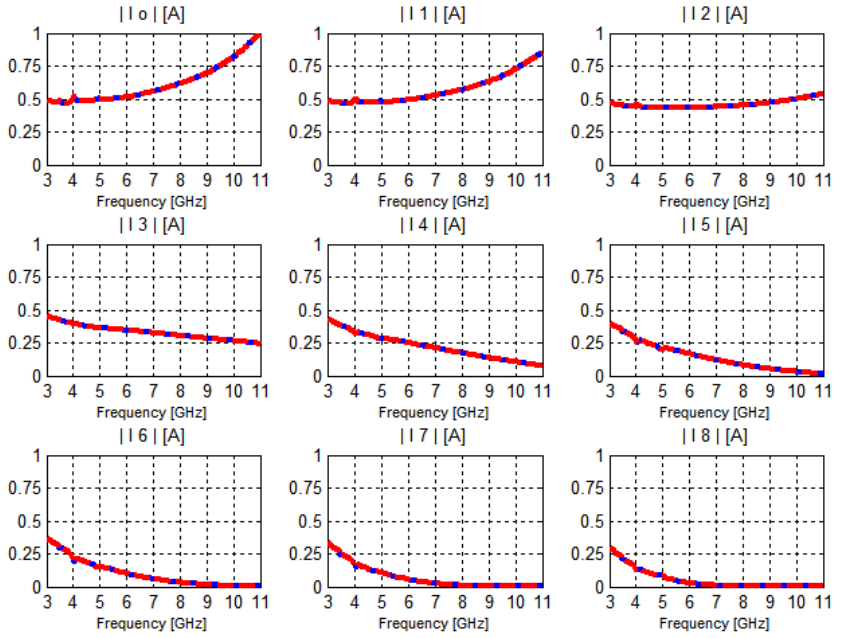

(a) Magnitude [A]

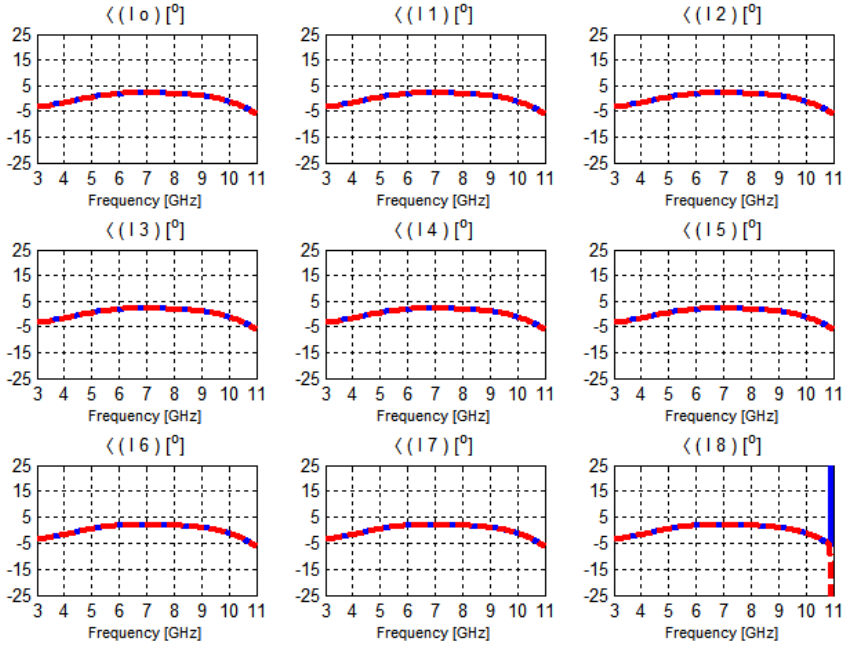

(b) Phase [°]

Fig. 5.21: Variations of excitation currents versus frequency for the elements of the array described in Fig. 5.20. Solid curves represent the currents calculated using (5.1) and (5.2), dashed curves represent the currents developed at the input ports of element antenna.

5.4 Transient response

In examining the transient response, the array antenna is treated as a linear time-invariant (LTI) system based on the fact the underlying governing equations, namely Maxwell's equations, are linear equations. The transient response of a UWB system may be more conveniently evaluated through the impulse response, which is simply the inverse Fourier transform of the transfer function of the system. The radiated total fields calculated in the previous sections are taken as the transfer functions of the respective arrays. Very narrow Gaussian pulses are useful models for impulse signals. Typical values for the standard deviation of UWB Gaussian pulses are in the order of nano or pico seconds, as discussed in [99, 100]. FCC regulations for UWB signals for medical imaging systems (FCC part 15.513) and for indoor UWB systems (FCC part 15.517) [101] state that the transmitted power in the frequency range of 3.1 GHz-10.6 GHz should not exceed 0.5 mW in order to minimize interference. This translates to a power spectral density (PSD) of approximately - 41.3 dBm/MHz. Usually these limits are enforced by applying a masking signal at the UWB transmitter, which according to (FCC part 15.503d) is defined as "an intentional radiator that, at any point in time, has a fractional bandwidth equal to or greater than 0.20 or has a UWB bandwidth equal to or greater than 500 MHz, regardless of the fractional bandwidth." In this study, un-masked UWB source signals are used to study the transient responses of the array designs that have been presented so far in this chapter. In some UWB systems, such as those used in medical imaging, the used signals utilize the entire UWB frequency range. The general time-domain analysis of an antenna is discussed in [102]. The formulation for the transient response is summarized in Appendix A. In Fig. 5.22, as an example case, the transient response of the wire-dipole antenna array is presented.

The radiation characteristics of a wire dipole antenna array in the frequency-domain for both uncompensated and compensated designs were discussed in section 5.1. To study the time-domain response of the array, a narrow Gaussian (approximating an impulse) is considered as the input signal. This input signal, $s(t)$, and its spectrum are shown in Fig.5.22a and Fig.5.22b, respectively. It is reminded that the bandwidth of the wire dipole array covers the frequency range $4.5\ \text{GHz}$ to $7.0\ \text{GHz}$. From Fig. 5.22b, one can tell that the bandwidth of the signal is much wider than the bandwidth of the array. The radiated output signals for the uncompensated and compensated cases are shown in Figs. 5.22c and 5.22d, respectively. Comparison of these

figures clearly indicates that the uncompensated design suffers more ringing effect than the compensated one.

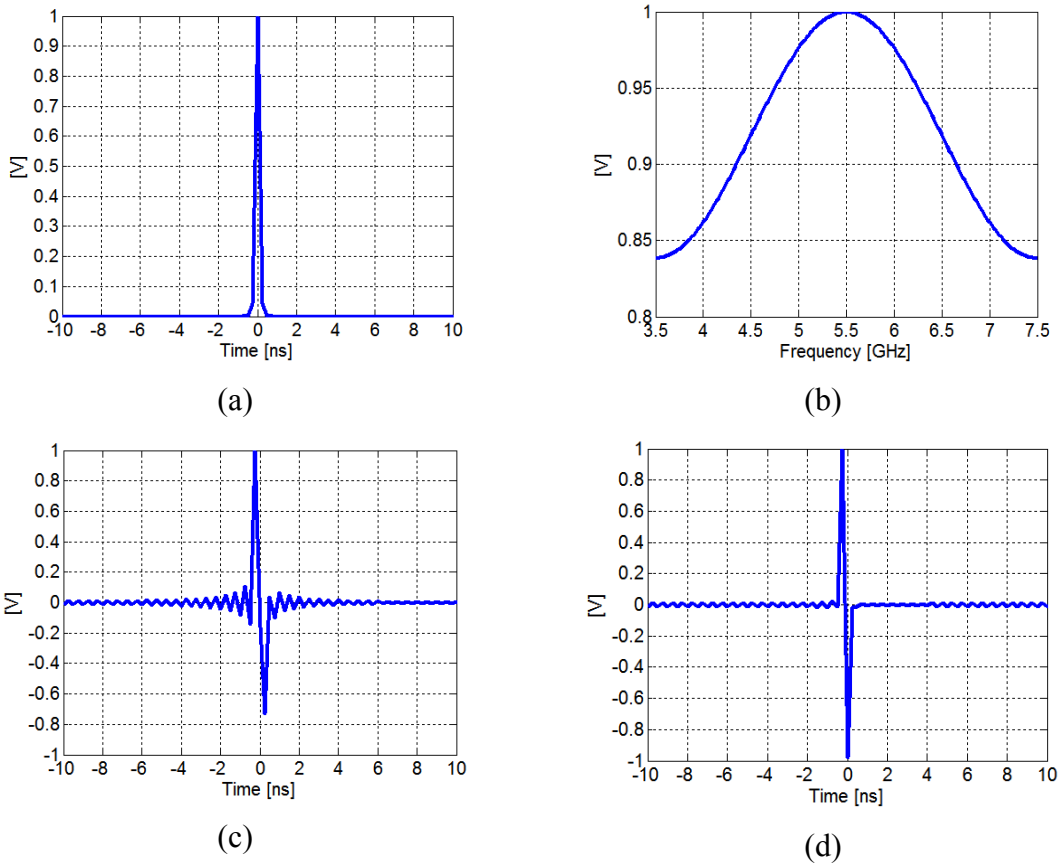

Fig. 5.22: Transient response of the wire dipole array configuration of Fig. 5.1; (a) Input Gaussian pulse with $\sigma = 0.1$ ns , (b) Spectrum of the modulated input signal, (c) Radiated pulse of the uncompensated design of Fig. 5.2 at $\theta = 90^{\circ}$, (d) Radiated pulse of the compensated design of Fig. 5.3 at $\theta = 90^{\circ}$

Chapter 6: Synthesis of Two-Dimensional Planar Arrays

In the previous chapters, a frequency adaptive array synthesis method was introduced, formulated, and tested for linear array designs. Beam forming and main-beam scanning by means of linear arrays can be controlled only on a single plane in space that contains the line of array. In other words, the array factor of a linear array, as a spatial function, is one dimensional, say a function of θ only. Thus, the beamwidth in a plane perpendicular to the line of array is determined solely by the beamwidth of the element antenna. In order to provide more directivity and beam scanning on two orthogonal planes, planar arrays whose array factors are function of two spatial coordinates (θ and ϕ) may be used. In this chapter, the application of the adaptive array synthesis technique is extended to two-dimensional planar arrays. Design examples using the same element antennas that were used in linear array designs in Chapter 5 are considered.

6.1 Formulation of planar array factor

Let us consider a planar rectangular array of $(2M+1)\times(2N+1)$ identical elements with centers of elements residing on the xy-plane. The entire array may be regarded as a linear array of $2M+1$ elements with element spacing d_x along the x-axis and array factor $AF_x(\theta_x)$, where θ_x is an angle measured from the x-axis. The constituting element of such array itself is another linear array of $2N+1$ elements along the y-axis with element spacing d_y and array factor $AF_y(\theta_y)$, where θ_y is an angle measured from the y-axis. It can be shown that the angles θ_x and θ_y are related to the spatial coordinates θ and φ through the relationships $\theta_x = \cos^{-1}\left(\sin\theta\cos\varphi\right)$ and $\theta_y = \cos^{-1}\left(\sin\theta\sin\varphi\right)$. The array factor $AF_y(\theta_y)$ serves as the element pattern for the array along the x-axis. Thus, based on the principle of pattern multiplication, the total array factor for the entire two-dimensional planar array is $AF(\theta,\varphi) = AF_x(\theta_x)AF_y(\theta_y)$.

Assuming that the center element of the array is situated at the origin and elements currents processes a symmetrical distribution described by $I_{mn} = I_{-mn} = I_{m(-n)}$, and $I_{mn} = I_m \cdot I_n$, then AF_x and AF_y are expressed as

$$AF_x(\theta,\phi) = I_{x0} + 2\sum_{m=1}^{M} I_{xm}\cos\left[(m\omega d_x / c)\sin\theta\cos\varphi\right] \qquad (6.1a)$$

$$AF_y(\theta,\phi) = I_{y0} + 2\sum_{n=1}^{N} I_{yn}\cos\left[(n\omega d_y / c)\sin\theta\sin\varphi)\right] \qquad (6.1b)$$

The expressions in (6.1a) and (6.1b) are very similar to (3.4) which is the array factor for a linear array. In fact, if θ in (3.4) is replaced with θ_x or θ_y equations (6.1a) or (6.1b) is obtained. These similarities allow us to employ much of formulations developed in Chapters 3-5 in analyzing two-dimensional planar arrays. Accordingly, if the array factors in (6.1) are sampled discretely in the frequency domain, they may be re-written in the following form:

$$AF_{xp}(\omega_p,\theta,\phi) = I_{x0p}(\omega_p) + 2\sum_{m=1}^{M} I_{xmp}(\omega_p)\cos\left[(m\omega_p d_x / c)\sin\theta\cos\varphi\right] \qquad (6.2a)$$

$$AF_{yp}(\omega_p,\theta,\phi) = I_{y0p}(\omega_p) + 2\sum_{n=1}^{N} I_{ynp}(\omega_p)\cos\left[(n\omega_p d_y / c)\sin\theta\sin\varphi)\right] \qquad (6.2b)$$

If the desired frequency-independent total far-field pattern of the array is described by the function $f(\theta,\varphi)$, the excitation currents in (6.2a) and (6.2b) are calculated using the patterns in the principal planes $\varphi = 0$ in AF_{xp} and $\varphi = 90^\circ$ in AF_{yp}. The results are summarized as

$$I_{xmp}(\omega_p) = \frac{1}{T_{xp}}\int_0^{\pi}\left[G(\omega_p,\theta,\varphi=0)/E_e(\omega_p,\theta,\varphi=0)\right]\cos\left[(md_x\omega_p / c)\cos\theta\right]\sin\theta\, d\theta, \quad -M \le m \le M \qquad (6.3a)$$

$$I_{ynp}(\omega_p) = \frac{1}{T_{yp}}\int_0^{\pi}\left[G(\omega_p,\theta,\varphi=90^\circ)/E_e(\omega_p,\theta,\varphi=90^\circ)\right]\cos\left[(nd_y\omega_p / c)\cos\theta\right]\sin\theta\, d\theta, \quad -N \le n \le N \qquad (6.3b)$$

where $E_e(\omega_p,\theta,\varphi)$ is the element field, $T_{xp} = \dfrac{2\pi c}{d_x\omega_p}$, $T_{yp} = \dfrac{2\pi c}{d_y\omega_p}$, and $|G(\omega_p,\theta,\varphi)| = f(\theta,\varphi)$ is the desired frequency-independent (UWB) radiation pattern of the array and $\angle G(\omega_p,\theta,\varphi) = -\alpha_0\omega_p$, ($\alpha_0$ = constant), is the phase of the total field which is expressed such that the desired linear dependence on frequency is maintained. Then, the current of the element

corresponding to *m*th row (in the x-direction) and *n*th column (in the y-direction) at frequency ω_p is obtained from

$$I_{mnp}(\omega_p) = I_{xmp}(\omega_p) I_{ynp}(\omega_p), \quad -M \le m \le M \text{ and } -N \le n \le N \tag{6.4}$$

To achieve scanning, the array factors in (6.2a) and (6.2b) should be modified as,

$$AF_{xp}(\omega_p, \theta, \phi) = I_{x0\,p} + 2\sum_{m=1}^{M} | I_{xmp}(\omega_p) | \cos\left[(m\omega_p d_x / c)(\sin\theta\cos\varphi - \sin\theta_0\cos\varphi_0 + \sin\theta_s\cos\varphi_s \right] \tag{6.5a}$$

$$AF_{yp}(\omega_p, \theta, \phi) = I_{y0\,p}(\omega_p) + 2\sum_{n=1}^{N} | I_{ynp}(\omega_p) | \cos\left[(n\omega_p d_y / c)(\sin\theta\sin\varphi - \sin\theta_0\sin\varphi_0 + \sin\theta_s\sin\varphi_s) \right] \tag{6.5b}$$

where θ_o and ϕ_o define the direction along which the magnitude of the unscanned main beam is maximum and θ_s and ϕ_s are the scan angles, defining the direction along which the main beam is desired to occur upon scanning. This modification amounts to replacing $I_{x\,mp}(\omega_p)$ in (6.3a) and $I_{y\,np}(\omega_p)$ in (6.3b) with $I_{x\,mp}(\omega_p)\exp(-\Psi_{ms})$ and $I_{y\,np}(\omega_p)\exp(-\Psi_{ns})$, respectively, where

$$\Psi_{ms} = \Psi^*_{-ms} = j(md_x\omega_p / c)(\sin\theta_s\cos\varphi_s - \sin\theta_0\cos\varphi_0) \tag{6.6a}$$

$$\Psi_{ns} = \Psi^*_{-ns} = j(nd_x\omega_p / c)(\sin\theta_s\sin\varphi_s - \sin\theta_0\sin\varphi_0) \tag{6.6b}$$

To reduce truncation errors due to using finite number of terms (ideally, infinite number of terms should be used) in the series in (6.2) and (6.5), excitation currents may be modified in the same manner as in linear arrays with the following results,

$$I_{mnp-\mathrm{mod}}(\omega_p) = \frac{I_{mnp}(\omega_p)}{| E_{tot}(\theta_0, \varphi_0, \omega_p) |} \tag{6.7}$$

where $E_{tot}(\theta_0, \varphi_0, \omega_p) = AF_{xp}(\theta_0, \varphi_0, \omega_p) AF_{yp}(\theta_0, \varphi_0, \omega_p) E_e(\theta_0, \varphi_0, \omega_p)$

Finally, taking into account inter-element mutual coupling, as explained in Chapter 3, the excitation voltages of the elements can be calculated as follows,

$$[V]_{(2M+1)\times(2N+1)} = Z_o\left([I]+[I-S]^{-1}[S]\right)_{\left[(2M+1)\times(2N+1)\right]^2}[I_m]_{(2M+1)\times 1}\left([I_n]^T\right)_{1\times(2N+1)} \qquad (6.8)$$

where I is the identity matrix, and $[\ ]^T$ represents a non-conjugate transpose.

6.2 Planar array of wire dipoles

The linear array of 17 wire dipole elements that was studied as a design example in section 5.1 is used here to construct a planar array. Seventeen such linear arrays are placed parallel to the x-axis, as shown in Fig. 6.1, to form a 17x17 planar array with element spacings $d_x = 0.4\lambda_r$ and $d_y = 0.6\lambda_r$ at the resonant frequency of $f_r = 5.5$ GHz. Equations (6.3), (6.4) and (6.6) to (6.8) are used to calculate the element excitation currents. The desired total pattern of the array is chosen to be

$$f(\theta,\phi) = \cos^{50}\theta \qquad (6.9)$$

which produces a half-power beamwidth of $HP \approx 13.5^\circ$

The radiation patterns for $\theta_s = \phi_s = 0^\circ$ are shown in Fig. 6.2. It is noted that these patterns remain essentially unchanged over the frequency rang 4.5 GHz to 7.0 GHz. However, as expected, the directivity of the planar array is significantly larger than that of the 17-element linear array. Summaries of performance parameters of the planar array designs presented in this chapter are provided in Appendix B. The magnitude and phase characteristics of the total radiated field along the direction of maximum radiation ($\theta = 0^\circ$) are shown in Fig. 6.3. It is seen in Fig. 6.3 that phase varies linearly with frequency and variations of the magnitude are quite small, validating the application of the proposed technique in synthesizing wideband/UWB planar arrays.

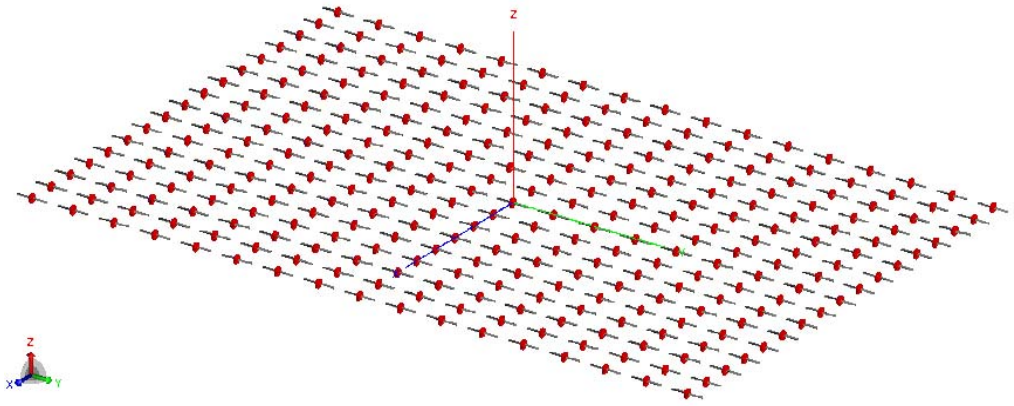

Fig. 6.1: Planar array of 17x17 wire dipoles constructed based on the linear array of Fig. 5.1. The array parameters are: element spacing in the x-direction $d_x = 0.4\lambda_r$, element spacing in the y-direction $d_y = 0.6\lambda_r$, dipole length $L = 0.48\lambda_r$; resonant frequency $f_r = 5.5$ GHz

The main-beam of the total-field produced by the array of Fig. 6.1 is scanned to the direction specified by coordinates $\theta_s = 45^\circ$ and $\phi_s = 0^\circ$. The same equations used to calculate the element excitations for the results in Fig. 6.2 are used with $\theta_s = 45^\circ$ and $\phi_s = 0^\circ$. The 3-D patterns of the magnitude of the total-field, scanned to the mentioned direction, are shown in Fig. 6.4. It is noted from Fig. 6.4e and Fig.6.4f that grating-lobes, or a back-lobe in this specific scan direction, start to appear at higher frequencies. The principal array factor contributing to these grating lobes is AF_x. The back-lobe shown in Fig. 6.4f is 15 dB below the maximum level of the scanned main beam. Next, ϕ_s is increased from zero to $\phi_s = 25^\circ$, while keeping $\theta_s = 45^\circ$. Figure 6.5 shows the two principal-plane array factors with applied linear phase-shift to element excitations to achieve main beam scanning. It is observed from Fig. 6.5b that AF_y suffers from appearance of grating lobes at the upper frequency limit of the bandwidth. On the other hand, grating lobes in AF_x shown in Fig. 6.5a do not appear even though its main beam is scanned to a direction farther than that of AF_y, because $d_x < d_y$. The patterns of the total field of the array with $\theta_s = 45^\circ$ and $\phi_s = 25^\circ$ are shown in Fig. 6.6. The maximum side-lobe level in Fig. 6.6f corresponding to 7.0 GHz is about 15 dB below the maximum level in the scanned direction.

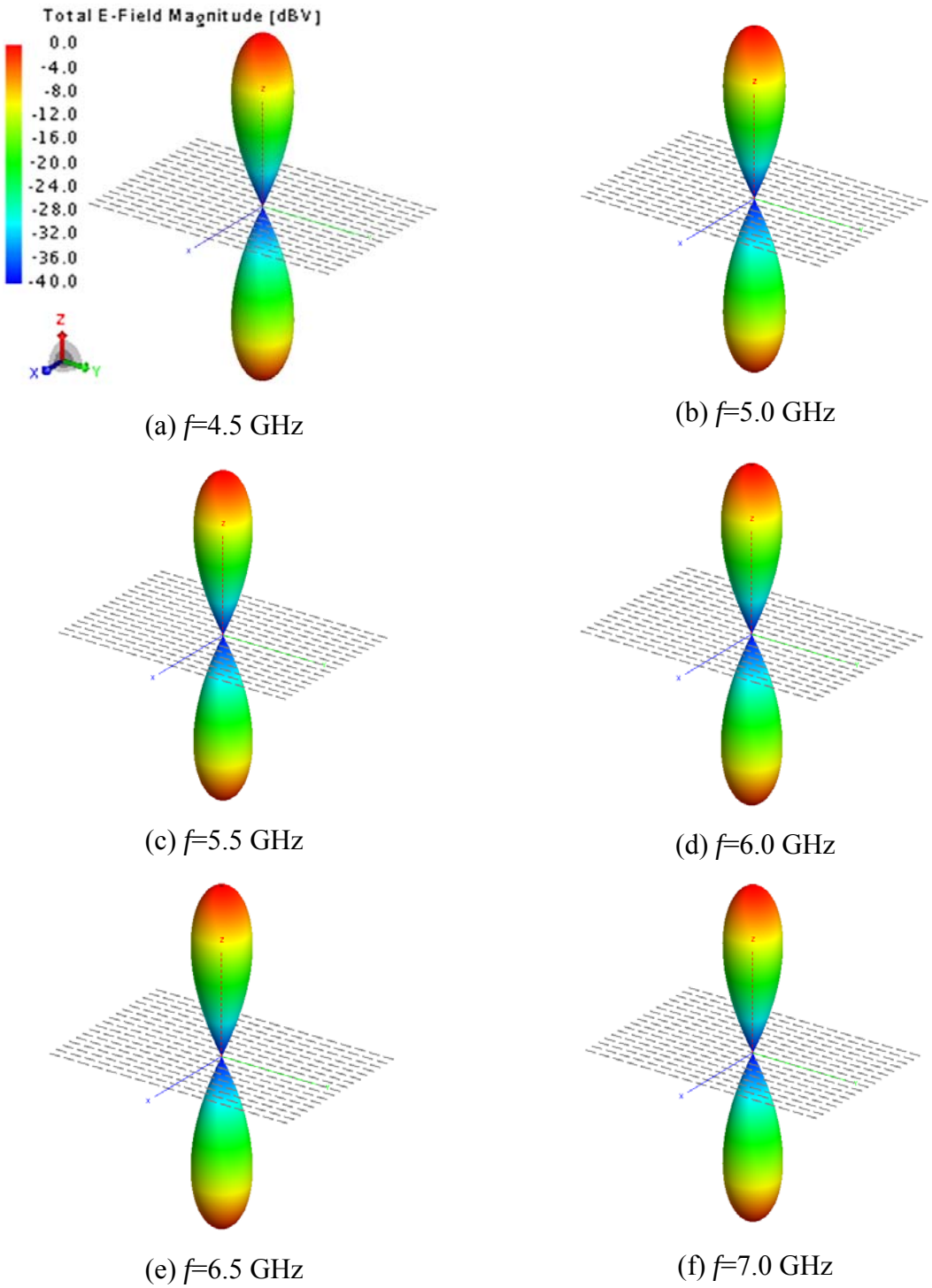

(a) f=4.5 GHz

(b) f=5.0 GHz

(c) f=5.5 GHz

(d) f=6.0 GHz

(e) f=6.5 GHz

(f) f=7.0 GHz

Fig. 6.2: Three-dimensional magnitude patterns at different frequencies for the total field of a planar array of wire dipoles with scan angles $\theta_s = \phi_s = 0^\circ$. The geometry and parameters of the array are the same as those described in Fig 6.1. The desired total array pattern used in the design is given by $f(\theta, \varphi) = \cos^{50}\theta$ over the bandwidth of the array, covering the frequency range of 4.5GHz to 7.0GHz. The corresponding performance parameters (HP, D, and SLL) are presented in Table B4.

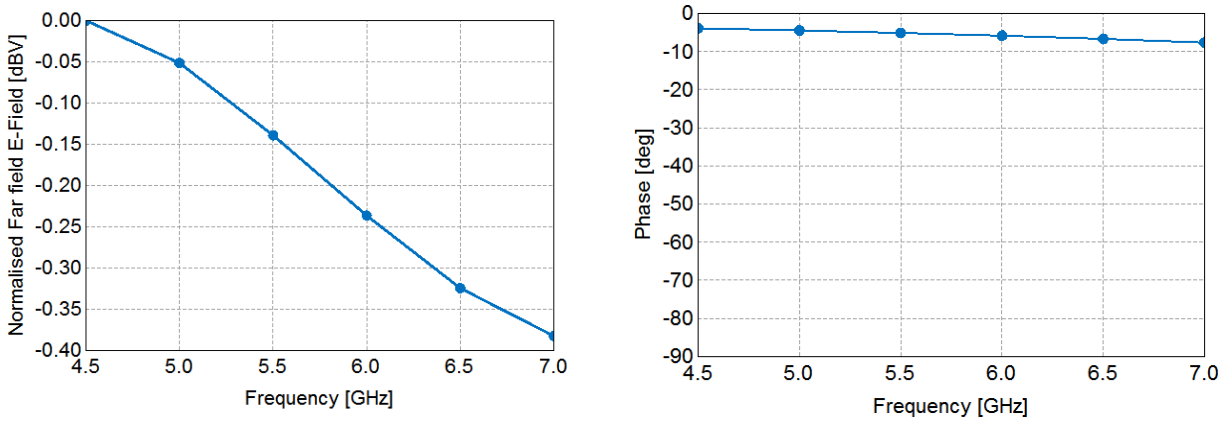

(a) (b)

Fig. 6.3: Variations of (a) magnitude of the total field at $\theta = 0^\circ$ and (b) phase of the total field at $\theta = 0^\circ$ versus frequency for the planar array of wire dipoles described in Fig.6.2

In order to produce more directional radiation patterns, a ground plane can be used as a reflector. The first consideration is to place the ground plane appropriately for the reflected field to be in-phase with the forward radiated field on an average sense within the desired bandwidth. To achieve this goal, a distance equal to $\lambda_c / 4$ between the ground plane and the plane of the array, where $\lambda_c = c / f_c$ with f_c being the center frequency of the bandwidth, is chosen. For the planar wire dipole array of Fig. 6.1, we have $f_c = 5.75$ GHz. We first examine the field of a single wire dipole element above an infinite ground plane with a distance of $\lambda_c / 4$, as shown in Fig. 6.7. The three-dimensional radiation patterns of the field of the element antenna of Fig. 6.7 are shown in Fig. 6.8. It is noted that over the frequency range of interest (4.5 GHz to 7.0 GHz), the total pattern of the element and ground plane remain essentially unchanged, indicating that an array of these elements above the ground plane is expected to provide about the same bandwidth when excitation current are determined based the synthesis technique introduced in this work. The planar array of wire dipoles above ground plane is shown in Fig. 6.9. The inter-element mutual coupling in Fig. 6.9 is different from that of the array configuration of Fig. 6.1. The reason for this difference is the presence of the image of the planar array below the ground plane, as is well known based on the image theory. Figure 6.10 illustrates the total radiation patterns of the array of Fig. 6.9 at several frequencies. Examination of Fig. 6.10 indicates that the total pattern remains relatively unchanged over the bandwidth of the array 4.45 GHz – 7.0 GHz, although the side-lobe level at 7.0 GHz (Fig. 6.10f) increased slightly compared to the case when ground plane was not included (Fig. 6.6f).

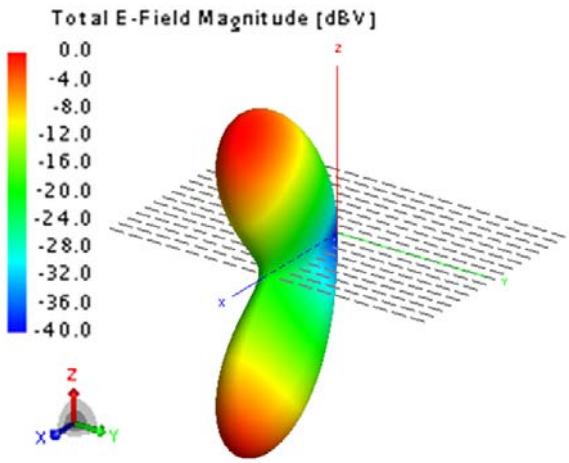

(a) f=4.5 GHz

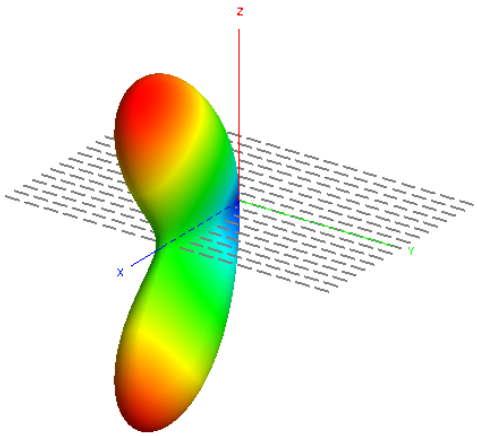

(b) f=5.0 GHz

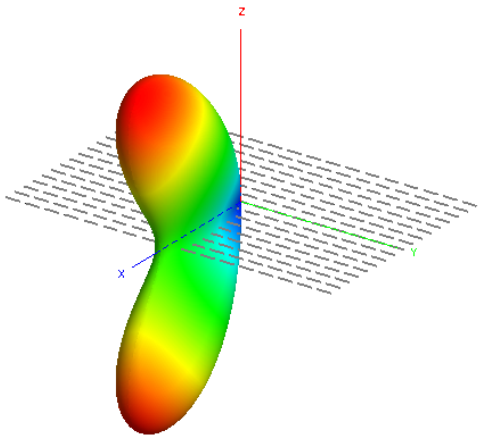

(c) f=5.5 GHz

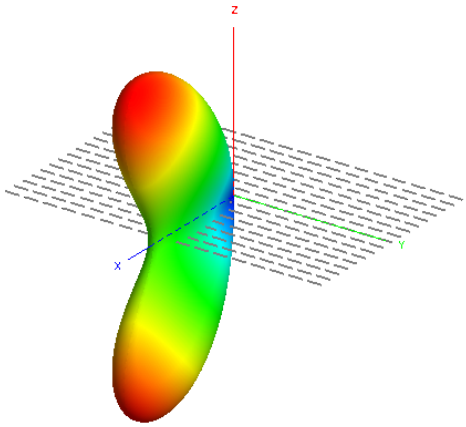

(d) f=6.0 GHz

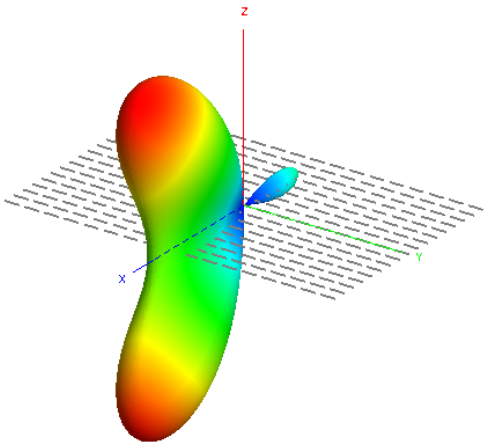

(e) f=6.5 GHz

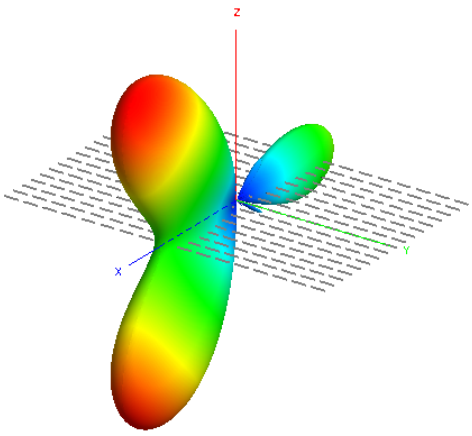

(f) f=7.0 GHz

Fig. 6.4: Three-dimensional magnitude patterns at different frequencies for the total field of the planar array of wire dipoles described in Fig. 6.2 but with scan angles $\theta_s = 45^\circ$ and $\phi_s = 0^\circ$. The corresponding performance parameters (HP, D, and SLL) are given in Table B5.

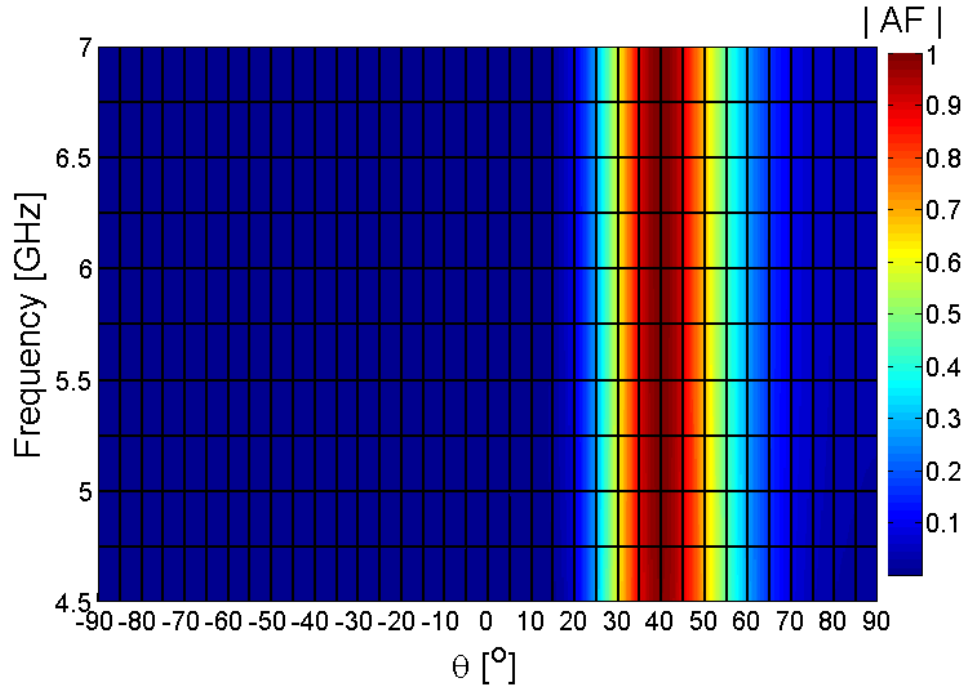

(a) AF_x

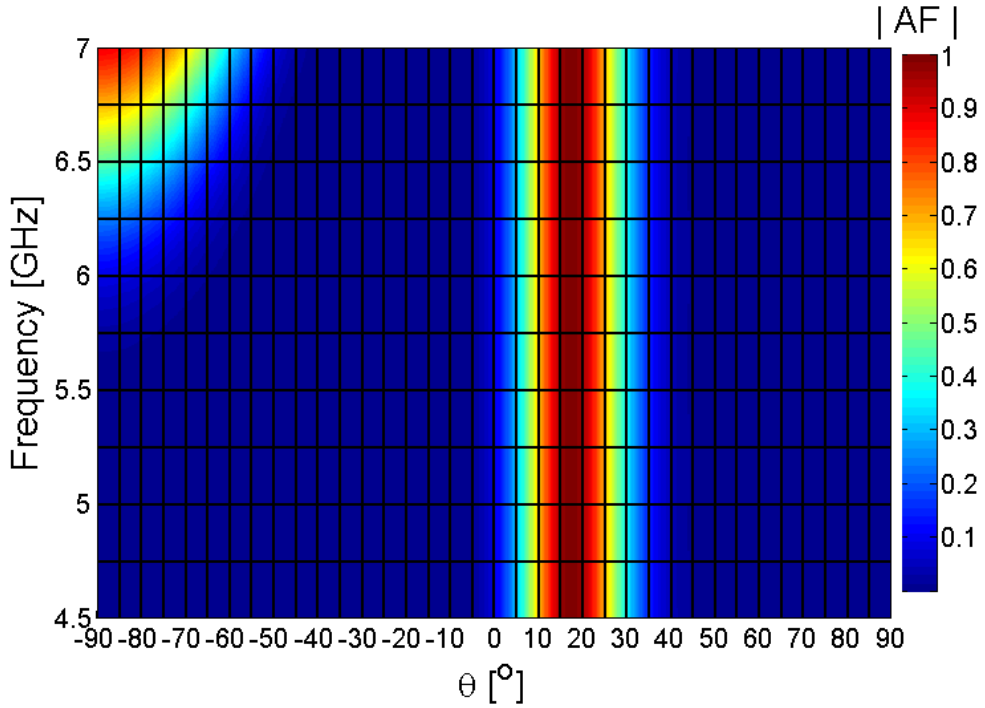

(b) AF_y

Fig. 6.5: Variations of the calculated principal-plane array factors versus frequency and angle θ for the planar array of wire dipoles described in Fig. 6.2 but with scan angles $\theta_s = 45^\circ$, $\phi_s = 25^\circ$. (a) AF_x, (b) AF_y

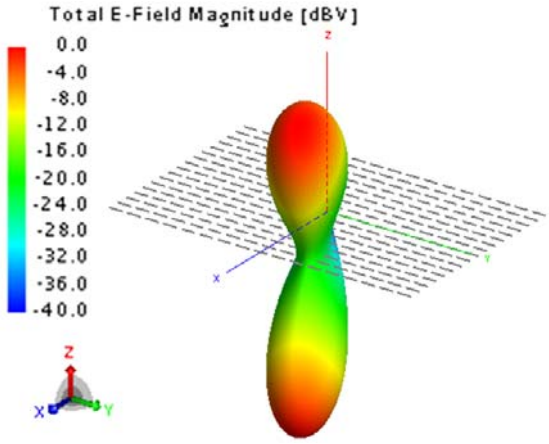

(a) f=4.5 GHz

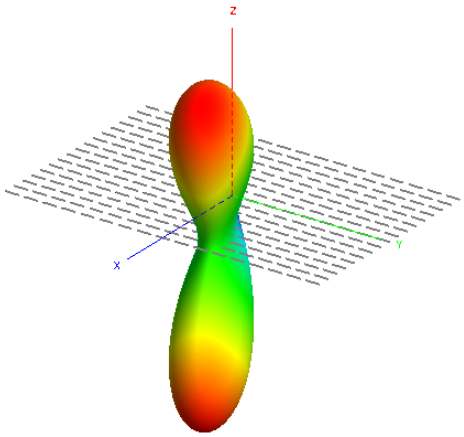

(b) f=5.0 GHz

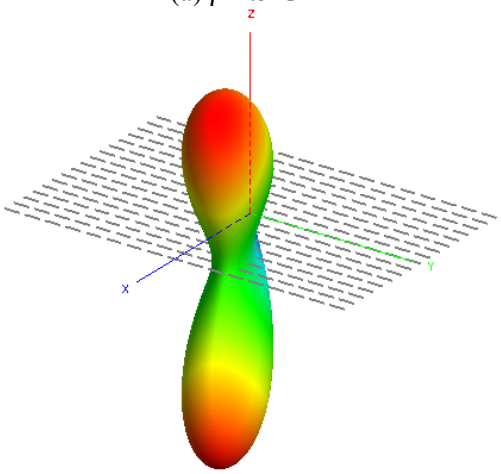

(c) f=5.5 GHz

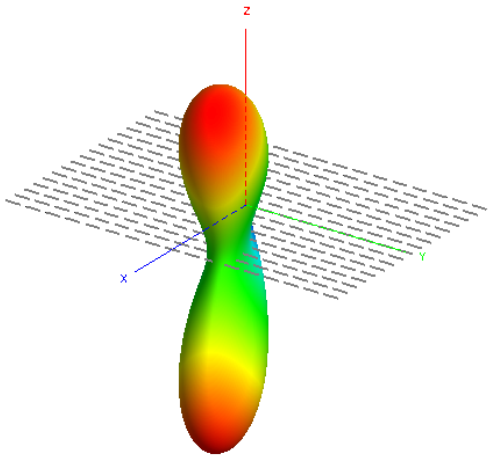

(d) f=6.0 GHz

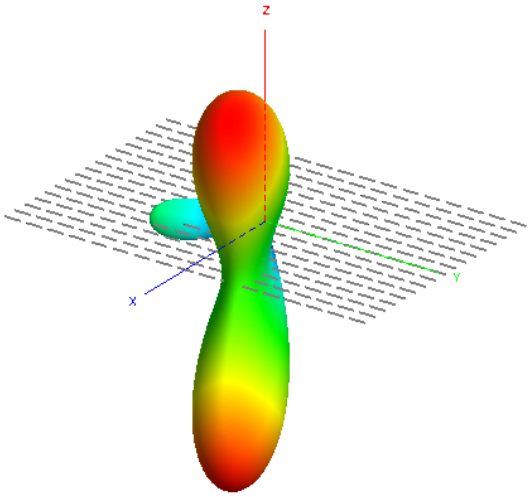

(e) f=6.5 GHz

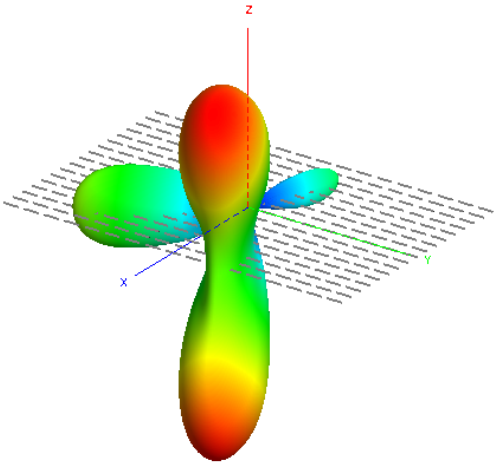

(f) f=7.0 GHz

Fig. 6.6: Three-dimensional magnitude patterns at different frequencies for the total field of the planar array of wire dipoles described in Fig. 6.2 but with scan angles $\theta_s = 45^\circ$, $\phi_s = 25^\circ$. The corresponding performance parameters (HP, D, and SLL) are provided in Table B6.

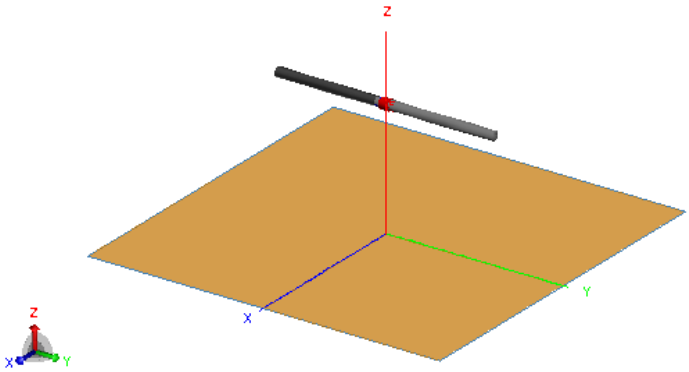

Fig. 6.7: Wire dipole antenna, used as an element in the planar array of Fig. 6.1, above an infinite ground plane by a distance of $h = \lambda_c / 4$ with $f_c = 5.75$ GHz

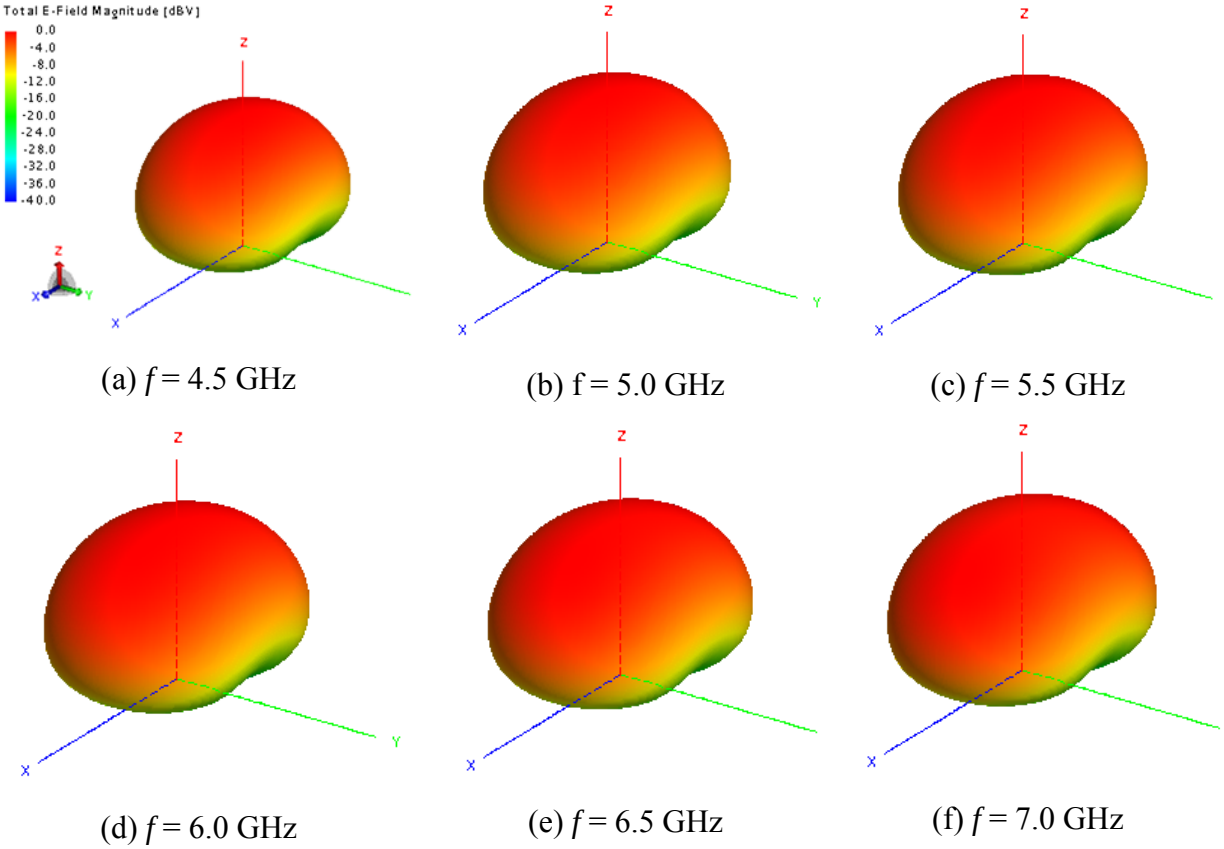

(a) $f = 4.5$ GHz (b) f = 5.0 GHz (c) $f = 5.5$ GHz

(d) $f = 6.0$ GHz (e) $f = 6.5$ GHz (f) $f = 7.0$ GHz

Fig. 6.8: Three-dimensional magnitude patterns at different frequencies for the total field of a single wire dipole antenna above an infinite perfectly-conducting ground plane. The dipole has a length $L = \lambda_c / 2$ and is a distance $h = \lambda_c / 4$ above the ground plane; $f_c = 5.75$ GHz.

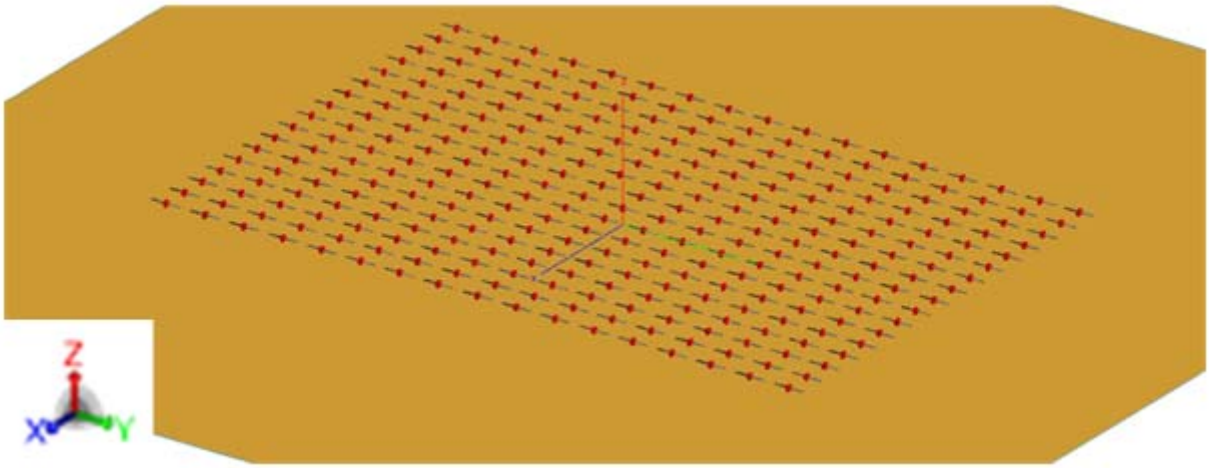

Fig. 6.9: A planar array of wire dipoles above an infinite ground plane. The array is assumed to have the same geometry, parameters and desired total pattern as that described in Figs. 6.1 and 6.2. The ground plane and plane of array are parallel and separated by a distance of $h = \lambda_c / 4$ at $f_c = 5.75$ GHz.

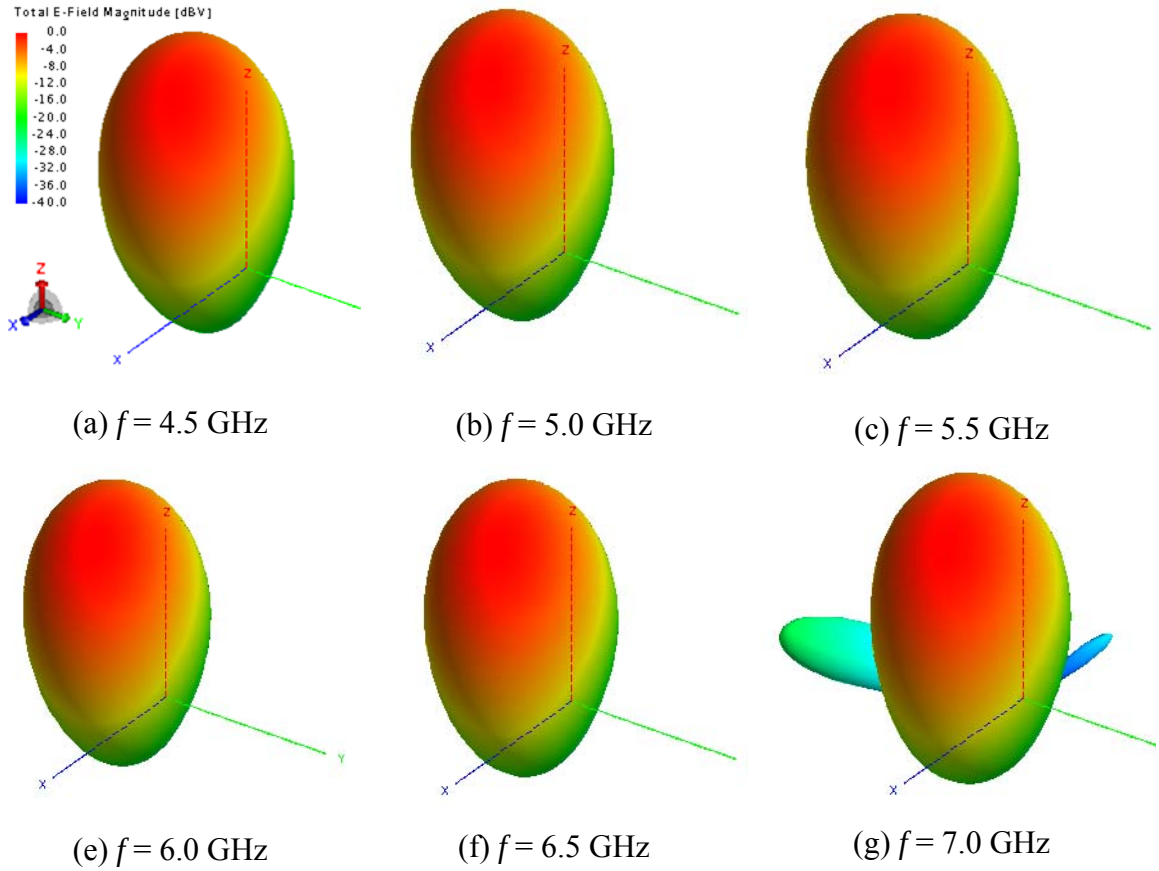

(a) $f = 4.5$ GHz (b) $f = 5.0$ GHz (c) $f = 5.5$ GHz

(e) $f = 6.0$ GHz (f) $f = 6.5$ GHz (g) $f = 7.0$ GHz

Fig. 6.10: Three-dimensional magnitude patterns at different frequencies for the total field of the planar array of wire dipoles above ground plane described in Fig. 6.9; scan angles are $\theta_s = 45^\circ$, $\phi_s = 25^\circ$. The corresponding performance parameters (HP, D, and SLL) are presented in Table B7.

6.3 Elliptical dipole planar array

The linear array of elliptically-tapered disc dipoles studied in Chapter 5and illustrated in Fig. 5.12, is used here to construct a planar array of 15x15 ($M = 7$, $N = 7$) elements, as shown in Fig. 6.11. For scan angles $\theta_s = 25^\circ$ and $\phi_s = 0^\circ$, the principal-plane array factors are calculated using the desired total pattern described by the function $f(\theta,\phi) = \cos^{50}(\theta - \theta_s)$. These principal-plane array factors are illustrated in Fig. 6.12. As noted in Fig. 6.12b, large grating lobes in the principal array factor AF_y begin to emerge when frequency exceeds 5.5 GHz, limiting the bandwidth to the frequency range 3.0 GHz to 5.5 GHz. Figure 6.13 shows the three-dimensional magnitude total radiation pattern of the array configuration of Fig. 6.11. The maximum side-lobe level for radiation patterns at all frequencies shown in Fig. 6.13 is around -15dB. As in the case of the linear array of elliptical dipoles studied in Chapter 5, errors due to active-element field are significant in this array design. The impact of these errors is evident in Fig. 6.14, which shows that the magnitude and phase characteristics of the total field of the array, along the direction of scan angles, do not exhibit the targeted performance of constant magnitude and linear phase variations with frequency. The active-element errors are compensated using an approach similar to that described in step 4 of the flow chart in Fig. 4.11, using a modified array factor given by

$$G^a(\theta,\phi,\omega) = \left[f(\theta,\phi) / E_e^i(\theta_s,\phi_s,\omega) \right] \cdot \left[f(\theta_s,\phi_s) / E_{tot}^a(\theta_s,\phi_s,\omega) \right] \qquad (6.10)$$

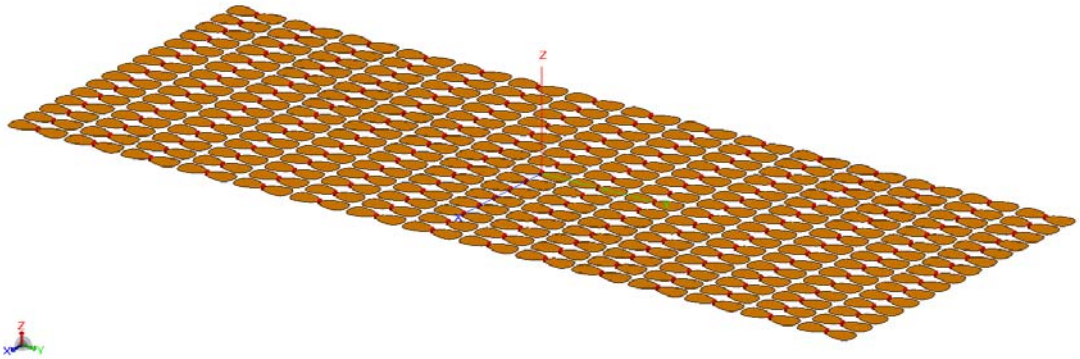

Fig. 6.11: Planar array of 15x15 elliptically-tapered disc dipoles constructed based on the linear array of Fig. 5.12. The array parameters are: element spacing in the x-direction $d_x = 17$ mm , element spacing in the y-direction $d_y = 43$ mm , and element axial dimensions $15\text{ mm} \times 20\text{ mm}$. The desired total array pattern is considered to be $f(\theta,\varphi) = \cos^{50}\theta$.

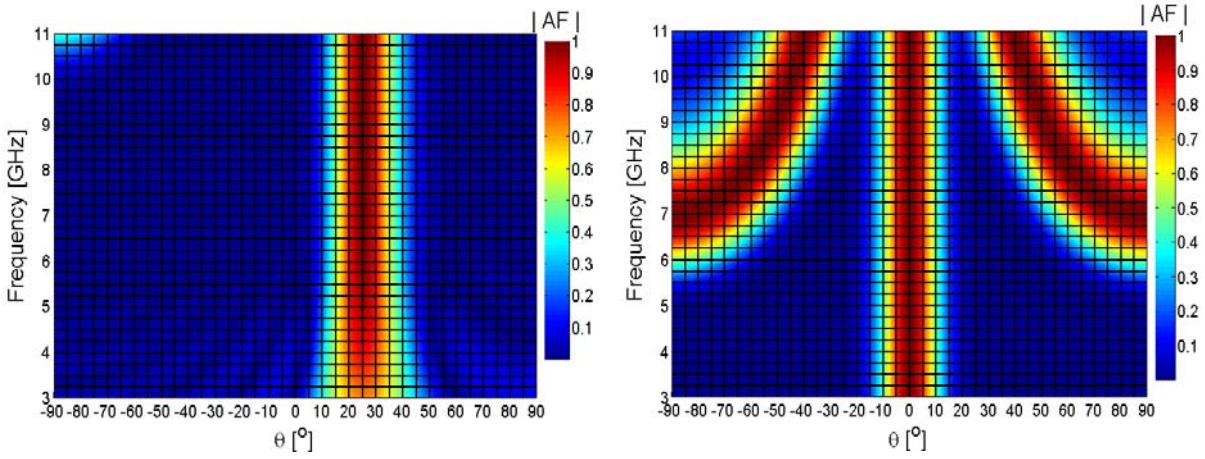

(a) AF_x (b) AF_y

Fig. 6.12: Variations of the calculated principal-plane array factors versus frequency and angle θ for the planar array of elliptical dipoles described in Fig. 6.11 but with scan angles $\theta_s = 25^\circ, \phi_s = 0^\circ$ (a) AF_x, (b) AF_y

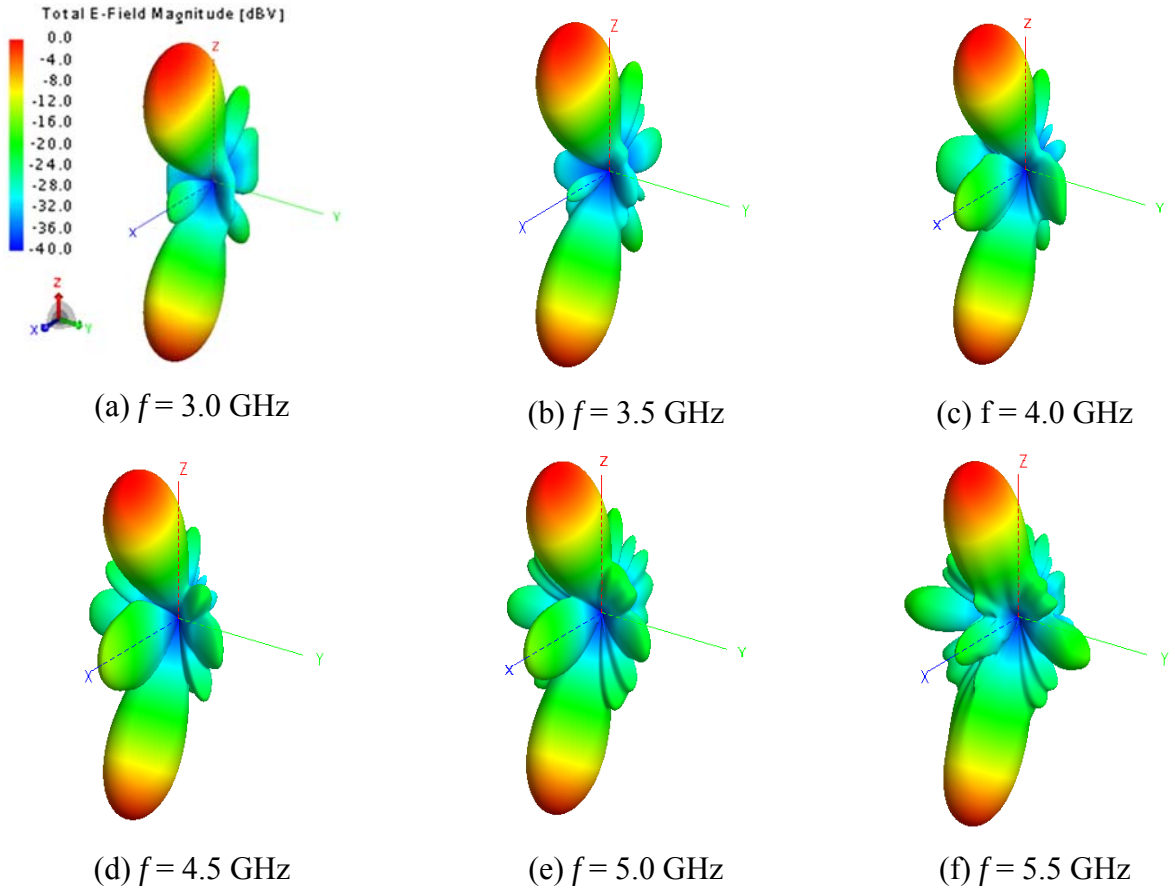

(a) $f = 3.0$ GHz (b) $f = 3.5$ GHz (c) f = 4.0 GHz

(d) $f = 4.5$ GHz (e) $f = 5.0$ GHz (f) $f = 5.5$ GHz

Fig. 6.13: Three-dimensional magnitude patterns for the total-field of the planar array described in Fig. 6.12. The corresponding performance parameters (HP, D, and SLL) are provided in Table B8.

The element excitations are calculated using (6.4-6.6). The radiation patterns of the array design of Fig. 6.11, after compensating for active-element error are nearly identical to those shown in 6.13. It can be seen in Fig. 6.15 that the magnitude of the total field of the array after compensating for active-element error is significantly more uniform than that of Fig. 6.14, and with significantly better phase performance.

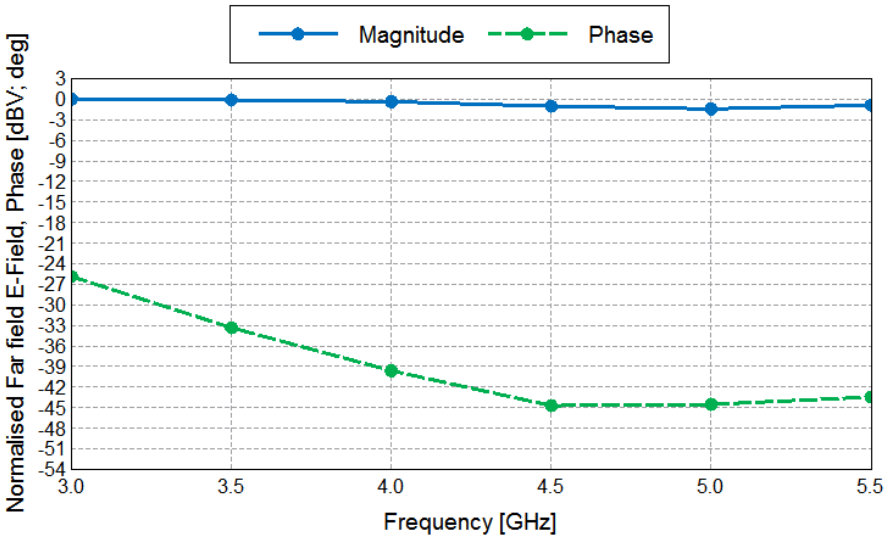

Fig. 6.14: Variations of the magnitude and phase versus frequency for the total field of the planar array of elliptical dipoles described in Fig. 6.13 at $\theta_s = 25^\circ$, $\phi_s = 0^\circ$. The corresponding performance parameters (HP, D, and SLL) for this array are provided in Table B8.

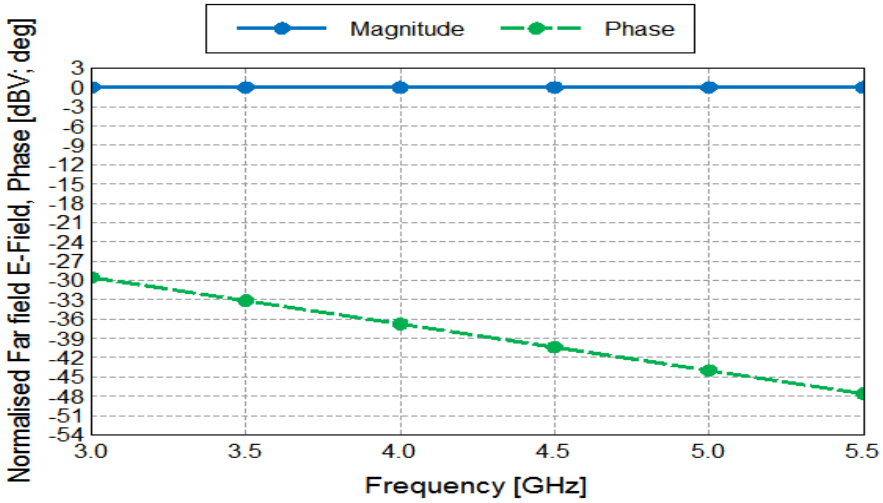

Fig. 6.15: Variations of the magnitude and phase versus frequency for the total field of the planar array of Fig. 6.13 at $\theta_s = 25^\circ$, $\phi_s = 0^\circ$ after compensating for active-element errors. The corresponding performance parameters (HP, D, and SLL) for this case are presented in Table B9.

In order to provide a more directive total pattern for the planar array of the elliptical dipoles, an infinite ground plane is placed below the plane of the array by a distance equal to $\lambda_{mid}/4$ at $f_{mid} = 4.25$ GHz, as shown in Fig. 6.16. The radiation pattern of an isolated elliptical dipole element antenna above an infinite ground plane is shown in Fig. 6.17. As noted in Fig. 6.17, the radiation pattern of this element antenna over a ground plane remains largely omni-directional over the design bandwidth, indicating that the separation of $\lambda_{mid}/4$ between the ground plane and plane of the array is a reasonable choice. The radiation patterns at several frequencies for the total field of the array of Fig. 6.16 are shown in Fig. 6.18.The maximum sidelobe level, similar to the case without ground plane, remains around -15dB. The performance of the array in Fig. 6.18 has not quite reached the goal of constant magnitude and linear phase variations with frequency as is evident in Fig. 6.19. This is of course due to errors resulting from the use of isolated element field in (6.3). Equation (6.10) is used to calculate the principal-plane array factors necessary to compensate for such errors, then element current excitations are calculated from (6.4) to (6.6). The radiation pattern for the total field of the array described in Fig. 6.18 after compensating for active-element field error remains essentially unchanged. The total field of the array after compensating for active-element errors meets the required performance of uniform magnitude and linear phase over the required bandwidth as shown in Fig. 6.20.

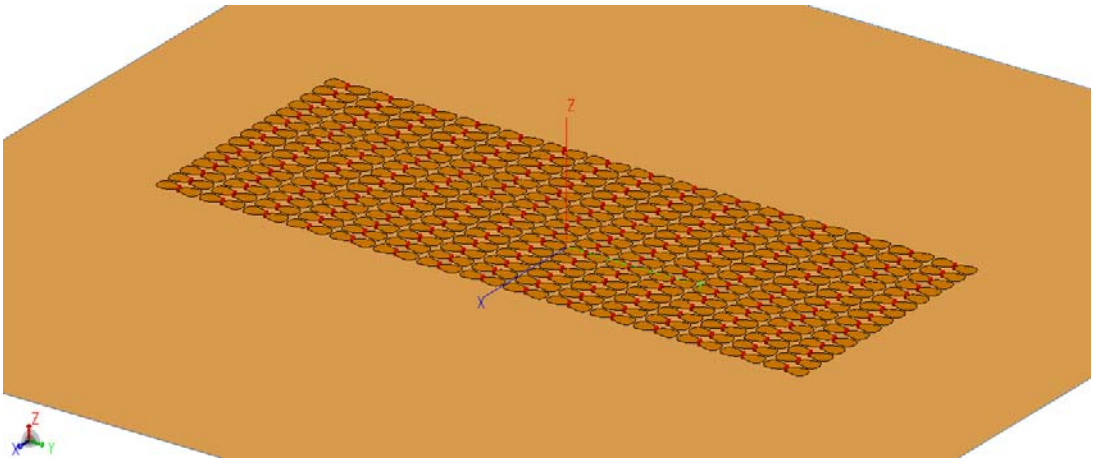

Fig. 6.16: Planar array of elliptical dipoles with the same geometry and parameters as those described in Fig. 6.11. The array is above an infinite ground plane by a distance of $h = \lambda_{mid}/4$ at $f_{mid} = 4.25$ GHz.

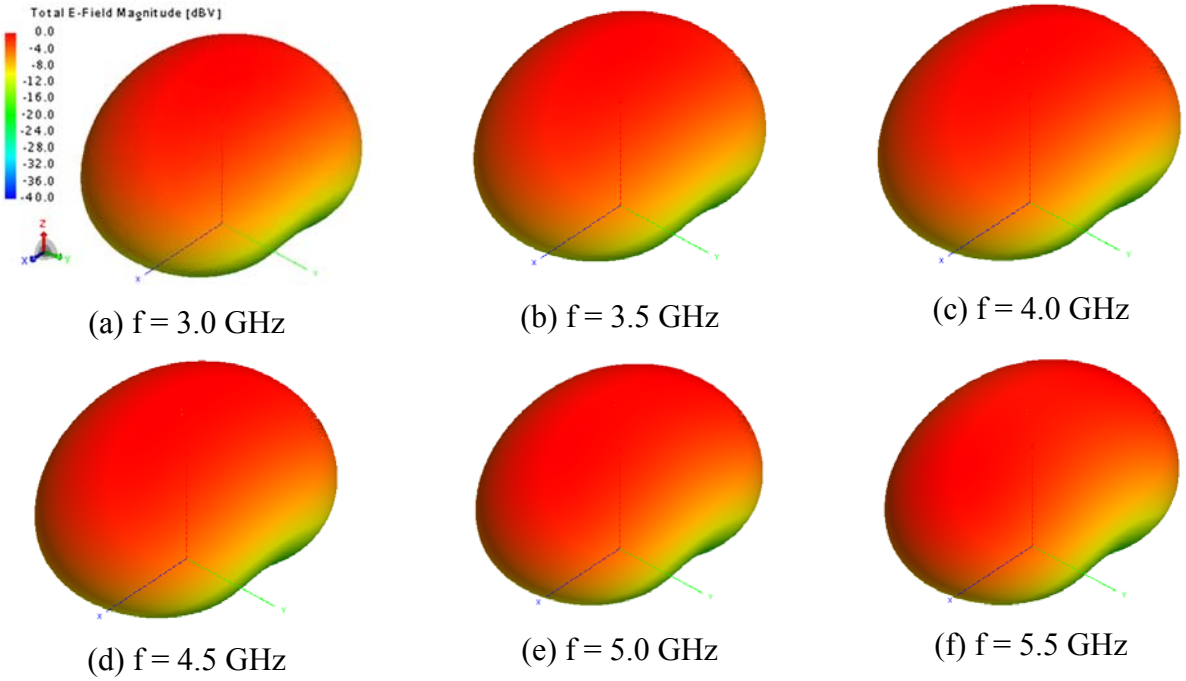

(a) f = 3.0 GHz (b) f = 3.5 GHz (c) f = 4.0 GHz

(d) f = 4.5 GHz (e) f = 5.0 GHz (f) f = 5.5 GHz

Fig. 6.17: Three-dimensional radiation patterns at several frequencies for an isolated elliptical dipole antenna above an infinite ground by a distance $\lambda_{mid}/4$ at $f_{mid} = 4.25$ GHz

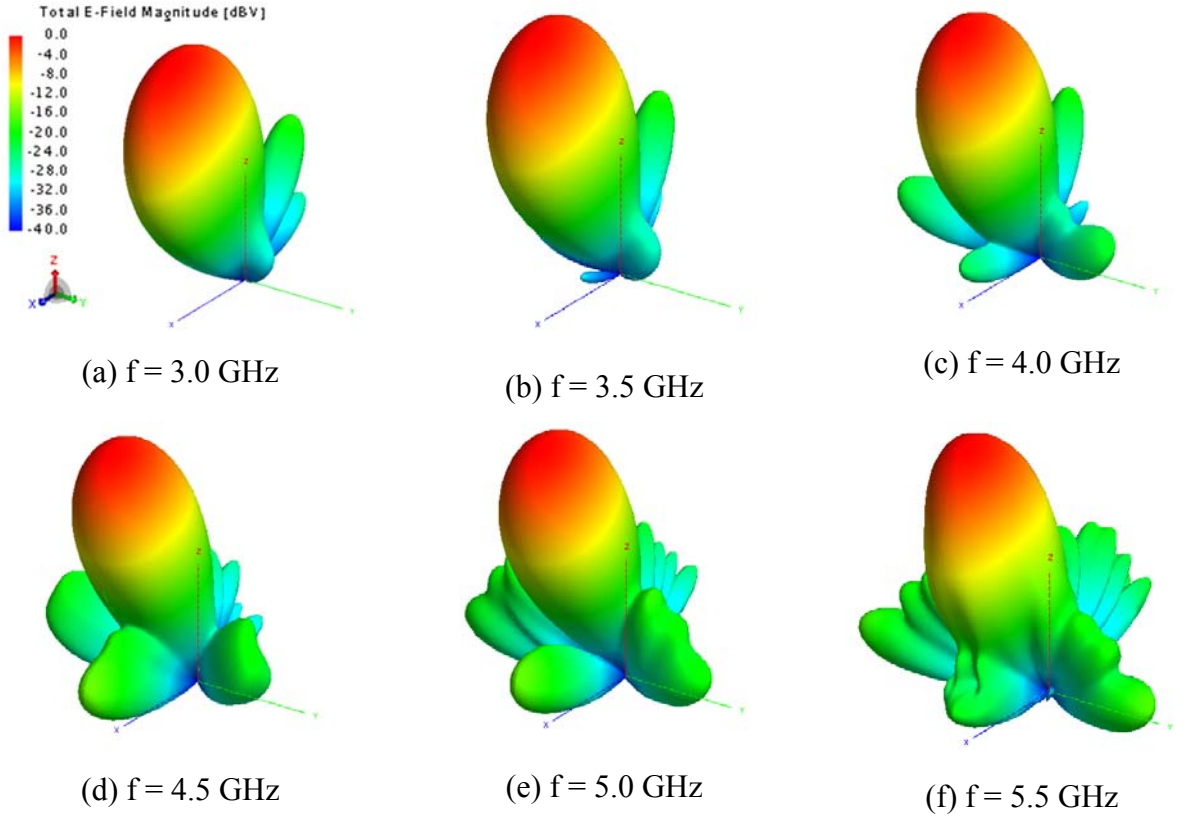

(a) f = 3.0 GHz (b) f = 3.5 GHz (c) f = 4.0 GHz

(d) f = 4.5 GHz (e) f = 5.0 GHz (f) f = 5.5 GHz

Fig. 6.18: Three-dimensional magnitude patterns for the total-field of the planar array described in Fig. 6.16 at $\theta_s = 25^\circ$, $\phi_s = 0^\circ$ .The corresponding performance parameters (HP, D, and SLL) are given in Table B9.

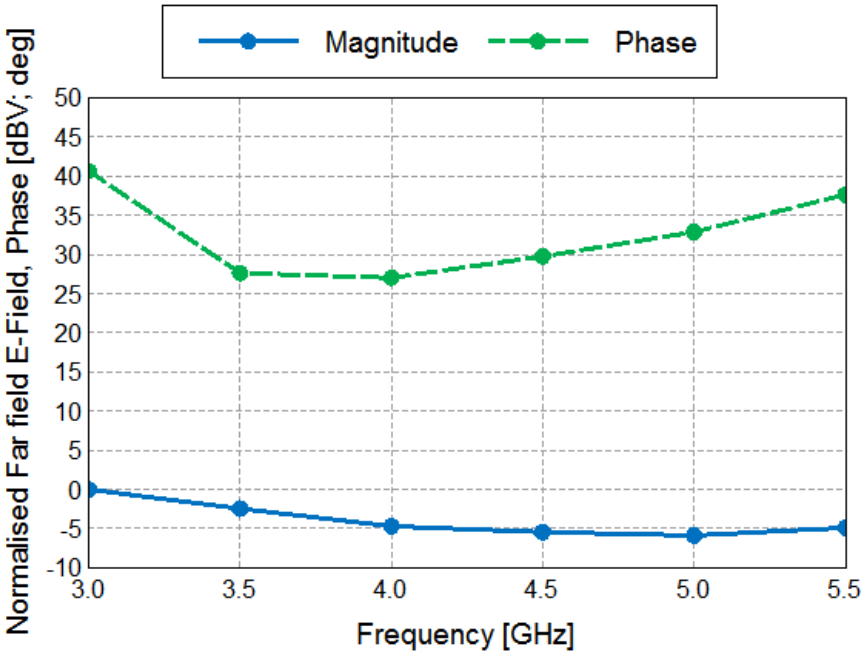

Fig. 6.19: Variations of the magnitude and phase versus frequency for the total field of the planar array of Fig. 6.18 at $\theta_s = 25^\circ$, $\phi_s = 0^\circ$ before compensating for active-element errors. The corresponding performance parameters (HP, D, and SLL) for this case are presented in Table B10.

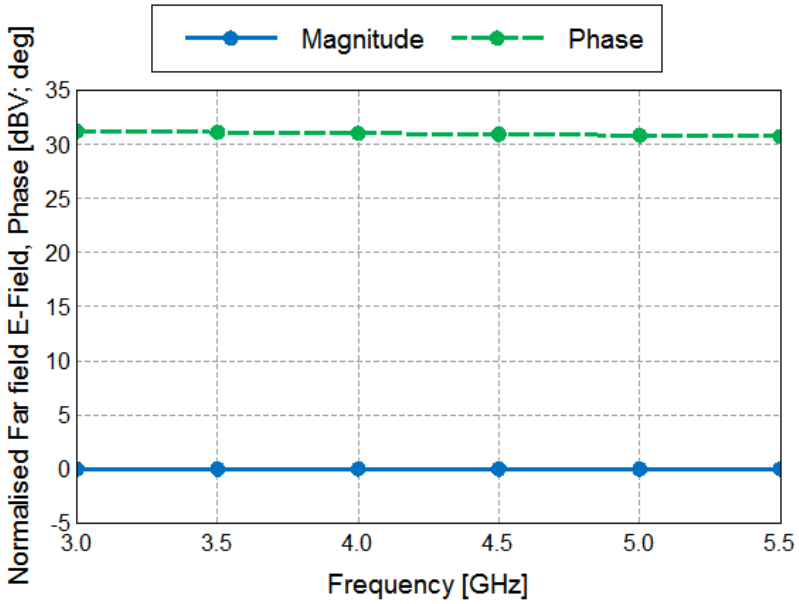

Fig. 6.20: Variations of the magnitude and phase versus frequency for the total field of the planar array of Fig. 6.18 at $\theta_s = 25^\circ$, $\phi_s = 0^\circ$ after compensating for active-element errors. The corresponding performance parameters (HP, D, and SLL) for this case are presented in Table B11.

Chapter 7: Implementation of Array Element Excitation

Real-time adaptive array excitation networks, or RF front ends, are good candidates for the adaptive array designs introduced in this work. As discussed in the literature review in Chapter 2, techniques based on the use of FPGA and Software Defined Radio (SDR) offer the most convenient solutions. SDR systems allow for real-time reconfiguration, a function that is difficult to achieve with fixed RF hardware. Integrating an adaptive interface with the array structure is necessary in order to provide frequency-invariant real-time beamforming and main-beam scanning. Additionally, an adaptive SDR system may extend the capabilities of the system to be integrated with different antenna arrays and different frequency-adaptive excitation algorithms. Practical constraints imposed by such factors as bandwidth, dynamic range, resolution, and speed of analog to digital converters (ADC), may limit the performance of real-time adaptive systems. In this chapter, the implementation of element excitation for array designs discussed in the previous chapters is addressed.

7.1 Adaptive element excitation using digital filters

Digital filters are a critical part of an adaptive digital signal processing (DSP) system. The frequency-domain excitation voltages of element antennas, namely $V_{np}^{A+}\left(\omega_p\right)$ in (4.44), are regarded as the transfer functions of the required digital filters in the feed network. The common requirements for these filters are stability and phase linearity. A stable filter can be characterized as a bounded-input bounded-output (BIBO) system. One way to ensure the stability of a digital filter is for the poles of its transfer function to reside on the left-half of the complex s-plane ($s = j\omega$). Other filter stability tests can be found in the literature [103].

The response of a digital filter can be modeled as a progressive linear sum of delayed weighted coefficients. A branch consisting of one delay term and one weight coefficient is designated as a filter tap. The response of the filter is the sum of the outputs of these taps. Two of the most common digital filters used in adaptive DSP systems are the finite impulse response (FIR) and the infinite impulse response (IIR) filters. The main difference between these two types of digital filters is that the IIR filter includes feedback, while the FIR filter involves only forwards processing of the input signal. The advantage of using feedback is to reduce memory

capacity requirements. However, a filter that includes feedback is not guaranteed to be stable, but a FIR filter is always stable [103, 104]. Another advantage of FIR filters is that it is easier to achieve linear phase characteristics with these filters.

7.2 FIR filter design

The block diagram of a FIR filter is shown in Fig. 7.1. The transfer function of the unit-time delay block in Fig. 7.1, represented by Z^{-1}, is given by $\exp(-j2\pi f)$, and the coefficients W_n are the weights of the filter. The transfer function of the filter is obtained as

$$H(f)=\frac{Y(f)}{X(f)}=\sum_{n=0}^{N-1}W_n Z^{-n};\quad Z=e^{j2\pi fT} \tag{7.1}$$

From (7.1) it can be seen that the impulse response of the FIR filter goes to zero within a finite period of time, hence the name finite impulse response (FIR).

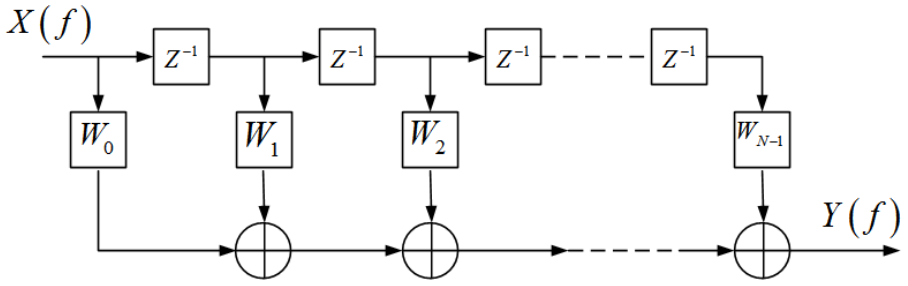

Fig. 7.1: Block diagram of a basic FIR filter, W_n are real valued weights, and Z^{-1} are time delay blocks

The required transfer function of the filter for each element antenna, necessary to achieve the performance of the array designs discussed in previous chapters, is already known. For the *n*th element, the transfer function of the associated filter is defined by $H(f)=V_n^{A+}(f)=V_{np}^{A+}(\omega_p)$ in (4.44) which can be divided into two purely real functions, one representing the real part, $H_{\mathrm{Re}}(f)=\mathrm{Re}\{V_n^{A+}(f)\}$, and another representing the imaginary part, $H_{\mathrm{Im}}(f)=\mathrm{Im}\{V_n^{A+}(f)\}$. Each part is realized by a separate filter with a real transfer function. A phase shift of 90° between $H_{\mathrm{Re}}(f)$ and $H_{\mathrm{Im}}(f)$ must be applied to form the complex transfer function. The 90° phase shifter must operate within the bandwidth of interest;

phase shifters like those used in [105] can be used for this purpose. It can be seen in (7.1) that the weights of the filter, W_n, can be calculated as Fourier series coefficients. Higher number of filter taps allow for generation of more accurate excitation signal for the element antenna.

A FIR filter with purely real transfer function can be realized by introducing conjugated filter taps to the FIR filter design of Fig. 7.1. The structure of the filter with the additional conjugated taps is shown in Fig. 7.2. The transfer function of the FIR filter with conjugate symmetrical taps is calculated as

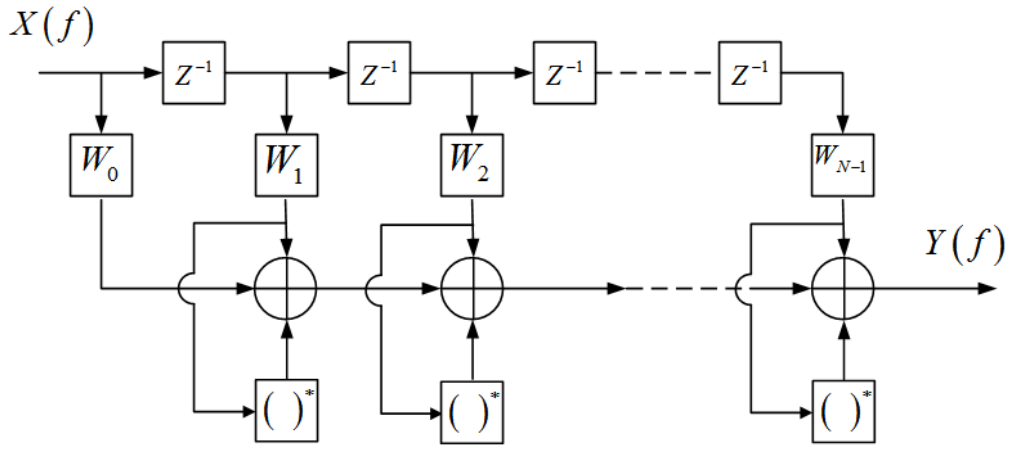

Fig. 7.2: Block diagram of FIR filter with conjugate symmetrical taps, W_n are real valued weights, Z^{-1} are time delay blocks, and $(\ )^*$ is a conjugation block

$$H(f)=\sum_{n=0}^{N-1}W_n\exp(-j2\pi nf)+\sum_{n=0}^{N-1}W_n\exp(+j2\pi nf)=2\sum_{n=0}^{N-1}W_n\cos(2\pi nf) \qquad (7.2)$$

As noted in (7.2), the transfer function of the FIR filter of Fig. 7.2 is a purely real function that also assumes the form of a truncated Fourier series. This property is necessary for realization of the real and the imaginary parts of the excitation of the element antenna as will be shown in the next section. The cost of FIR filters with conjugate taps might be higher than that of other types of FIR filter designs, but this cost comes with the benefit of providing the capability for realizing complex transfer functions with arbitrary real and imaginary parts, and hence arbitrary magnitude and phase functions.

7.3 Element antenna excitation

The signals fed to elements of an array each must possess specific magnitude and phase spectral characteristics in order to achieve the desired total radiated field over the bandwidth of interest. These spectral characteristics and their calculations were studied in details in Chapters 3 to 6. This section briefly addresses the realization of required spectral characteristics by means of digital filters. As mentioned earlier, two FIR filters with symmetrical conjugate taps for the realization of transfer functions $\mathrm{Re}\left\{V_n^{A+}(f)\right\}$ and $\mathrm{Im}\left\{V_n^{A+}(f)\right\}$ are needed. The block diagram of the overall filter structure, combining the real and imaginary parts, is shown in Fig. 7.3. The source signal, $X(f)$, is equally divided into two streams, one for $\mathrm{Re}\left\{V_n^{A+}(f)\right\}$ and the other for $\mathrm{Im}\left\{V_n^{A+}(f)\right\}$. The $\mathrm{Im}\left\{V_n^{A+}(f)\right\}$ part includes a 90° phase-shifter and the filter weights, denoted as W_n^{Im} and W_n^{Re}, are calculated by using (7.2). The output of the filter which constitutes the element excitation signal is

$$Y(f) = X(f)\cdot\left[\mathrm{Re}\left\{V_n^{A+}(f)\right\} + j\,\mathrm{Im}\left\{V_n^{A+}(f)\right\}\right] = X(f)\cdot V_n^{A+}(f) \qquad (7.3)$$

The additional phase shifting of the element signal, necessary to achieve main-beam scanning, can be implemented at the output of the filter structure of Fig. 7.3.

The main reason that digital filters seem to be viable candidates for the implementation of the array design techniques presented in this research is because of their flexibility. Digital filters are mostly programmable and highly reconfigurable thus allowing real-time reconfiguration of array element excitations. This capability facilitates the acquisition of the required magnitude and phase characteristics for element excitations in order to achieve a frequency-invariant antenna array performance.

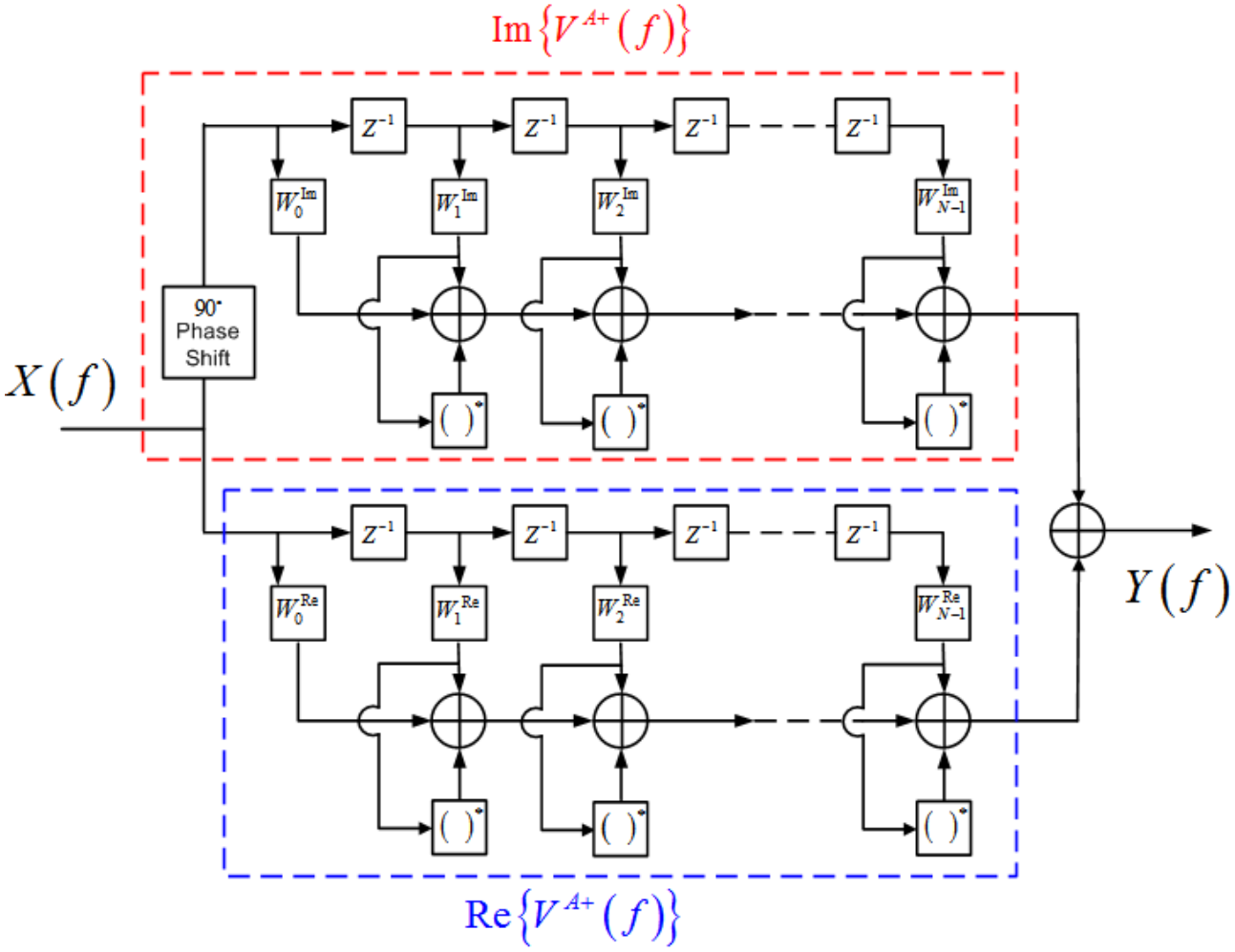

Fig. 7.3: Block diagram of the FIR filter for element antenna excitation, W_n are real valued weights, Z^{-1} are time delay blocks, and $(\ )^*$ is a conjugation block

Chapter 8: Conclusion and Future Work

A robust ultra-wideband array synthesis technique has been introduced and studied. The main objective of this research has been to achieve frequency-invariant radiation characteristics for array antennas that are capable of transmitting or receiving ultra-wideband signals with minimum distortions at boresight or within a specified spatial region. Frequency-adaptive antenna element excitation is employed in order to achieve such performance for the array. A summary of the main tasks of the proposed synthesis technique and the impact on the wideband performance of the array in each case is presented below. The main contributions of this research are pointed out and suggestions for further investigations are given

8.1 Summary

8.1.1 Element field compensation

The design technique presented in this research starts with calculating the complex radiated far-field of the isolated element antenna as a function of space and frequency. The array factor, expressed as a Fourier series, is constructed such that it would ideally converge (if the series had infinite number of terms) to a function obtained by multiplying the inverse of the element field and the desired total pattern of the array. Preliminary calculations of the array factor with isotropic elements provide useful estimations of maximum element spacing and how it is related to main-beam scan angle, appearance of grating-lobes, and achievable bandwidth. Mostly, the appearance of grating lobes sets the ultimate limits on the main-beam scanning range and bandwidth.

8.1.2 Inter-element mutual coupling compensation

Information about inter-element mutual coupling in a fully active array environment along with element field information are used in compensating the inter-element mutual coupling. Upon carrying out mutual coupling compensation, the adjusted excitation currents are delivered to the terminals of the element antenna in order to produce the required array factor. The input impedance of the element antenna is accounted for in the process of compensation for inter-element mutual coupling.

8.1.3 Achieving frequency-invariant total field pattern

At the beginning of the synthesis process, the field of the element antenna is calculated in isolation. The field of an isolated element might be a good approximation of its actual field in the array environment, as in the case of the wire dipole array design presented in Chapters 5 and 6, or might be significantly different from its actual field, as in the case of the arrays using elliptical dipole element also discussed in Chapters 5 and 6. The error resulting from using the field of an isolated element is related to the current distribution on the antenna. In a fully active array environment, the current distribution of the element antenna is affected by the induced currents due to radiation by the surrounding elements. In the previous subsection, compensation of inter-element mutual coupling is implemented at the excitation terminals of the element antenna, which does not mitigate current distribution alterations due to mutual coupling. One way to eliminate such error is to use active-element patterns at the beginning of the design process.

Calculating active-element patterns for each element could be impractical especially for large arrays such as the planar array designs presented in Chapter 6. Hybrid active-element methods, in which the center elements are assumed to have identical active-element patterns, could be helpful in reducing the computational burden. In fact, if Fourier series or any periodic series is used to synthesize the required array factor, the use of hybrid active-element method is necessary. Another way of eliminating the active-element error is to compensate for it. After producing a total-field based on the assumption of isolated element field, that contains the active-element error, the element excitations can be re-calculated iteratively to compensate for this error. The latter method of compensating for active-element error is adopted in this research. This compensation process could be performed over multiple iterations in order to achieve more accurate results. For the linear and planar arrays with elliptical element antenna, one iteration was enough to obtain satisfactory results.

8.2 Contributions

An ultra-wideband array synthesis technique has been introduced and validated by applying it to design linear and planar arrays of dipole elements. The main contributions of this research are summarized as follows:

- The proposed synthesis method is comprehensive and accounts for all factors contributing to bandwidth limitation of the array. The existing methods often do not address the frequency dependences of the element antenna or are limited to synthesizing the array factor only.
- Both magnitude and phase of the total radiated fields are considered in the synthesis process proposed here. Most existing array synthesis methods account for the power pattern only and leave the phase untreated.
- Using the proposed technique, linear and planar arrays can be synthesized that, in principle, can produce far-field total radiation patterns with arbitrary spatial variations which remain essentially unchanged over a wide frequency range. Also, the phase of the total radiated field of a synthesized array varies linearly with frequency over the bandwidth.
- The proposed technique allows synthesizing arrays that can provide bandwidths significantly larger than the bandwidths of their constituent elements. Linear and planar arrays of wire dipoles with a minimum bandwidth of 2.5 GHz, which were studied as example cases in Chapters 5 and 6, are a testimony to this fact.

8.3 Suggestions for future work

There are a number of issues that require further investigations in order to improve the performance of the array or optimize the design with the aim of reducing the cost. Suggestions for future work are summarized below.

- Noise and electromagnetic interference can be a significant source of wideband signal distortion. Compensation for noise and interference might be integrated into the synthesis method proposed in this research, provided that the modeling of such sources of signal distortions is available.
- As it was mentioned in this study, appearance of grating lobes is the main factor limiting the main-beam scanning range and bandwidth of the array. The use of unequal element spacing is an effective method to minimize the limiting effects of grating lobes.

Combining optimized unequal element spacing and optimized frequency-adaptive element excitation might be a topic of great potential for future research.

- Multi-rate sampling in the DSP stage of the array systems could help in reducing the number of required filters in order to achieve adaptive element excitation. As it was discussed in the literature survey of this dissertation, some researchers have applied this concept and developed frequency-invariant beamformers using only one reference filter while achieving the required filter responses for the different elements of the array through applying multi-rate sampling. Such technique could be used in the implementation of the adaptive element excitation proposed in this research in order to optimize the cost of the system of the wideband array.
- Having an optimized design for digital filters required for element excitations, fabricating the array geometries presented as example designs in this research will be an important task. Measuring the radiation characteristics of fabricated arrays and comparing them with simulation results are indeed necessary steps toward validating the predicted performances of the wideband and ultra-wideband arrays discussed in this work.

References

[1] Tuan, D. H. and Russer, P., "Signal processing for wideband smart antenna array applications," *IEEE Microwave Magazine,* vol. 5, pp. 57-67, 2004.

[2] Van Veen, B. D. and Buckley, K. M., "Beamforming: a versatile approach to spatial filtering," *IEEE ASSP Magazine,* vol. 5, pp. 4-24, 1988.

[3] Hong, S. K., "Resonance-Based Techniques for Microwave Breast Cancer Applications," Ph.D. Dissertation, Bradely Department of Electrical and Computer Engineering, Virginia Polytechnic Institute and State University, Blacksburg, 2012.

[4] Stutzman, W. L. and Thiele, G. Z., *Antenna Theory and Design*, Third Edition ed.: John Wiley and Sons, Inc., 2013.

[5] Balanis, C. A., *Antenna Theory*, Third Edition ed.: John Wiley and Sons, Inc., 2005.

[6] Mailloux, R. J., *Phased Array Antenna Handbook*, Second Edition ed. Norwood, MA 02062: Artech House, 2005.

[7] Safaai-Jazi, A., "A new formulation for the design of Chebyshev arrays," *IEEE Transactions on Antennas and Propagation,* vol. 42, pp. 439-443, Mar 1994 1994.

[8] Chan, S. C. and Pun, C. K. S., "On the design of digital broadband beamformer for uniform circular array with frequency invariant characteristics," in *IEEE International Symposium on Circuits and Systems, ISCAS*, 2002, pp. I-693-I-696 vol.1.

[9] Ghavami, M., "Wideband smart antenna theory using rectangular array structures," *IEEE Transactions on Signal Processing,* vol. 50, pp. 2143-2151, 2002.

[10] Uthansakul, M. and Bialkowski, M. E., "Fully spatial wide-band beamforming using a rectangular array of planar monopoles," *IEEE Transactions on Antennas and Propagation,,* vol. 54, pp. 527-533, 2006.

[11] Wei, L., "Adaptive Broadband Beamforming with Spatial-Only Information," in *15th International Conference on Digital Signal Processing*, 2007, pp. 575-578.

[12] Wei, L., McLernon, D. C., and Ghogho, M., "Design of Frequency Invariant Beamformer Without Temporal Filtering," *IEEE Transactions on Signal Processing,* vol. 57, pp. 798-802, 2009.

[13] Frost, O. L., III, "An algorithm for linearly constrained adaptive array processing," *IEEE Proceedings,* vol. 60, pp. 926-935, 1972.

[14] Schmidt, R. O., "Multiple emitter location and signal parameter estimation," *IEEE Transactions on Antennas and Propagation,,* vol. 34, pp. 276-280, 1986.

[15] Tuan, D. H., Demmel, F., and Russer, P., "A method for wideband direction-of-arrival estimation using frequency-domain frequency-invariant beamformers," in *IEEE Antennas and Propagation Society International Symposium*, 2003, pp. 244-247 vol.3.

[16] Yunhong, L., Ho, K. C., and Chiman, K., "3-D array pattern synthesis with frequency Invariant property for concentric ring array," *IEEE Transactions on Signal Processing,* vol. 54, pp. 780-784, 2006.

[17] Zhu, W., "Design of broadband adaptive array based on DFT interpolation method," in *International Conference on Transportation, Mechanical, and Electrical Engineering (TMEE)*, 2011, pp. 2315-2318.

[18] Subramanian, A., "UWB Linear Quadratic Frequency Domain Frequency Invariant Beamforming and Angle of Arrival Estimation," in *VTC2007-Spring. IEEE 65th Vehicular Technology Conference*, 2007, pp. 614-618.

[19] Alshammary, A., "Frequency invariant beamforming using sensor delay line," in *Saudi International Electronics, Communications and Photonics Conference (SIECPC)*, 2011, pp. 1-5.

[20] Abhayapala, T. D., Kennedy, R. A., and Williamson, R. C., "Broadband beamforming using elementary shape invariant beampatterns," in *Proceedings of the 1998 IEEE International Conference on Acoustics, Speech and Signal Processing*, 1998, pp. 2041-2044 vol.4.

[21] Repetto, S. and Trucco, A., "Frequency-Invariant Beamforming in Very Short Arrays for AUVs Instrumentation," in *Proceedings of the IEEE Instrumentation and Measurement Technology Conference, IMTC*, 2005, pp. 1113-1118.

[22] Crocco, M. and Trucco, A., "Design of Robust Superdirective Arrays With a Tunable Tradeoff Between Directivity and Frequency-Invariance," *IEEE Transactions on Signal Processing,* vol. 59, pp. 2169-2181, 2011.

[23] Traverso, F., Crocco, M., Trucco, A., and Vernazza, G., "Tuning the performance of the superdirective frequency-invariant beamforming applied to end-fire arrays," in *IEEE - Spain OCEANS*, 2011, pp. 1-7.

[24] Ronald, M., "Frequency-independent amplitude difference patterns in broadside arrays," in *IRE International Convention Record*, 1965, pp. 172-177.

[25] Holmgren, T., Ouacha, A., and Samuelsson, C., "Ultra Wideband Reconfigurable Beamforming and Beamshaping for Radar and Electronic Warfare Applications," in *European Radar Conference, EURAD*, 2005, pp. 157-160.

[26] Ouacha, A., Erickson, R., Gunnarsson, R., Carlegrim, B., Samuelsson, C., and Leijon, S., "Wideband Antenna Arrays with Reconfigurable Beamforming and Beamshaping," in *2007. IEEE/MTT-S International Microwave Symposium*, 2007, pp. 1867-1870.

[27] Wheeler, H., "Simple relations derived fom a phased-array antenna made of an infinite current sheet," *IEEE Transactions on Antennas and Propagation,,* vol. 13, pp. 506-514, 1965.

[28] Munk, B., *Finite antenna arrays and FSS*. Hoboken, N.J.: IEEE Press ; Wiley-Interscience, 2003.

[29] Yang, F. and Rahmat-Samii, Y., *Electromagnetic Band Gap Structures in Antenna Engineering*. New York: Cambridge University Press, 2009.

[30] Munk, B., Taylor, R., Durharn, T., Croswell, W., Pigon, B., Boozer, R., Brown, S., Jones, M., Pryor, J., Ortiz, S., Rawnick, J., Krebs, K., Vanstrum, M., Gothard, G., and Wiebelt, D., "A low-profile broadband phased array antenna," in *IEEE Antennas and Propagation Society International Symposium*, 2003, pp. 448-451 vol.2.

[31] Kasemodel, J. A., Chi-Chih, C., and Volakis, J. L., "Broadband planar wide-scan array employing tightly coupled elements and integrated balun," in *IEEE International Symposium on Phased Array Systems and Technology (ARRAY)*, 2010, pp. 467-472.

[32] Buxton, C. G., "Design of a Broadband Array Using the Foursquare Radiating Element," Ph.D. Dissertation, Bradely Department of Electrical and Computer Engineering, Virginia Polytechnic Institute and State University, Blacksburg, 2001.

[33] Nealy, J. R., "Foursquare antenna radiating element," U. S. Patent 5 926 137, 1999.

[34] Schaubert, D. H., Kasturi, S., Boryssenko, A. O., and Elsallal, W. M., "Vivaldi Antenna Arrays for Wide Bandwidth and Electronic Scanning," in *The Second European Conference on Antennas and Propagation, EuCAP*, 2007, pp. 1-6.

[35] Kasturi, S., "Wideband Characteristics of Vivaldi Antenna Arrays," Ph.D. Dissertation, Department of Electrical and Computer Engineering, University of Massachusetts Amherst, 2008.

[36] Smith, R. S., "Analysis and design of microstrip array antennas including mutual coupling," M.Sc. Thesis, Bradely Department of Electrical and Computer Engineering, Virginia Polytechnic Institute and State University, Blacksburg, 1986.

[37] Kelley, D. F., "Analysis of phased array antenna radiation patterns including mutual coupling," M.Sc. Thesis, Bradely Department of Electrical and Computer Engineering, Virginia Polytechnic Institute and State University, Blacksburg, 1990.

[38] Kelley, D. F. and Stutzman, W. L., "Array antenna pattern modeling methods that include mutual coupling effects," *IEEE Transactions on Antennas and Propagation,* vol. 41, pp. 1625-1632, 1993.

[39] Takamizawa, K., "Analysis of highly coupled wideband antenna arrays using scattering parameter network models," Ph.D. Dissertation, Bradley Dept of Electrical and Computer

Engineering, University Libraries, Virginia Polytechnic Institute and State University, Blacksburg, Va., 2004.

[40] Tang, W. and Zhou, Y., "Synthesis of power patterns for wideband arrays including mutual coupling," *Electronics Letters,* vol. 48, pp. 1581-1583, 2012.

[41] Tang, W. and Zhou, Y., "Frequency invariant power pattern synthesis for arbitrary arrays via simulated annealing," *Electronics Letters,* vol. 46, pp. 1647-1648, 2010.

[42] Jing, L. and Huawei, C., "Least squares frequency invariant beamforming robust against microphone mismatches," in *International Conference on Information Science and Technology (ICIST)*, 2011, pp. 496-499.

[43] Jing, L. and Huawei, C., "Robust frequency invariant beamformer design using variably-weighted constrained least squares," in *IEEE International Conference on Signal Processing, Communications and Computing (ICSPCC)*, 2011, pp. 1-6.

[44] Sorgel, W., Sturm, C., and Wiesbeck, W., "Impulse responses of linear UWB antenna arrays and the application to beam steering," in *IEEE International Conference on Ultra-Wideband, ICU*, 2005, pp. 275-280.

[45] Ertel, R. B., Zhong, H., and Reed, J. H., "Antenna array hardware amplitude and phase compensation using baseband antenna array outputs," in *IEEE 49th Vehicular Technology Conference*, 1999, pp. 1759-1763 vol.3.

[46] Deshuang, Z., Yuanwei, J., Bing-Zhong, W., and Rui, Z., "Time Reversal Based Broadband Synthesis Method for Arbitrarily Structured Beam-Steering Arrays," *IEEE Transactions on Antennas and Propagation,* vol. 60, pp. 164-173, 2012.

[47] Tanyer-Tigrek, F. M., Lager, I. E., and Ligthart, L. P., "On the Array Performance of Printed, Ultra-Wideband “Eared” Antennas," *IEEE Antennas and Propagation Magazine,* vol. 53, pp. 57-64, 2011.

[48] Gershman, A. B., "Robust adaptive beamforming: an overview of recent trends and advances in the field," in *4th International Conference on Antenna Theory and Techniques*, 2003, pp. 30-35 vol.1.

[49] Puskely, J. and Mikulasek, T., "Compact wideband Vivaldi antenna array for microwave imaging applications," in *7th European Conference on Antennas and Propagation (EuCAP)*, 2013, pp. 1519-1522.

[50] Pozar, D. M., "Waveform optimizations for ultrawideband radio systems," *IEEE Transactions on Antennas and Propagation,* vol. 51, pp. 2335-2345, 2003.

[51] Schantz, H., *The art and science of ultrawideband antennas*. Boston: Artech House, 2005.

[52] Marciano, J. S., Jr., Mehrpour, H., and Vu, T. B., "Adaptive control of a broadband array using frequency independent coefficients," in *Proceedings of the Fifth International Symposium on Signal Processing and Its Applications, ISSPA '99.*, 1999, pp. 897-900 vol.2.

[53] Obote, S., Ichikawa, Y., and Kagoshima, K., "A design methodology of a tapped delay line adaptive array antenna," in *IEEE Antennas and Propagation Society International Symposium*, 2005, pp. 30-33 vol. 4A.

[54] Junjie, G., Stark, H., and Yongyi, Y., "Design of tapped-delay line antenna array using vector space projections," *IEEE Transactions on Antennas and Propagation,* vol. 53, pp. 4178-4182, 2005.

[55] Sakai, F. and Ohta, K., "UWB array antenna utilizing novel electrical scanning system with tapped delay lines," in *IEEE MTT-S International Microwave Symposium Digest (MTT)*, 2010, pp. 1262-1265.

[56] Sakai, F., Suzuki, A., Kazuo, O., Makimoto, M., and Sawaya, K., "A UWB through-wall radar using beam scanning array antenna," in *IEEE MTT-S International Microwave Symposium Digest (MTT)*, 2011, pp. 1-4.

[57] Riza, N. A., "Photonic control of phased arrays using analog vector modulation," in *IEEE International Symposium on Phased Array Systems and Technology*, 1996, pp. 31-36.

[58] Joler, M., Malnar, D., and Barbin, S. E., "Real-time performance considerations of an FPGA-embedded genetic algorithm for self-recovery of an antenna array," in *ICECom, 2010 Conference Proceedings*, 2010, pp. 1-4.

[59] Chiba, I., Miura, R., Tanaka, T., and Karasawa, Y., "Digital beam forming (DBF) antenna system for mobile communications," *IEEE Aerospace and Electronic Systems Magazine,* vol. 12, pp. 31-41, 1997.

[60] Fischman, M. A., Le, C., and Rosen, P. A., "A digital beamforming processor for the joint DoD/NASA space based radar mission," in *Proceedings of the IEEE Radar Conference*, 2004, pp. 9-14.

[61] Xin-Huai, W., Xiao-Wei, S., Ping, L., Yan-Fu, B., Bo, L., Rui, L., and Hao-Jia, L., "Smart antenna design for GPS/GLONASS anti-jamming using adaptive beamforming," in *International Conference on Microwave and Millimeter Wave Technology (ICMMT)*, 2010, pp. 1149-1152.

[62] Harter, M. and Zwick, T., "An FPGA controlled digital beamforming radar sensor with three-dimensional imaging capability," in *International Radar Symposium (IRS), Proceedings*, 2011, pp. 441-446.

[63] Fournier, J. L., Titz, D., Ferrero, F., Luxey, C., Dekneuvel, E., and Jacquemod, G., "Phased array antenna controlled by neural network FPGA," in *Antennas and Propagation Conference (LAPC), Loughborough*, 2011, pp. 1-5.

[64] Weber, R. J. and Huang, Y., "A frequency agile beamforming array," in *IEEE International Symposium on Antennas and Propagation (APSURSI)*, 2011, pp. 2035-2038.

[65] Alwan, E. A., Khalil, W., and Volakis, J. L., "Ultra-Wideband On-Site Coding Receiver (OSCR) For Digital Beamforming Applications," presented at the IEEE APS-URSI, 2013.

[66] Horrell, J. M. and du Toit, L. J., "Array pattern synthesis using PBIL," in *IEEE 4th AFRICON*, 1996, pp. 276-281 vol.1.

[67] Ward, D. B., Kennedy, R. A., and Williamson, R. C., "Design of frequency-invariant broadband far-field sensor arrays," in *Antennas and Propagation Society International Symposium, AP-S. Digest*, 1994, pp. 1274-1277 vol.2.

[68] Ihsan, Z. and Solbach, K., "Frequency invariant far-field beam pattern of UWB printed circular monopole antenna array," in *The 7th German Microwave Conference (GeMiC)*, 2012, pp. 1-4.

[69] Ward, D. B., Kennedy, R. A., and Williamson, R. C., "FIR filter design for frequency invariant beamformers," *IEEE Signal Processing Letters,* vol. 3, pp. 69-71, 1996.

[70] Forcellini, S. and Kohno, R., "Frequency invariant beamformer using a single set of IIR filter coefficients and multirate techniques," in *IEEE Sixth International Symposium on Spread Spectrum Techniques and Applications*, 2000, pp. 575-579 vol.2.

[71] Hansen, R. C., *Microwave scanning antennas*. New York: Academic Press, 1964.

[72] Rufenach, C., Cronyn, W., and Neal, K., "Broad-band antenna array with application to radio astronomy," *IEEE Transactions on Antennas and Propagation,* vol. 21, pp. 697-700, 1973.

[73] Frankel, M. Y., Matthews, P. J., and Esman, R. D., "Wideband array transmitter with two-dimensional fiber-optic beam steering," in *IEEE International Symposium on Phased Array Systems and Technology*, 1996, pp. 425-428.

[74] Liao, P. and York, R. A., "A new phase-shifterless beam-scanning technique using arrays of coupled oscillators," *IEEE Transactions on Microwave Theory and Techniques,* vol. 41, pp. 1810-1815, 1993.

[75] Haupt, R. L., "Fitting time delay units in a large wideband corporate fed array," in *IEEE Radar Conference (RADAR)*, 2013, pp. 1-4.

[76] Haupt, R. L., *Antenna arrays : a computational approach*. Hoboken, N.J.: Wiley-IEEE Press, 2010.

[77] Corbin, J. and Howard, R. L., "TDU quantization error impact on wideband phased-array performance," in *IEEE International Conference on Phased Array Systems and Technology, Proceedings*, 2000, pp. 457-460.

[78] Bianchi, D., Genovesi, S., and Monorchio, A., "Reducing time-delay units through randomlyoverlapped subarrays in wideband linear array designs," presented at the IEEE APS-URSI, 2013.

[79] Lee, T.-S., "Efficient wideband source localization using beamforming invariance technique," *IEEE Transactions on Signal Processing,* vol. 42, pp. 1376-1387, 1994.

[80] Yan, S. and Hou, C., "Broadband DOA Estimation Using Optimal Array Pattern Synthesis Technique," *IEEE Antennas and Wireless Propagation Letters,* vol. 5, pp. 88-90, 2006.

[81] Liu, W., Wu, R., and Langley, R., "Beamspace Adaptive Beamforming for Broadband Planar Arrays," in *2007. IWAT '07. International Workshop on Antenna Technology: Small and Smart Antennas Metamaterials and Applications*, 2007, pp. 311-314.

[82] Ward, D. B., Zhi, D., and Kennedy, R. A., "Broadband DOA estimation using frequency invariant beamforming," *IEEE Transactions on Signal Processing,* vol. 46, pp. 1463-1469, 1998.

[83] Sekiguchi, T. and Karasawa, Y., "Wideband beamspace adaptive array utilizing FIR fan filters for multibeam forming," *IEEE Transactions on Signal Processing,* vol. 48, pp. 277-284, 2000.

[84] Ansari, R., "Efficient IIR and FIR fan filters," *IEEE Transactions on Circuits and Systems,* vol. 34, pp. 941-945, 1987.

[85] Liu, W., Wu, R., and Langley, R. J., "Design and Analysis of Broadband Beamspace Adaptive Arrays," *IEEE Transactions on Antennas and Propagation,* vol. 55, pp. 3413-3420, 2007.

[86] Gregory, M. D. and Werner, D. H., "Ultrawideband Aperiodic Antenna Arrays Based on Optimized Raised Power Series Representations," *IEEE Transactions on Antennas and Propagation,* vol. 58, pp. 756-764, 2010.

[87] Gregory, M. D., Namin, F. A., and Werner, D. H., "Exploiting Rotational Symmetry for the Design of Ultra-Wideband Planar Phased Array Layouts," *IEEE Transactions on Antennas and Propagation,* vol. 61, pp. 176-184, 2013.

[88] Gregory, M. D., Werner, D. H., and Werner, P. L., "Nature-inspired techniques for the synthesis of aperiodic ultra-wideband phased arrays," in *IEEE International Symposium on Phased Array Systems and Technology (ARRAY)*, 2010, pp. 707-712.

[89] Yoon-Won, K. and Pozar, D., "Optimization of pulse radiation from dipole arrays for maximum energy in a specified time interval," *IEEE Transactions on Antennas and Propagation,*, vol. 34, pp. 1383-1390, 1986.

[90] Ciattaglia, M. and Marrocco, G., "Time Domain Synthesis of Pulsed Arrays," *IEEE Transactions on Antennas and Propagation,* vol. 56, pp. 1928-1938, 2008.

[91] Johnson, D. H. and Dudgeon, D. E., *Array signal processing : concepts and techniques*. Englewood Cliffs, NJ: P T R Prentice Hall, 1993.

[92] Stutzman, W. L., *Polarization in electromagnetic systems* Artech House, 1993.

[93] Alsawaha, H. W. and Safaai-Jazi, A., "Ultrawideband Hemispherical Helical Antennas," *IEEE Transactions on Antennas and Propagation,* vol. 58, pp. 3175-3181, 2010.

[94] *FEKO User's Manual Suite 6.3*. Available: http://www.feko.info

[95] Alsawaha, H. and Safaai-Jazi, A., "Antenna Array Synthesis for Ultra-Wideband Signals," presented at the IEEE APS-URSI, 2013.

[96] Schantz, H. G., "Planar elliptical element ultra-wideband dipole antennas," in *IEEE Antennas and Propagation Society International Symposium*, 2002, p. 44.

[97] Duncan, C. and Lule, E., "Half disc element dipole antenna," in *IEEE Antennas and Propagation Society International Symposium*, 2005, pp. 576-579 vol. 2B.

[98] Alameddine, K., Chahine, S. A., Alim, O. A., and Osman, Z., "A New Modified Circular Disc Dipole Antenna for Ultra-Wideband Systems," in *IWCMC '08. International Wireless Communications and Mobile Computing Conference*, 2008, pp. 733-737.

[99] Ghavami, M. M. L. B. K. R., *Ultra-wideband signals and systems in communication engineering*. Chichester: John Wiley & Sons, 2004.

[100] Siwiak, K. M. D., *Ultra-wideband radio technology*. Chichester, England: Hoboken, NJ : Wiley, 2004.

[101] *Available on: http://www.ecfr.gov*.

[102] Bayram, A., "A Study of Indoor Ultra-wideband Propagation Measurement and Characterization," M.Sc. Thesis, Bradely Department of Electrical and Computer Engineering, Virginia Polytechnic Institute and State University, Blacksburg, 2004.

[103] Proakis, J. G. M. D. G., *Digital signal processing*. Upper Saddle River, N.J.: Pearson Prentice Hall, 2007.

[104] Najim, M., *Digital filters design for signal and image processing*. Newport Beach, CA: ISTE Ltd., 2006.

[105] Yong-Sheng, D., Da-Gang, F., and Yong-Xin, G., "A Novel Miniature 1–22 GHz 90 degrees MMIC Phase Shifter with Microstrip Radial Stubs," *IEEE Microwave and Wireless Components Letters,* vol. 18, pp. 109-111, 2008.

Appendix A: Formulation of the Transient Response of an Antenna

For an array antenna with its main-beam scanned to a direction defined by angles θ_s and ϕ_s, the general expression of the total field is given as:

$$\vec{E}(\theta_s,\phi_s,\omega) = -j\omega\mu\frac{e^{j(\omega t-\beta r)}}{4\pi r}\vec{P}_1(\theta_s,\phi_s,\omega) \tag{A.1}$$

$$\vec{P}_1(\theta_s,\phi_s,\omega) = \vec{P}(\theta_s,\phi_s,\omega) - \left[\vec{P}(\theta_s,\phi_s,\omega)\cdot\hat{r}\right]\hat{r} \tag{A.2}$$

$$\vec{P}(\theta_s,\phi_s,\omega) = \int_{v'}\vec{J}\left(\vec{r}',\omega\right)\, e^{j\beta r'\cdot\hat{r}}dv' \tag{A.3}$$

where

$\vec{J}\left(\vec{r}',\omega\right)$ is the current distribution of the radiator or the antenna

$\vec{r}'$ is the position vector that describes the geometry of the radiator

$\vec{r}$ is the position vector of that describes the location of the point of observation

Let $S(\omega)$ be considered as the frequency-domain representation of a wideband input signal to an LTI system such as an antenna, then if we can define the function

$$\vec{X}(\theta_s,\phi_s,\omega) = \vec{P}_1(\theta_s,\phi_s,\omega)S(\omega), \tag{A.4}$$

the inverse Fourier transform of the field given in (A.1) is:

$$\vec{e}(\theta_s,\phi_s,t) = -\frac{\mu}{4\pi r}\frac{\partial}{\partial t}\vec{x}(\theta_s,\phi_s,t-r/c) \tag{A.5}$$

where $\vec{x}(\theta_s,\phi_s,t) = \vec{p_1}(\theta_s,\phi_s,t) * s(t)$.

NOTE: the formulation above can be used to calculate the transient response of an array in any direction, not just the direction of the main-beam.

Appendix B: Performance Parameters (HP, D, and SLL) for Array Design Examples Presented in Chapters 5 and 6

Table B1: Summary of performance parameters for the wire dipole array described in Fig. 5.6 (The geometry and parameters of the array are the same as those given in Fig. 5.1.)

Frequency (GHz)	Performance Parameters		
	HP	*D*	SLL
4.5	15.1º	11.6 dB	-45.4 dB
5.0	14.9º	11.7 dB	-49.1 dB
5.5	14.8º	11.8 dB	-58.1 dB
6.0	14.7º	11.9 dB	< -58.1 dB
6.5	14.7º	12.0 dB	< -58.1 dB
7.0	14.7º	12.1 dB	< -58.1 dB

Table B2: Summary of performance parameters for the elliptically-tapered disc-dipole array described in Fig. 5.18 (The geometry and parameters of the array are the same as those given in Fig. 5.13.)

Frequency (GHz)	Performance Parameters		
	HP	*D*	SLL
3.0	19.4º	10.7 dB	-18.2 dB
4.0	15.8º	11.9 dB	-25.8 dB
5.0	14.0º	12.7 dB	-30.3 dB
6.0	13.0º	13.2 dB	-37.7 dB
7.0	12.9º	13.5 dB	-41.5 dB
8.0	13.3º	13.5 dB	-51.6 dB
9.0	13.4º	13.2 dB	< -58 dB
10.0	13.4º	12.3 dB	< -58 dB
11.0	13.3º	10.5 dB	< -58 dB

Table B3: Summary of performance parameters for the elliptically-tapered disc-dipole array described in Fig. 5.20 (The geometry and parameters of the array are the same as those given in Fig. 5.13.)

Frequency (GHz)	**Performance Parameters**		
	HP	*D*	SLL
3.0	18.7º	10.8 dB	-16.6 dB
4.0	15.8º	12.0 dB	-25.0 dB
5.0	14.1º	12.7 dB	-33.1 dB
6.0	13.8º	13.0 dB	-53.1 dB
7.0	13.7º	13.3 dB	-51.9 dB
8.0	13.5º	13.5 dB	< -58 dB
9.0	13.5º	13.2 dB	< -58 dB
10.0	13.5º	12.26 dB	< -58 dB
11.0	13.5º	10.5 dB	< -58 dB

Table B4: Summary of performance parameters for the planar array of wire dipoles described in Fig. 6.2 (The geometry and parameters of the array are the same as those given in Fig. 6.1.)

Frequency (GHz)	**Performance Parameters**		
	HP_x / HP_y	*D*	SLL
4.5	13.9º/13.5º	20.0 dB	< -40 dB
5.0	13.7º/13.5º	20.0 dB	< -40 dB
5.5	13.5º/13.5º	20.0 dB	< -40 dB
6.0	13.5º/13.5º	20.0 dB	< -40 dB
6.5	13.5º/13.5º	20.0 dB	< -40 dB
7.0	13.5º/13.5º	20.0 dB	< -40 dB

Table B5: Summary of performance parameters for the planar array of wire dipoles described in Fig. 6.4

(The geometry and parameters of the array are the same as those given in Fig. 6.1.)

Frequency (GHz)	**Performance parameters**		
	HP_x	D	SLL
4.5	20.0º	18.2 dB	< -40 dB
5.0	19.6º	18.3 dB	< -40 dB
5.5	19.3º	18.3 dB	< -40 dB
6.0	19.1º	18.3 dB	< -40 dB
6.5	19.2º	18.3 dB	-26 dB
7.0	21.1º	18.0 dB	-14.5 dB

Table B6: Summary of performance parameters for the planar array of wire dipoles described in Fig. 6.6

(The geometry and parameters of the array are the same as those given in Fig. 6.1.)

Frequency (GHz)	**Performance Parameters**		
	$HP_{\phi=25^\circ}$	D	SLL
4.5	19.8º	18.2 dB	< -40 dB
5.0	19.4º	18.3 dB	< -40 dB
5.5	19.2º	18.3 dB	< -40 dB
6.0	19.1º	18.4 dB	< -40 dB
6.5	19.2º	18.3 dB	-23.8 dB
7.0	19.4º	18.2 dB	-14.3 dB

Table B7: Summary of performance parameters for the planar array of wire dipoles above ground plane described in Fig. 6.10 (The geometry and parameters of the array are the same as those given in Fig. 6.9.)

Frequency (GHz)	Performance Parameters		
	$HP_{\phi=25^\circ}$	D	SLL
4.5	18.4º	21.7 dB	< -40 dB
5.0	18.2º	21.8 dB	< -40 dB
5.5	18.3º	21.7 dB	< -40 dB
6.0	18.5º	21.7 dB	< -40 dB
6.5	18.7º	21.6 dB	< -40 dB
7.0	19.0º	21.4 dB	-28.4 dB

Table B8: Summary of performance parameters for the planar array of elliptical dipoles described in Figs. 6.13 and 6.14 (The geometry and parameters of the array are the same as those given in Fig. 6.11.)

Frequency (GHz)	Performance Parameters		
	HP_x	D	SLL
3.0	24.7º	17.2 dB	-18.4 dB
3.5	21.3º	17.8 dB	-17.6 dB
4.0	18.9º	18.3 dB	-15.8 dB
4.5	18.6º	18.2 dB	-14.0 dB
5.0	18.6º	18.2 dB	-15.1 dB
5.5	16.2º	18.6 dB	-17.9 dB

Table B9: Summary of performance parameters for the planar array of elliptical dipoles described in Fig. 6.15 (The geometry and parameters of the array are the same as those given in Fig. 6.11.)

Frequency (GHz)	Performance Parameters		
	HP_x	D	SLL
3.0	24.7º	17.2 dB	-18.4 dB
3.5	21.3º	17.8 dB	-17.6 dB
4.0	18.9º	18.3 dB	-15.8 dB
4.5	18.6º	18.2 dB	-14.0 dB
5.0	18.6º	18.2 dB	-15.1 dB
5.5	16.2º	18.6 dB	-17.9 dB

Table B10: Summary of performance parameters for the planar array of elliptical dipoles above ground plane described in Figs. 6.18 and 6.19 (The geometry and parameters of the array are the same as those given in Figs. 6.11 and 6.16.)

Frequency (GHz)	Performance Parameters		
	HP_x	D	SLL
3.0	24.1º	20.3 dB	-18.3 dB
3.5	21.4º	20.8 dB	-18.7 dB
4.0	19.1º	21.2 dB	-23.1 dB
4.5	16.8º	21.6 dB	-16.1 dB
5.0	18.4º	21.2 dB	-16.3 dB
5.5	16.2º	21.3 dB	-18.2 dB

Table B11: Summary of performance parameters for the planar array of elliptical dipoles above ground plane described in Fig. 6.20 (The geometry and parameters of the array are the same as those given in Figs. 6.11 and 6.16.)

Frequency (GHz)	**Performance Parameters**		
	HP_x	D	SLL
3.0	24.1º	21.6 dB	-18.3 dB
3.5	21.4º	22.3 dB	-18.7 dB
4.0	19.1º	22.8 dB	-23.1 dB
4.5	16.8º	23.3 dB	-16.1 dB
5.0	18.3º	23.0 dB	-16.3 dB
5.5	16.1º	23.3 dB	-18.2 dB

Appendix C: Surface Current Density Distributions on elements of Linear Array of Elliptical Dipole Antennas

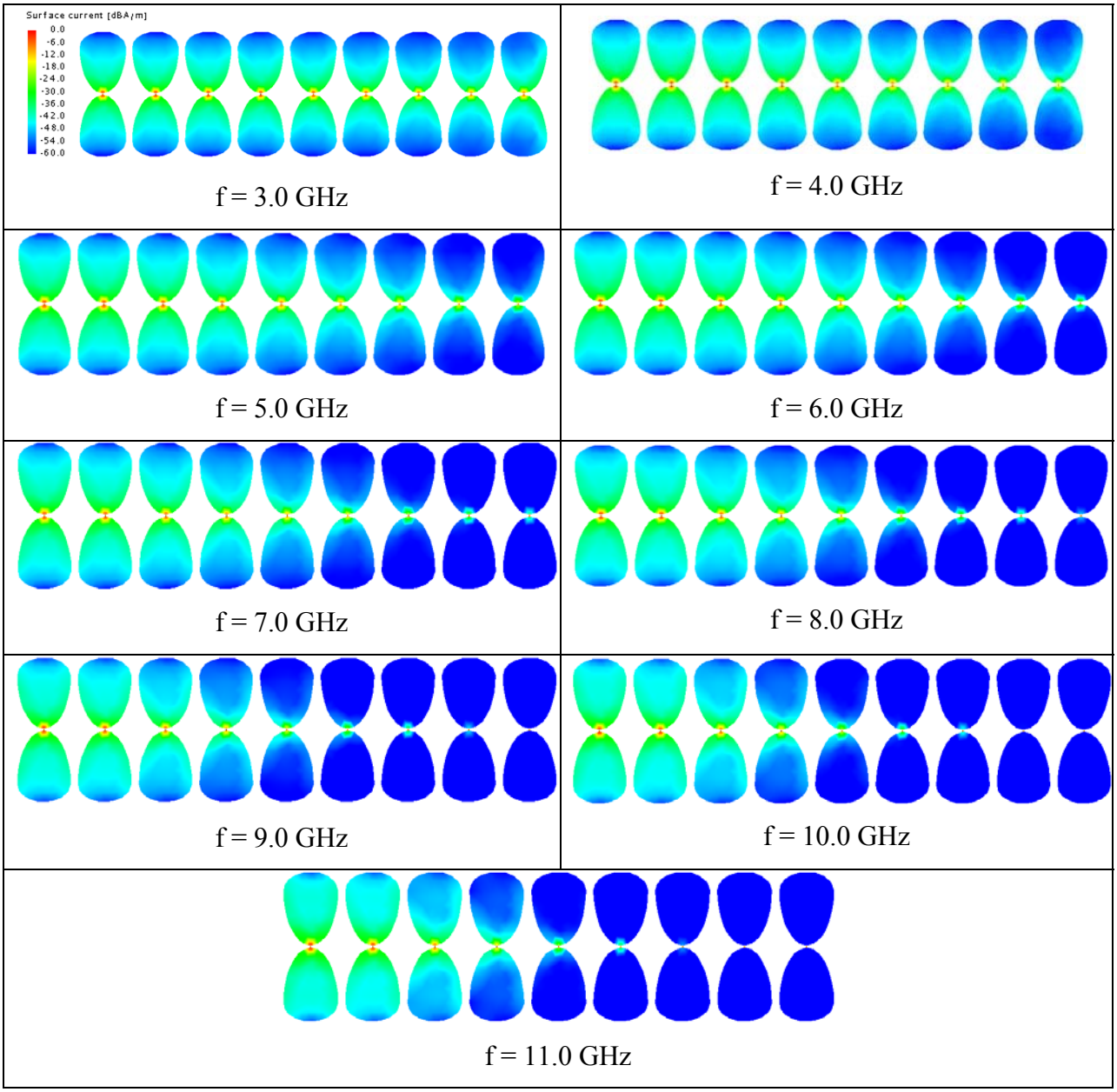

Fig. C1: Illustration of surface current distributions for half of the elements of the array described in Fig. 5.14 with center element shown on the left (The geometry and parameters of the array are the same as those given in Fig. 5.13.)

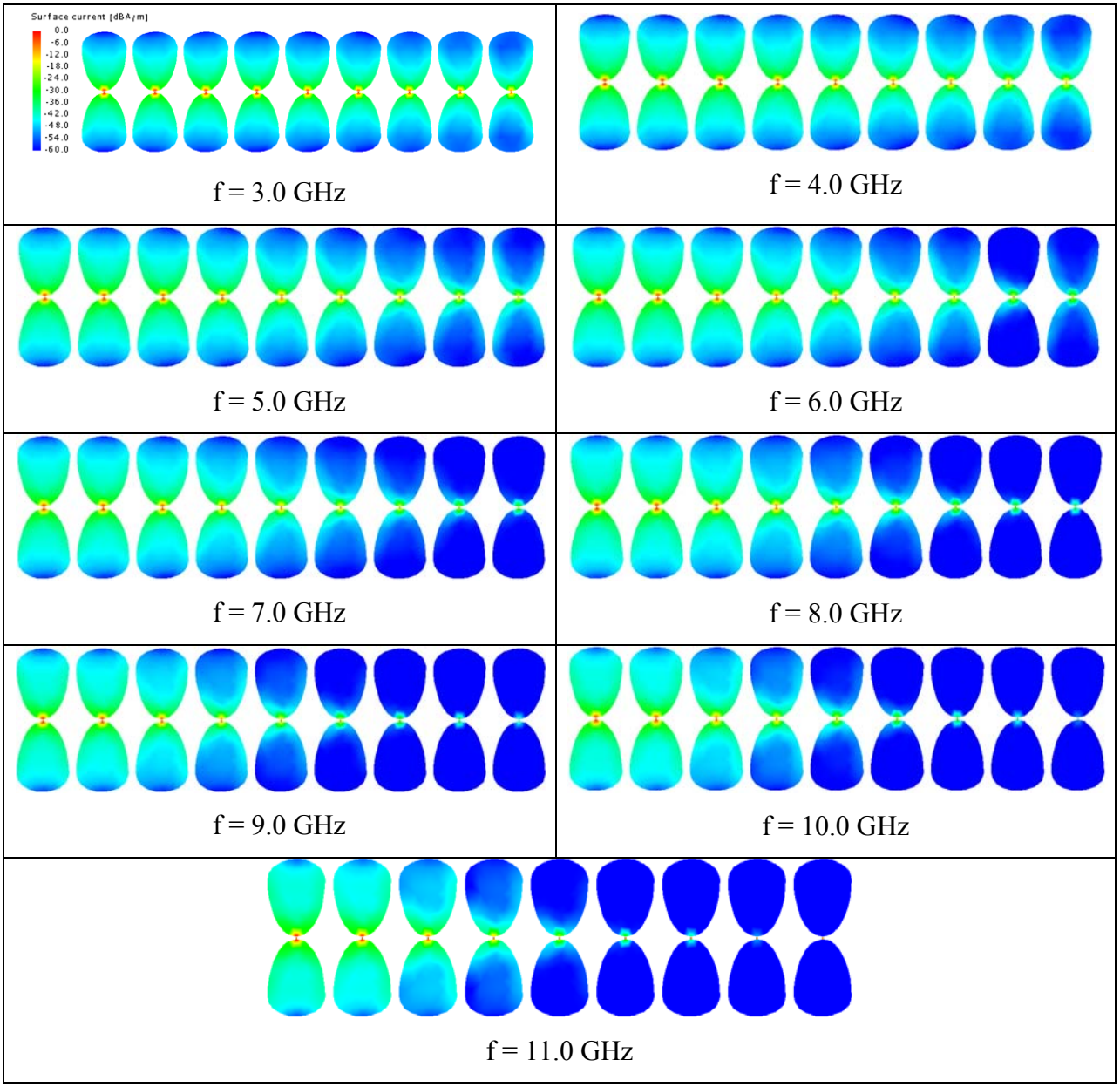

Fig. C2: Illustration of surface current distributions for half of the elements of the array described in Fig. 5.18 with center element shown on the left (The geometry and parameters of the array are the same as those given in Fig. 5.13.)

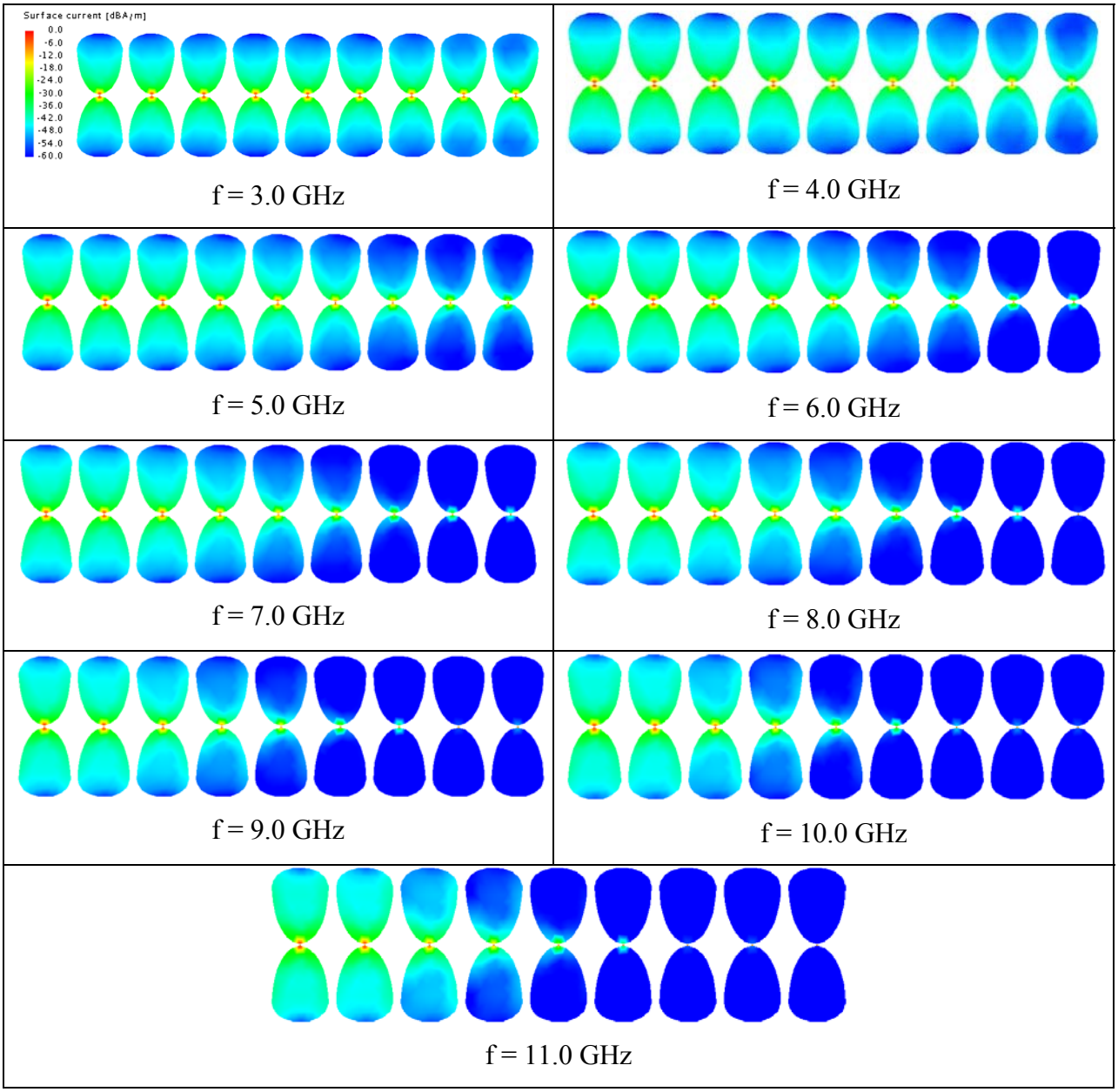

Fig. C3: Illustration of surface current distributions for half of the elements of the array described in Fig. 5.20 with center element shown on the left (The geometry and parameters of the array are the same as those given in Fig. 5.13.)